Report no: CSM/MT/CWJCR/2005/009

FINAL PROJECT REPORT

AN ASSESSMENT OF MAGNETIZATION EFFECTS ON HYDROGEN CRACKING FOR THICK WALLED PIPELINES

MMS Contract Number: 0103PO73498
CSM Project No. 4-42368

Submitted to

MINERAL MANAGEMENT SERVICES –US Department of Interior
OFFICE OF PIPELINE SAFETY- US Department of Transportation

Attn: Mr. Michael Else
Engineering & Research Branch
381 Elden Street, MS 4021
Herndon, VA 20170-4817

[Performance Period: August 1, 2003-December31, 2005]

Submitted by

Brajendra Mishra
David L. Olson
Francisco Sanchez

CENTER FOR WELDING JOINING & COATINGS RESEARCH
DEPARTMENT OF METALLURGICAL & MATERIALS ENGINEERING

DECEMBER 2005

TABLE OF CONTENTS

EXECUTIVE SUMMARY

Because pipelines are designed conservatively to protect against unforeseen events, pipeline networks require a high level of confidence. This means a high reliance on inspection techniques such as the Magnetic Flux Leakage (MFL) pigging tool. This technique is based on the principle of magnetizing the pipe wall and then detecting a local flux leakage caused by anomalies relative to change in pipe wall thickness.

Laboratory experiments demonstrate that the diffusible hydrogen content in steels can be significantly affected by a magnetic induction. The magnetization produced during MFL pigging operations could have an effect on the hydrogen concentration in pipeline steels. This means the susceptibility of steels to the hydrogen-cracking phenomenon and potential catastrophic failure is higher.

The experimental studies in this dissertation were on the magnetization effect on hydrogen concentration in pipeline steels, the magnetization effect on hydrogen concentration in cold-worked steel samples, and the magnetization effect on hydrogen induced cracking for thick high strength pipeline steels.

To evaluate how a strong magnetic flux density produced throughout recurrent pigging routines affect the hydrogen-induced cracking susceptibility of thick walled and high-strength pipeline steels, five independent variables and one dependent variable have been defined. The independent variables are pipeline steel grade, wall thickness, residual stress effect, magnetic flux density, and hydrogen charging time. The dependent variable is the absorbed hydrogen concentration. The experimental approach used three steel grades: X52, X70, and X80. The actual yield strength levels of these grades were in the range of 70-90 ksi. The wall thickness ranges from $^{9}/_{32}$ to $^{5}/_{8}$ inches (6.89 to 15.3 mm). Test specimens are sectioned from cold worked samples bent at different angles to induce varying levels of residual stresses. The selected magnetic flux density level is the saturation induction and the hydrogen charging time was set at different periods of time from one to six hours.

The experimental approach shows that the saturation magnetic induction generated by MFL inspection tools considerably increases the hydrogen content in pipeline steels. Adsorbed hydrogen concentration (total hydrogen content) in the tested cold-worked pipeline steel samples increases with increasing the residual stress concentration. The hydrogen induced cracking susceptibility of steel is negatively affected by the magnetic induction of 2 Tesla (20,000 Gauss). The magnetic induction accelerates the hydrogen damage phenomenon; i.e., the tested steels are more susceptible to hydrogen cracking under a strong magnetic field.

Even though the results revealed the effect of saturation magnetic induction on the absorbed hydrogen concentration in pipeline steels, the effect of the remanent magnetization left behind by inspection tools was mathematically analyzed but not experimentally determined. The remanent magnetic induction may increase up to sixty percent the absorbed hydrogen content in the studied pipeline steels.

NOMENCLATURE

B	Magnetic induction or total magnetic flux density
C_H	Concentration of hydrogen – [H]
D	Lattice diffusivity
Do	Pre-exponential term
E	Electrochemical potential
E^o	Standard half-cell electrode potential for reactions
E_p	Potential Energy
F	Faraday's constant
H	Magnetic field
H_m	Intensity of the molecular field
k	Hydrogen solubility constant
L	Separation distance of magnetic poles of strength
L	Length of membrane in the Devanathan cell.
m	Magnetic moment of the magnet
M	intensity of magnetization
M_s	Saturation magnetization
p	Pole Strength
Q	Activation energy
R	Universal gas constant
T	Temperature
T_{lag}	Time lag for Devanathan cell
τ	Moment of the couple or torque
V	Volume of solid
μ_o	Magnetic permeability of vacuum
μ	Magnetic permeability
χ	Magnetic susceptibility
γ	Molecular field coefficient
θ	Angle apart from the field direction

1. INTRODUCTION

The most efficient method for transporting fluids in the oil, gas, and petrochemical industries is through steel pipelines. Pipelines are designed conventionally to protect against high-pressure, thermal effects, ice mechanics, and environmental degradation. To satisfy these conditions, pipelines are constructed from thick wall pipes and high-strength steels. However, high-strength steels are susceptible to hydrogen induced cracking. This susceptibility is affected primarily by the hydrogen concentration, steel microstructure, stress concentration, temperature, and environment.

During oil and gas operations hydrogen may be introduced in steel from various sources, such as hydrogen-bearing environments during welding, heat-treatment, pickling or service. The most common service source of hydrogen is the cathodic reduction of water, which can be present during cathodic protection for corrosion.

The integrity of pipelines, with high level of confidence and reliance, is monitored using intelligent inspection tools (broadly known as intelligent pigs). One of the assessment methods is the in-line inspection technology of determination of localized Magnetic Flux Leakage (MFL). This technique performs by magnetizing the pipe steel near the saturation flux density and then detecting a local flux leakage caused by anomalies in surface morphologies. The magnetic saturation flux density of high-strength pipeline steels is approximately 1.9 Tesla (19,000 Gauss), while the remaining density (remanence) is in the region of one Tesla (10,000 Gauss). Since the maximum energy product of MFL pigging tools can easily reach 30 megagauss-oersted (MGOe) and even go as high as 50 MGOe, depending on the level and duration of remanent magnetization left by MFL inspection tools, the steel may be more susceptible to hydrogen induced cracking.

The aim of the present study is to demonstrate experimentally that the magnetic induction generated by MFL inspection tools affects considerably the hydrogen content in pipeline steels (as-received and cold-worked) and its influence on the hydrogen induced cracking susceptibility in pipeline steels. It is shown that the hydrogen concentration in steels is a function of the surrounding magnetic field strength besides hydrogen-bearing environment pressure, steel composition and microstructure. The experimental investigation was carried out on three pipeline steel grades under a strong and uniform magnetic field of approximately 2 Tesla (20,000 Gauss).

The main objective of this research is to comprehend experimentally and describe the effect of high strength magnetic fields applied during frequent pigging to steel pipeline on the hydrogen-induced cracking susceptibility. This research project will quantitatively measure the increased hydrogen activity in the thick walled, high strength steels due to the magnetization and establish if the augmented level of diffusible hydrogen is deleterious to the integrity of the pipes. If the remaining magnetism left in steel pipes after pigging causes significant enhancement in hydrogen absorption at either the internal or the external surface of the pipe will also be determined, as well as, if this phenomenon promotes the initiation of hydrogen assisted cracking. If the hydrogen effect is determined to be deleterious, a group of additional tasks will be proposed to have a better understanding of this phenomenon and its operational implications. The approach of future researches will generate enough scientific data to develop prevention methods to minimize pipeline steel damage after magnetic flux leakage pigging.

2. LITERATURE REVIEW

The purpose of this chapter is to provide a literature review of three of the most relevant technical areas of this research. These areas of interest are: (1) pigging analysis of pipelines, (2) magnetism and magnetic phenomena in steel, and (3) magnetic flux leakage technique in pipeline pigging inspection. These three subjects bring up others issues to address the assessment of the effect of in-line inspection magnetic tools on hydrogen induced cracking phenomenon in high strength, thick walled pipeline steels. The other subjects are the hydrogen damage mechanism and the relationship between the hydrogen concentration and the magnetic flux density. These two subjects are discussed in Chapters Three and Four.

Even though there has been no previous work on the effect of magnetization on hydrogen damage in pipeline steels after pigging operations, some physics, metallurgy, and corrosion-oriented papers on magnetism phenomenon and hydrogen damage in pipelines have been reviewed. This review also includes literature related to pigging operations and techniques and failure analysis of line pipes.

2.1 Pigging Analysis of Pipeline

In this section an introductory description of the concept and history of pigging is presented. Additionally, the goals and application of pigging operations, in line inspection techniques, and the characteristics of magnetic flux leakage tools are discussed.

2.1.1 Pigging: Concept and History

The most efficient method for transporting fluids in the oil, gas and petrochemical industries is the pipeline. Even though the construction material of the first pipeline is not recorded, the first pigging operation took place during 1870's to remove the paraffin deposits that were produced inside a crude oil pipeline. These paraffin deposits reduced the internal diameter of the pipe affecting the oil transportation process efficiency (PPSA 1995).

The pigging tool, commonly known as pig, is defined as a device that moves through the inside of a pipeline as a free moving piston, sealing against the inside wall with sealing elements for the purpose of cleaning, dimensioning, or inspection (see Figure 2.1). This definition covers in excess of 500 different designs and types of pigs. Pigs get their name from the squealing, scraping, noise made by a pipe cleaner (pigging tool) traveling through the steel line (pipeline). It sounded like the "squeal of a pig" in accordance with a pipeline operator comment at the beginning of the 20^{th} century.

Pipeline failures have heightened the awareness of transmission pipeline systems. The integrity of the pipelines is monitored using "smart" or "intelligent" pigging (instrumented pigs). This method of monitoring is becoming industrially common and is required by international regulations. These regulations require that internal inspections be performed using equipment which provides the detection of corrosion, cracks, laminations, and changes in pipe wall thickness, etc (Nespeca and Hvending 1988).

According to a recent study (Leis 1999), mechanical damage is the single largest cause of failures on gas transmission pipelines and a leading cause of failures on hazardous liquid pipelines. The mechanical damage usually occurs after a pipeline is constructed and is caused by excavation equipment, which deforms the shape of the pipe, scrapes away metal and coating, and/or changes the mechanical properties of the pipe.

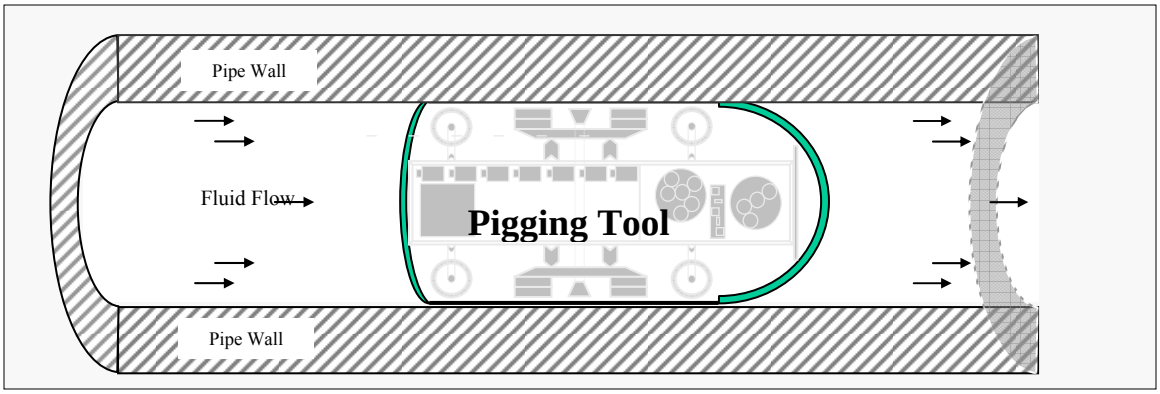

Figure 2.1. Common pigging tool (pig) used to clean, size or inspect pipelines (after PPSA 1995).

Internal inspection devices are integral parts of every pipeline-monitoring program. The inspection operation by pigging is a rapidly maturing technology and is based on instrumented pigs. Advancements in electronics and computing technology have made this technique more useful and beneficial (Muhlbauer 1992). In 1987, it was necessary to confirm the technical capability and commercial availability of a new "State of the Art" inspection tool for use in the Ekofisk-Emden 36-in. gas pipeline: the magnetic flux leakage inspection. Nespeca and Hvending (1988) described some special pigging requirements for large diameter pipelines as the following: (a) vary internal diameter, (b) pipeline misalignment, and (c) severe bending radius.

2.1.2 Objectives of Pigging

Two fundamental requirements must be addressed in designing a pipeline where pigs have to function in a manner to maintain continuous operations and investment efficiency. The contribution that pigging inspection does to guarantee nonstop functionability and maximum efficiency of the pipeline is achieved by (PPSA 1995; Choumar 1996):

a) Eliminating internal deposits,
b) Monitoring the physical and operational conditions and verifying them against current service requirements,
c) Evaluating external coating conditions,
d) Supplying data concerning any apparent problems as well as potential repairs,
e) Gauging internal bore,
f) Reducing possibilities to design statutory recurrent tests.

The full-length pipeline pigging operation without interruption is the main advantage of smart or intelligent pigs when inspection is the principal concern. Intelligent, instrumented pigs

have become of paramount importance in the management of pipeline integrity (Choumar, 1996). "Pipeline Integrity Management," widely used by oil and gas industry nowadays, defines procedures to reduce the billions of dollars spent on corrosion control of pipeline systems. An effective management program that engages in the integrity threats typically associated with pipeline systems can reduce the probability of failure. These threats include, but are not limited to, external corrosion, internal corrosion, mechanical damage, and environmental assisted cracking (Vieth *et al.* 2002).

2.1.3 Application of Pigging Operations

Although pipeline pigging operation was only used in the past for removing liquid or solid deposits, nowadays it is involved in all pipeline life stages. Those basic phases are the construction, operation, inspection, maintenance, rehabilitation, and decommissioning of the pipeline. Pipeline inspection or in-line inspection (ILI) operations cover a widely range of inspection services; however, the two most common requirements are for geometry measurement and metal-loss detection (PPSA 1995). The pigging tools employed in pipeline inspection based on metal loss detection and sizing accuracy are essentially divided into two groups: ultrasonic and magnetic flux leakage tools.

2.1.4 In-Line Inspection Techniques

Pipeline operators use at present a wide variety of methods to evaluate, inspect, and monitor the transmission pipelines in operation worldwide. These methods include cathodic protection surveys, leak detection programs, excavations to look for pipe corrosion or protective coating failures, hydrostatic tests, and the use of in-line inspection tools that travel through the pipe (Nestleroth and Bubenik 1999). For the purpose of this work, in-line inspection will be considered as the most relevant method of pipeline assessment.

The use of pigs for in-line inspection of pipelines has increased considerably. The beginning of in-line inspection with the introduction of a corrosion-measuring tool based on magnetic flux leakage technology was in the early 1960's. In 1980, a high-resolution magnetic flux leakage tool was developed starting a new era of in-line inspection tools.

Some of the in-line inspection techniques available use intelligent pigs. They are based on (a) geometry or caliper/deformation technique to characterize bend radii, dents and changes in ovality; and (b) ultrasonic and magnetic flux leakage techniques to characterize corrosion-caused metal loss and sizing.

2.1.5 Magnetic Flux Leakage (MFL) Tools

The magnetic flux leakage (MFL) technique is based on the principle of magnetizing the pipe wall using very strong magnets and then detecting a local flux leakage caused by metal loss (or gain) or other anomaly relative to change in pipe wall thickness. This technique can only be applied on ferromagnetic materials, such as low-alloy-carbon steels, which have a high magnetic permeability. The MFL tools are the most commonly used in-line inspection pigs. They can be run in oil, gas or multiphase flow systems.

Magnetic flux leakage tools can be either segmented, with two or more parts joined by flexible connectors, or as a single piece where all the components are contained with in a single, rigid package. Generally, segmented and single-piece MFL pigs incorporate several arrangements: drive or pushing system, magnetic system, sensor system (many rows of sensors covering the complete circumference of the pipe wall), data conditioning and recording system, and power system (see Figure 2.2). MFL tools generally require specially designed launching, running, retrieving procedures to operate pigs in the pipeline (PPSA 1995).

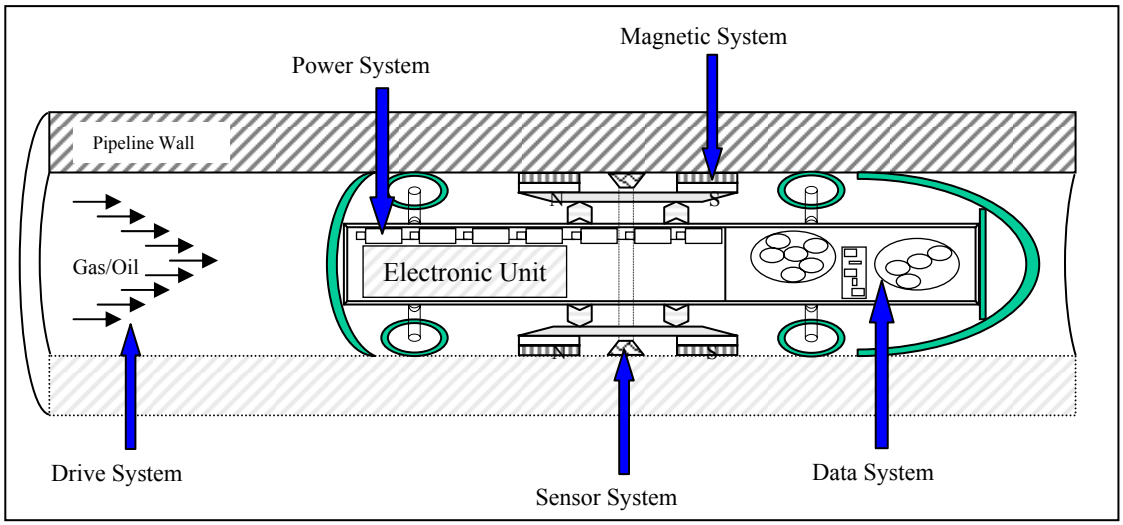

Figure 2.2. General systems incorporated in segmented or single-piece MFL pigs (after PPSA 1995).

The magnetic system is a set of strong magnets (either permanent magnets or battery-powered electromagnets) that are circumferentially arranged around the internal surface of the pipe. They magnetize a length of the pipeline wall. The magnets transmit the magnetic field to the pipe and its ends are connected to metal brushes placed against the pipe wall (see Figure 2.3).

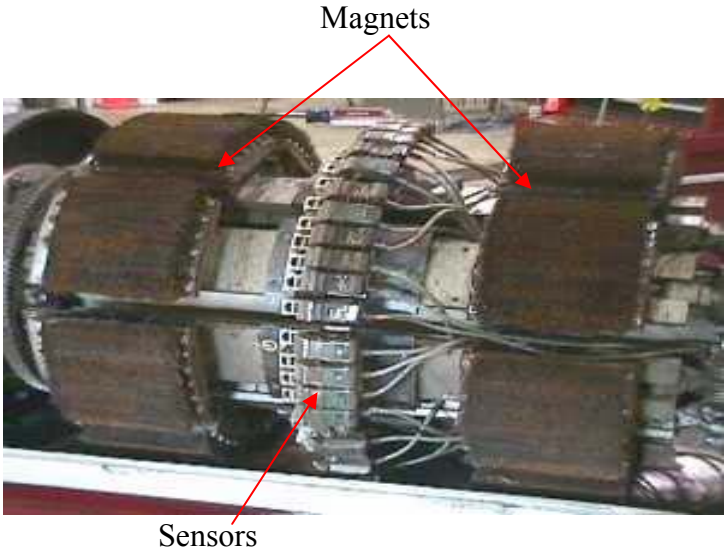

Figure 2.3. Typical magnetic (a) and sensor system (b) in MFL pigs (Nestleroth and Bubenik 1999).

Electromagnets produce a magnetic field by passing a current through a coil of wire, while permanent magnets have a homogeneous charge without external power to operate. This lack of power requirements is a valuable advantage of permanent magnets and makes them the most commonly used magnetism sources in modern MFL tools.

The magnetic system of common MFL tools is comprised of several high-strength, rare-earth permanent magnets. Rare-earth magnets include Samarium-Cobalt (Sm-Co) magnets and sintered Neodymium-Iron-Boron (Nd-Fe-B) magnet. The measure of the magnet's force of attraction is called the magnet's strength and is categorized by a distinguishing characteristic known as maximum energy product (BH_{max}). Nd-Fe-B magnets have a higher BH_{max} than Sm-Co magnets. Thus Nd-Fe-B magnets are the most commonly used magnets in pipeline inspection industry. The Maximum Energy Product can easily reach 30 megagauss-oersted (MGOe) and even goes up to 50 MGOe (MMC 2001). Varying the number of magnets changes the strength of the magnetic field.

The sensor system is a set of sensors that record the leakage field during pipeline inspection. The leakage is transformed into a signal that could be linked to a possible defect and can be later analyzed. The sensor size represents an important parameter because it directly impacts the resolution of the measurement system. All sensors have a length, width, and height and they provide an average measurement of the leakage field passing through the volume of the sensor (Porter 1996).

The most important limitations of a MFL tool are the flow restrictions, the need for large quantities of data that is typically interpreted by humans, and the permanent magnetization left in the pipe steel after pig running. On the other hand, the benefits of the MFL technique are the accuracy of the test-true comparison obtained data and that the tool is capable to chose the level of sensibility according to testing needs: low, middle, high, extra high or newest extra high resolution tools (Nestleroth and Bubenik 1999; Bickerstaff *et al.* 2002).

The *First Generation Tools-Conventional/Low Resolution tools* report internal and external metal loss in bands (in order of magnitude), with no distinction and no sizing. These tools are incapable of accurately assessing against specific pressure requirements. On the other hand, the *Mid-Resolution tools* are capable of discriminating between internal and external anomalies and to producing pressure-based reports.

The *High-Resolution tools* have the highest accuracy due to increased number of sensors, channels, and magnetic levels. The *extra high* and *newest extra high* generation of tools significantly increases the quality and number of small sensors to provide better anomaly sizing and higher resolution. The newest generation includes both inspection directions: circumferential and transversal.

2.2 Magnetism and Magnetic Phenomena In Steel

The modern history of permanent magnets started about 1940 with the introduction of AlNiCo (Aluminum-Nickel-Cobalt, Alnico) magnets. Before this discovery, the use of permanent magnets was limited to a few applications such as the compass and the magneto.

Electromagnets were replaced by permanent magnets after the introduction of Alnico. The use of these magnets became widespread in devices such as motors, generators, loudspeakers, and high-tech inspection tools.

A revolution in the permanent magnetic materials industry stared about 1970 with the introduction of the samarium-cobalt (SmCo) family of hard magnetic materials with astonishing magnetic energy densities. The discovery in 1983 of a less expensive new generation of rare-earth magnets, neodymium-iron-boron (Nd-Fe-B), with even higher magnetic energy densities, accelerated this revolutionary technology. These two families of rare-earth magnets have such high energy densities that they not only replaced, but also have applications not available to high-tech electromagnets (AMT 2002). The most relevant application of this magnet is in the oil and gas pipeline in-line inspection industry.

The interpretation of the magnetization effect on hydrogen damage in pipeline steels is feasible if magnetism and its physics are well understood. A concise description of the magnetic moment (magnetization), magnetism in materials, magnetization curves, ferromagnetism, demagnetizing field, magnetic measurements, and magnetic materials is included in the following Sections.

2.2.1 Magnetic Moment and Magnetization

The magnetic moment, an important and fundamental quantity applied to a bar magnet or to the electronic magnet, is considered the analog of the angular momentum in mechanics. If a bar magnet (dipole) of length l with poles of strength p and $-p$ at its ends is suspended in a uniform magnetic field H, each pole is acted upon by a force that tends to turn it into the field direction (see Figure 2.4). This behavior means that a couple or torque is exerted on the magnet. From Figure 2.4, the moment of the couple or torque is:

$$\tau = (p\, l)\, H \sin\theta \qquad (2.1)$$

where, in the SI system of units (in the cgs system of units), τ is the torque, Amp^2-m (emu-oersted); p the pole strength, Amp-m (emu/cm); l the separation distance of magnetic poles of strength p, m (cm); H the magnetic field, Amp/m (oersteds); and θ the angle apart from the field direction. From conversion tables (Jiles 1998), 1 oersted (Oe) = 79.58 Amp/m and 1 emu/cm^3 = 1000 Amp/m.

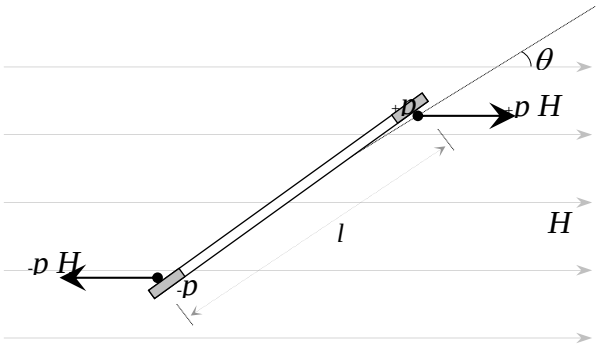

Figure 2.4. Suspended magnet in a uniform field under the action of a couple or torque.

The product, $p\ l$ (Amp-m^2 or emu), is the magnetic moment of the magnet, i.e. if the couple is acting on the magnet when it is at a right angle (90°) to a uniform magnetic field of 1 oersted, the magnetic moment is given by:

$$m = p\ l \tag{2.2}$$

Any force acting on the magnet involves the pole strength p and the length l in the product $p\ l$. If no frictional forces act on the magnet, the work done by the torque in turning the bar magnet through a tiny angle $d\theta$ is reversible, producing a potential energy (E_p, emu-oersted),

$$dE_p = (\ pH \sin \theta\ )\ (l)\ d\theta \tag{2.3}$$

In terms of the magnetic moment m and assuming that potential energy is equal to zero when the magnet is perpendicular to the field (work done by the torque is zero),

$$dE_p = \quad (m\ H \sin \theta)\ \ d\theta\,, \tag{2.4}$$

which integrates to:

$$E_p\ =\ -\ m\ H \cos \theta \tag{2.5}$$

Since the magnetic moment m and the magnetic field H are vectors, Equation (2.5) becomes the dot product of m and H, shown in Equation (2.6).

$$E_p = -\ \boldsymbol{m} \bullet \boldsymbol{H} \tag{2.6}$$

When a magnetic material is subjected to a uniform magnetic field, it becomes magnetized; therefore the magnetic moment per unit volume is called magnetic polarization or intensity of magnetization. The intensity of magnetization, or simply the magnetization, usually denoted by M (Amp/m or emu/cm^3), is the magnitude to which the magnet is magnetized, i.e. the magnetic moment (m) per unit volume of solid (V). Hence,

$$M\ =\ \frac{m}{V} \tag{2.7}$$

2.2.2 Magnetism in Materials

The materials considered in this research, high-strength pipeline steels, are ferromagnetic. Useful examples of how the magnetic behavior of a substance may be measured are presented in some magnetism texts (Du Trémolet *et al.* 2002; Cullity 1972; Jiles 1998). Cullity (1972) considered the Rowland' Ring, a ring sample wound with two groups of wire-based windings (turns of isolated wire) connected to electrical components (switch, ammeter, and ballistic galvanometer), as the circuit for magnetization (see Figure 2.5). This configuration (toroid) has the advantage of being a closed magnetic circuit in which magnetic poles do not appear as the ring material is magnetized. Its principle is based on the comparison of the magnetic flux (Φ,

Weber) produced by the current flowing through the primary winding and the flux obtained from the galvanometer deflection (secondary winding).

When the ring contains any material substance, the calculated magnetic flux is found to differ from that observed in the galvanometer. When the ring is empty, this difference is zero. The magnetism that any material exhibits can be classified as: diamagnetic, paramagnetic or antiferromagnetic, and ferromagnetic or ferrimagnetic.

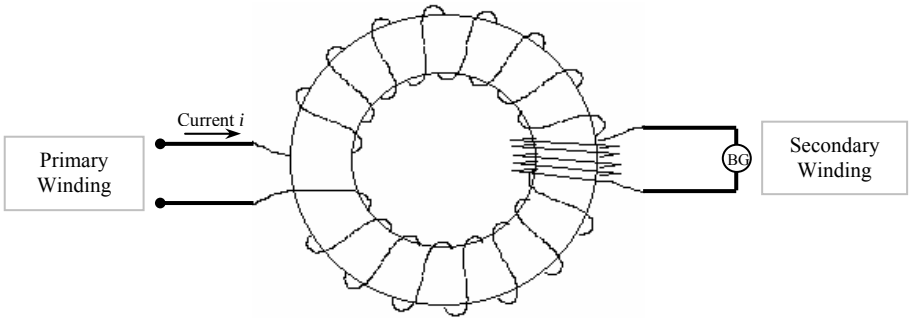

Figure 2.5. Circuit for Magnetization.

The internal mechanisms responsible for the observed magnetic behavior of various material substances are primarily related to the property and nature of the electrons in the atomic structure. The electrons have their own magnetic moment due to their constant orbital and spin angular momentum. The change in the orbital angular momentum caused by any applied magnetic field causes a change in the magnetic moment. The sum of all electronic magnetic moments gives rise to the magnetic moment of the atom, which is an indispensable concept in the magnetic behavior of materials.

There are two essential concepts to consider. They are (a) the presence of a magnetic field in a free environment will always cause the presence of a magnetic flux Φ (i.e., the flux is produced by the presence of a magnetic field in a medium) and (b) the lines of force in a magnetized bar are applicable at macroscopic scale; however, in any internal section of a material, small north-south poles are created by an external applied magnetic field, *H*. These lines of magnetization added to the lines of forces constitute the lines of induction, and the total number of lines of induction per unit area is called the magnetic induction or total flux density, *B,* which is proportional to magnetization, *M,* and magnetic field, *H*. Generally, *B* is calculated from

$$B = \mu_o (M + H) \qquad (2.8)$$

where B is expressed in Tesla (SI system of units) or Gauss (CGS system of units) and μ_o is called the permeability of vacuum (a fundamental physical constant), and has the value of $4\pi 10^{-7}$ Henrys per meter (H/m).

Ferromagnetic materials have been defined as paramagnetic substances with large molecular fields (Chikazumi 1997). However, there is no a single theory to explain

ferromagnetic behavior. There are at least two rather divergent viewpoints: (a) the localized moment theory which declares that the electrons responsible for ferromagnetism are attached to the atoms and cannot move about in the crystal, and (b) the band theory, also called collective-electron theory and itinerant-electron theory. The band theory declares that the electrons responsible for ferromagnetism are considered to belong to the crystal as a whole and are capable of motion from one atom to another (see Section 2.2.6.2.).

2.2.3 Magnetization Curves and Hysteresis Loop

The magnetic properties of a substance are based in the magnitude and direction of the magnetization M as well as the way in which M varies with the applied field H. The ratio of these parameters is called the magnetic susceptibility, χ (dimensionless, SI system of units, or emu/cm^3/Oe, CGS system of units):

$$\chi = \frac{M}{H} \tag{2.9}$$

However, engineering researchers are usually involved in ferromagnetic material investigations and the total flux density, B, produced by an applied field is the main concern. The ratio of B and H is called the magnetic permeability (μ), which in terms of Roland-ring experiment noted in section 2.2.2, is given by the ratio of the obtained flux (galvanometer) and the flux produced by the current. In other words, the degree of magnetization of a ferromagnetic material that responds linearly to an applied magnetic field is defined as magnetic permeability and given by:

$$\mu = \frac{B}{H} \tag{2.10}$$

The most common way to represent the bulk magnetic properties of a substance is by a plot of M/H or B/H ratios and is called a magnetization curve. Normally, the diamagnetic and paramagnetic materials have linear M-H curves that do not show the remaining magnetization once the field is removed. However, the magnetization curve of ferro- and ferrimagnetic materials is nonlinear. The magnetization M increases with increasing field until it reaches a point where the curves flattens, called the magnetization saturation. At high magnitude of the magnetic field (H), M becomes constant at its saturation value of M_s (see Figure 2.6), which is dependent only upon the magnitude of the atomic magnetic moments. Once the magnetic field is removed ($H = 0$), a remaining magnetization (remanence) is left and the irreversibility or hysteresis phenomena appears giving rise to hysteresis loop.

The suitability of ferromagnetic materials for applications is determined principally from characteristic hysteresis loops. Therefore, materials for transformer applications need to have high permeability and low hysteresis losses because of the need for efficient conversion of electrical energy. Materials for electromagnets need to have low remanence and coercivity to ensure that the magnetization can be reduced to zero as needed. Coercivity is the reverse magnetic field necessary to coerce the substance back to zero magnetic induction (see Figure

2.7). Permanent magnet materials need high remanence and coercivity in order to retain the magnetization as much as possible (Jiles 1998).

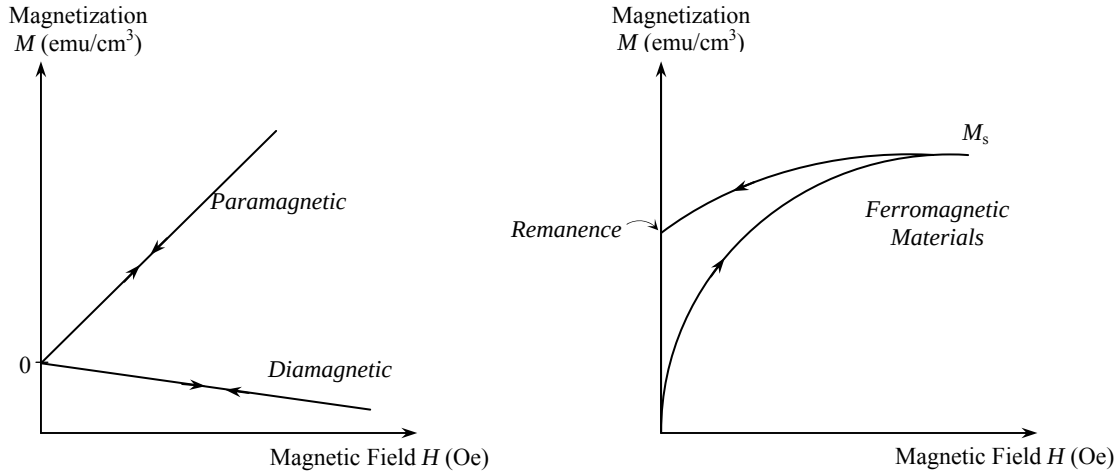

Figure 2.6. Typical magnetization curves of different substances.

The permeability of ferromagnetic materials declines significantly with temperature and both coercivity and remanence become zero at the Curie temperature. All ferromagnetic substances become paramagnetic once a material is heated above its Curie temperature. For example, the transition temperature of iron, nickel, and cobalt are 770, 358, and 1131°C, respectively. The reason for the transition from ferromagnetic to paramagnetic will not be discussed in this work because this phenomenon does not occur in pipeline inspecting operations.

As shown in Figure 2.7, once a magnetic field is applied (a) the substance follows a nonlinear magnetization curve until it reaches its magnetic saturation (b). When driving magnetic field drops to zero (c), the ferromagnetic material retains an appreciable degree of magnetization (remanence). Then, the magnetic field is reversed and increased to a large value to drive the magnetization to zero again (d, coercivity). Thereafter the same amount of magnetic field force is slowly applied in the opposite direction toward the magnetic saturation in the opposite direction (e). When the driving magnetic field drops again to zero, due to the natural retentivity of the material, it will hold a magnetic flux with no magnetic field applied (f, remanence). Finally, the field is re-applied and the flux density reaches its prior value (b) passing first by another coercivity point (g). The hysteresis loop shows the history dependent nature of magnetization of a ferromagnetic material. Once the material has been driven to saturation, the magnetizing field can then be dropped to zero and the material will retain most of its magnetization, i.e. it remembers its history (Nave 2002).

2.2.4 Ferromagnetism

The term *ferromagnetism* is used to characterize strong magnetic behavior, such as the strong attraction of a material to a permanent magnet. The origin of this strong magnetism is the presence, at the microscopic scale, and below the Curie temperature, of a spontaneous magnetization produced by a parallel alignment of spins. It means that all magnetic moments in a

ferromagnetic substance are spontaneously parallel to each other (Chikazumi 1997; Du Trémolet *et al* 2002). In 1907, Pierre Weiss explained the mechanism for the appearance of spontaneous magnetization, assuming that in a ferromagnetic substance there exists an effective field called the molecular field. This strong molecular field acts regardless the Curie temperature of each particular substance, which could be magnetized to saturation by the molecular field even in the absence of an applied field. The substance is then self-saturated or spontaneously magnetized. The intensity of the molecular field, H_m, acting on a material is directly proportional to the saturation magnetization, M_s, by the molecular field coefficient, γ, or

$$H_m = \gamma M_s \tag{2.11}$$

Iron and iron-based alloys (such as steel) are examples of self-saturating materials. Nevertheless, it is possible to obtain a piece of iron in the unmagnetized condition. Weiss also explained why it is probable assuming that ferromagnetic materials in unmagnetized conditions are divided into some very small regions known as *domains*. Two domains are separated by a boundary called a *domain wall*. Every region or domain is spontaneously magnetized to saturation, but the directions of magnetization of all domains are random and as such, the total magnetization of the specimen as a whole is zero.

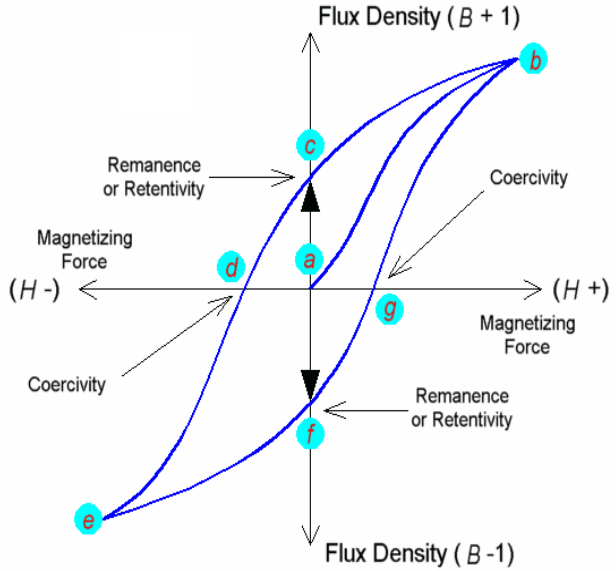

Figure 2.7. Hysteresis loop (after Learn Electronics Tutorials).

From a quantum mechanical perspective, ferromagnetism arises from a positive exchange energy between atomic magnetic moments in partially filled shells. Heisenberg was the first to propose the quantum mechanical exchange interaction between two neighboring electrons with overlapping wave functions. He suggested that between atoms with an electronic spin angular momentum number *Si* and *Sj* there is an interaction with energy equal to the dot product of the spins, as shown in Equation 2.12.

$$E_{EX} = -2 J \boldsymbol{Si} \cdot \boldsymbol{Sj} \tag{2.12}$$

where J is the exchange integral; exchange interaction between two electrons. When the exchange integral is positive ($J > 0$), parallel alignment of the spins is favored (ferromagnetic). In contrast, antiparallel alignment (antiferromagnetic) is favored when the exchange integral is negative ($J < 0$; Berkowitz and Kneller 1969; Chikazumi 1997)..

Bethe, in 1933, found the exchange integral for the electrons on two one-electron atoms as a function of interatomic distances (r_{ab}) and radius (r_d) of the d-shell orbits. In 1930 values of the interatomic spacing and the radii of the partially filled d-shell of some transition metals were published by Slater. Further investigations revealed that the exchange integral becomes positive for the ferromagnetic 3d elements iron, cobalt, and nickel; and negative for the antiferromagnetic elements chromium and manganese as shown in Figure 2.8. The exchange integral becomes also positive for rare earth elements (Jiles 1998).

2.2.5 Magnetic Materials and Hard Magnetic Materials

Engineering applications of ferromagnetic materials are divided into three principal categories: (a) soft ferromagnetic materials, almost exclusively associated with electrical circuit (AC applications), (b) semi-hard magnetic materials, associated with magnetic recording purposes, and (c) hard ferromagnetic materials, associated with permanent magnets. The latter category is extensively described in this section because it is associated with the most common type of magnetic materials used in pipeline MFL inspection tools.

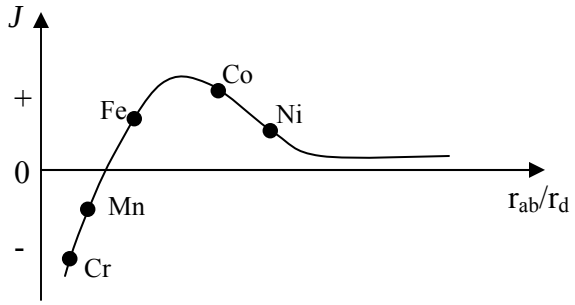

Figure 2.8. The Bethe-Slater curve. The ferromagnetic 3d elements iron, cobalt, and nickel are separated from the 3d antiferromagnetic elements chromium and manganese. The rare earth elements lie to the right of nickel on the curve (after Jiles 1998).

Hard magnetic materials, better known as permanent magnets, are used to provide a magnetic field in a particular volume of space. The principal properties of these materials are their high coercivity field and high residual magnetization. For many engineering applications such as pipeline MFL inspections, permanent magnets are used because they provide a constant magnetic field without both the continuous consumption of electricity and the generation of heat. The magnetic field is maintained due to the energy stored into the magnet when it was previously magnetized or 'charged'. It remains in the magnet indefinitely. Therefore, a high remanence is desirable and, additionally, high saturation magnetization.

The quality of permanent magnet materials is determined by the maximum energy product $(BH)_{max}$, which represent the maximum area under the magnetization curve in the second quadrant of the hysteresis loop (from the remanence to the coercivity point: *demagnetization curve*; see Figure 2.9*a*). Commonly, the maximum energy product of hard magnetic materials is measured in non-standard units of megaGauss-Oersted (MG Oe), where 1 MG Oe = 79,577 ergs/cm^3 = 7.96 kJ/m^3. For efficient use of the magnetic material, the working point of the magnet should correspond to the maximum value of the energy product (Chikazumi 1997). The energy of a magnet is always available for use and is not drained away by repeated use because a magnet does no net work on its surroundings (Cullity 1972).

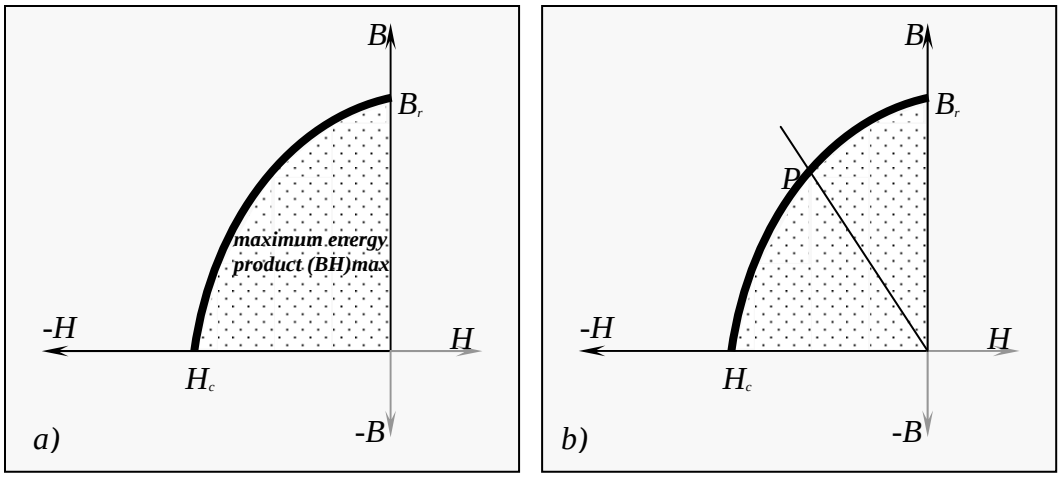

Figure 2.9. Second quadrant of the hysteresis loop: *demagnetization curve* (a). Operating point P of a permanent magnet (b) (after Bray and Stanley 1997).

The desirable properties of permanent magnet materials are typically stated in terms of remanence (noted in Section 2.2.3) and coercivity. A combination of high remanence and high coercivity is necessary in permanent magnets. The coercivity is used to differentiate soft and hard magnetic materials. High coercivity in a permanent magnet is desirable because it requires being highly resistant to demagnetization.

Jiles (1998) points out that the coercivity is defined by either the field at which M is zero (intrinsic coercivity, ${}_mH_c$) or at which the B in the material is zero, ${}_BH_c$. In hard magnetic materials, these quantities have very different values. The greater the difference, the better the material is as a permanent magnet. Since the remanence M_R is the maximum residual magnetization that can be obtained in a closed-loop configuration, the residual magnetization at which the permanent magnet operates in open circuit is always less than M_R. The intrinsic coercivity in neodymium-iron-boron magnets is typically 1.12 MA/m while the remanence is typically 1.05 MA/m, which represent high values if these are compared with other hard magnetic materials.

Materials that are considered hard magnetic materials are grouped in three categories: (a) permanent magnet alloys, (b) compound magnets, and (c) rare earth compound magnets. The most common rare earth compound used in pipeline MFL inspection tools is neodymium-iron-

boron alloy, which has a very large uniaxial anisotropy, high coercivity, and high-energy product. Its high coercivity is because it is difficult to nucleate reverse domains. Once a strong field magnetizes the material, the intrinsic coercivity ($_mH_c$) increases with an increase of the maximum magnetization field (H_M). This phenomenon is considered to be from the elimination of 'magnetic seeds' for the nucleation of reverse domains by the application of the maximum magnetization field (Chikazumi 1997). The maximum energy product $(BH)_{max}$ of neodymium-iron-boron magnets can easily reach 30 megagauss-oersted (MGOe) and even can rise to 50 MGOe.

2.2.6 Magnetic Behavior in Iron and Steel

The ferromagnetic behavior of iron and iron-base alloys is related their atomic and electronic configuration. To describe this magnetic phenomenon, an atomic theory and metallic theory will be discussed.

2.2.6.1 Atomic Theory

Electrons have spin and orbital angular momenta and occupy energy levels or shells. According to the Pauli exclusion principle, two electrons at the same energy level must be of opposite spin.

The quantum numbers (n,l,m_L, and m_S) and letters (s, p, d, f, g, and h) denote the different shells, energy levels, and electron spins that represent the electronic state in an atom. For example, the schematic representation of electronic configuration of the free iron atom is shown in Table 2.1, where ↑ is +½ and ↓ is -½ (spin quantum number). The shell-filling scheme of iron and its neighboring elements in the periodic table is given in Table 2.2. This scheme suggests the magnetic behavior of iron, its alloys, and neighboring elements.

Table 2.1. Schematic representation of electronic configuration of the free iron atom

Shell	Sub-Shell	m_L				
		-2	-1	0	+1	+2
N	4s			↑↓		
M	3d	↑	↑	↑	↑	↑↓
	3p		↑↓	↑↓	↑↓	
	3s			↑↓		
L	2p		↑↓	↑↓	↑↓	
	2s			↑↓		
K	1s			↑↓		

The 3d-band or 3d-state is empty for the two first elements of the 4th period of the periodic table and begins to fill out only after 4s-band is first doubly occupied. In the case of iron, the 3d-band is partially filled out with five electrons with ↑-spin and only one with ↓-spin. When the

number of electrons with ↑-spin is equal to the number of electrons with ↓-spin, the magnetic moment of the electron spin is compensated. Otherwise, it leads to a spin polarization of the atom with a permanent moment. When a strong external magnetic field is applied to a ferromagnetic material such as iron, it develops a major component in the magnetic field direction. That is, at the saturation magnetization the domain configuration of a single crystal show electron spins parallel alignment (see Figure 2.10). In other words, all magnetic moments are aligned parallel. When both electron spins are pointing in the same direction, the net spin is (½) + (½) = 1; i.e., uncompensated, but if they are pointing in opposite directions, the net spin is (½) + (-½) = 0.

Table 2.2. Shell-filling scheme of iron and its neighboring elements

Shell	Sub-Shell	K	Ca	Sc	Ti	V	Cr	Mn	Fe	Co	Ni	Cu	Zn
M	3s	2	2	2	2	2	2	2	2	2	2	2	2
	3p	6	6	6	6	6	6	6	6	6	6	6	6
	3d			1	2	3	5	5	6	7	8	10	10
N	4s	1	2	2	2	2	1	2	2	2	2	1	2

Based on the quantum mechanic exchange energy concept introduced by Heisenberg (Chikazumi 1997) and Coulomb's law, it is said that even though electrons always repel each other because of the presence of electric charges, the exchange energy or exchange force is repulsive for electrons with parallel spins and attractive for electrons with antiparallel spins. The number of neighboring atoms and how they are configured in the metallic crystal structure influence the strength and the nature of the exchange energy. Some other influencing factors are the intratomic spacing (atomic radius) and the interatomic spacing (lattice spacing).

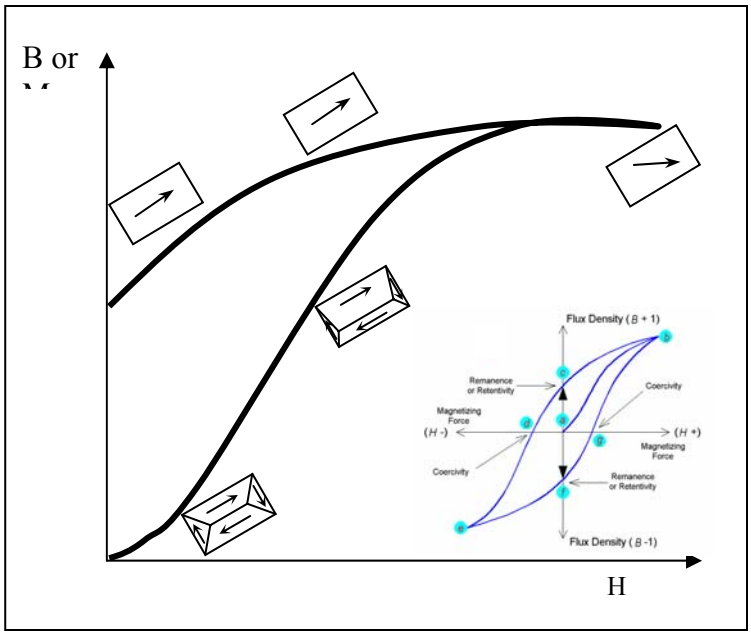

Figure 2.10. Domain configuration of a single crystal under the magnetic field H (after Cahn-Haasen 1996).

Some authors consider that the repulsion of electrons with parallel spins produce a larger separation than in the case of electrons with antiparallel spins. In contrast, based on Hubbard model (Du Trémolet *et al.* 2002), others consider that an electron can jump to a nearest neighbor creating an empty space and a double occupancy on the nearest neighbor. Either theory shows that electrons with parallel spins distort the metal lattice.

2.2.6.2 Metallic Theory

The 3*d* transition metals iron, cobalt, and nickel are the only metallic elements where ferromagnetism occurs. Ferromagnetism occurs also in rare-earth metals. Some of these rare-earth elements are gadolinium (Gb), terbium (Tb), and dysprosium (Dy). Because, at room temperature, the transitions metals exhibit spontaneous magnetization, some alloys containing these elements are used as magnetic materials. The 3*d* electrons and 4*f* electrons are the carriers of magnetism in transition metals and rare-earth metals, respectively. The magnetic moments of the 4*f* electrons are localized at individual atoms and the magnetic moments of 3*d* electrons are localized among the atoms. This behavior is because 4*f* electrons are located deep inside the atoms and 3*d* electrons are moving far from the atomic nuclei. The 3*d* electrons are moving between the atoms and form a band structure; i.e. these conduction electrons are itinerant and are not bound to a specific atom nucleus. In magnetic alloys that contained these transitions elements, the 3*d* electrons also are responsible for their magnetic moments. But in this case, 3*d* electrons form the band structure together with the 4*s* electrons (Chikazumi 1997). It is known that in solids, a band structure result from the overlap of atomic orbitals. In other words, the formation of these bands (energy bands) is derived from the fact that no two electrons can exist in the same energy state or quantum state (Pauli exclusion principle; Ibach and Lüth 1995).

From the atomic viewpoint, the strength of the energy levels of the electrons bounded to the atom nucleus decreases as the distance from the nuclei increases. This strength or potential energy, E, increase asymptotically with increasing the distance, as is shown in Figure 2.11a. But, in the crystal lattice the potential energy behavior changes. The total potential energy sum up the potential energies from individual itinerant electrons (see Figure 2.11.b). The strength of the exchange coupling governs the width of the band (energy state). The outer electrons, which form a uniform and continuous band, move freely within the whole crystal lattice (Pepperhoff and Acet 2001).

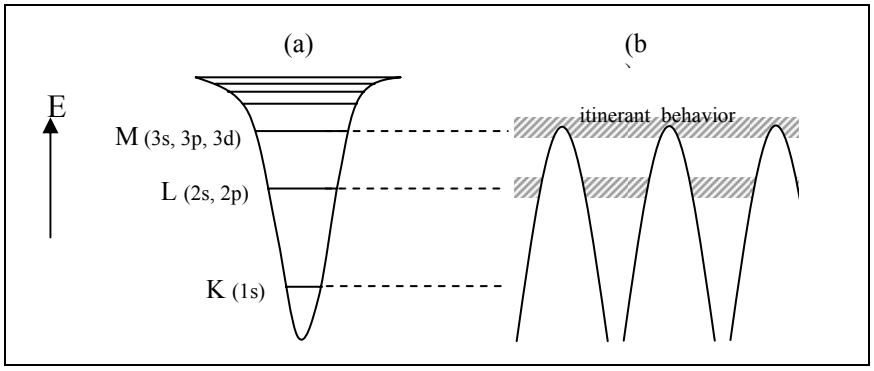

Figure 2.11. Potential energy scheme (a) for a single atom and (b) for a crystal lattice in which the electrons form a band (after Pepperhoff and Acet 2001).

In transition metals the d-energy state is narrower (higher density of states) than the s-energy state of valence electrons, because when the atoms approach one another, the lower energy level gets wider faster than the higher energy level (see Figure 2.12). The d-band, with ten electronic states per atom, is overlapped by the s-band, with only two states. The result of the overlapping is the high density of states, N(E). Because of the Pauli principle, the conduction electrons start in filling the lowest energy state and fill higher energy states until the filling of all these conduction electrons, which is the Fermi energy or Fermi level, E_F. The Fermi level dictates the ferromagnetic property of materials, and all the energy states above it are empty. The transition metals have the d-band partly filled. The hatched area of Figure 2.12 is the number of occupied 4s and 3d-states in transition metals (Berkowitz and Kneller 1969; Tanner 1995; Kittel 1953).

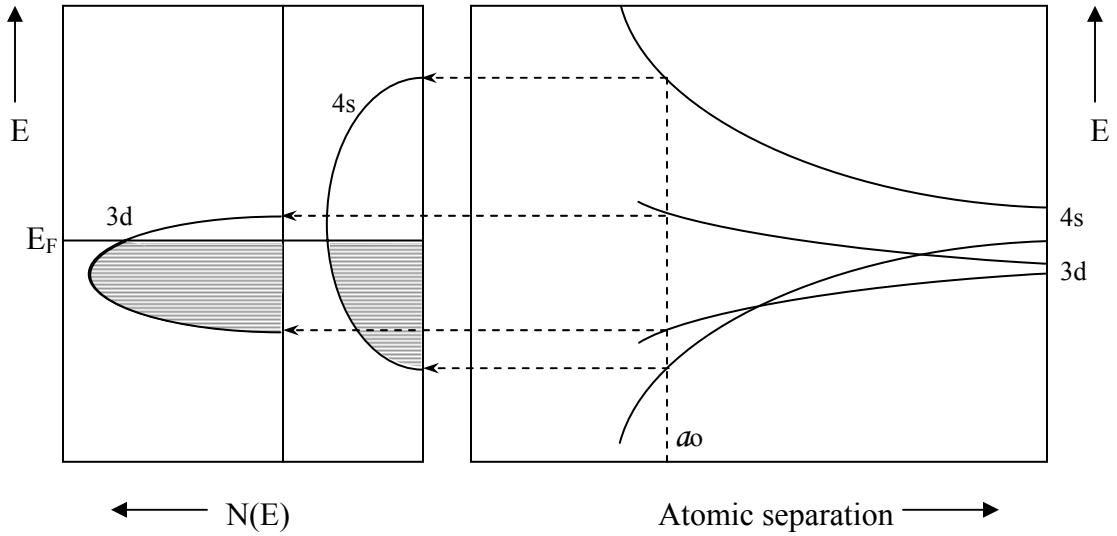

Figure 2.12. S-band and d-band in transition metals. Representation of the s-band and d-band as a function of atomic separation. The resulting density of states at the equilibrium separation is a_o. The hatched area denotes the occupied states below Fermi energy, E_F (after Pepperhoff and Acet 2001).

The occupied state below the Fermi energy in Figure 2.12 can be split into two identical sub-bands, with 5 electronic states per atom each. These two sub-bands or half bands, which represent the two possible spin orientations, ↑-spin and ↓-spin, can be occupied up to a common E_F (see Figure 2.13a). The number of electrons in both sub-bands is the same.

Under the influence of a magnetic field the electrons of a half band follow the magnetic field direction producing a shift in energy of one band respect to the other (see Figure 2.13b). This behavior is called ferromagnetic exchange interaction or exchange splitting. The Fermi energy level is different in both half bands; one d-band is full with 5 electrons, while the other is partly filled (Jelis 1991; Berkowitz and Kneller 1969; Tanner 1995; Pepperhoff and Acet 2001).

Because of the Pauli principle, electrons with parallel spins avoid each other. So, the chance of detecting an electron close to another electron with opposite spin is much bigger than an electron with similar spin. The spontaneously magnetized state becomes stable because of the

parallel orientation of the spins. This orientation is favored by the repulsive interaction between the electrons. At the same time, the potential energy is reduced. In other word, the sub-bands can exchange electrons without the cost of energy.

The Pauli principle is one of the Hund's rules, which are a set of guidelines that facilitates the determination of the quantum numbers for the ground states of atoms. The Hund's first rule states that in a given shell, electrons try to maximize the total spin, consistent with the Pauli exclusion principle. The reason is that the electrons tend to take different orbits (Coulomb repulsion). Also, the interatomic spin-spin interaction tends to align these pins parallel to each other. Once the first rule is satisfied, the second rule states that electrons maximize the total orbital angular momentum (L) within the restriction of the Pauli exclusion principle. The third rule states that the electrons choose a value of $J = L +/- S$ (- for less than half full, + for more than half full) within the restriction of the conditions one and two. This rule is aimed at maximizing a favorable spin-orbit interaction (Chikazumi 1997).

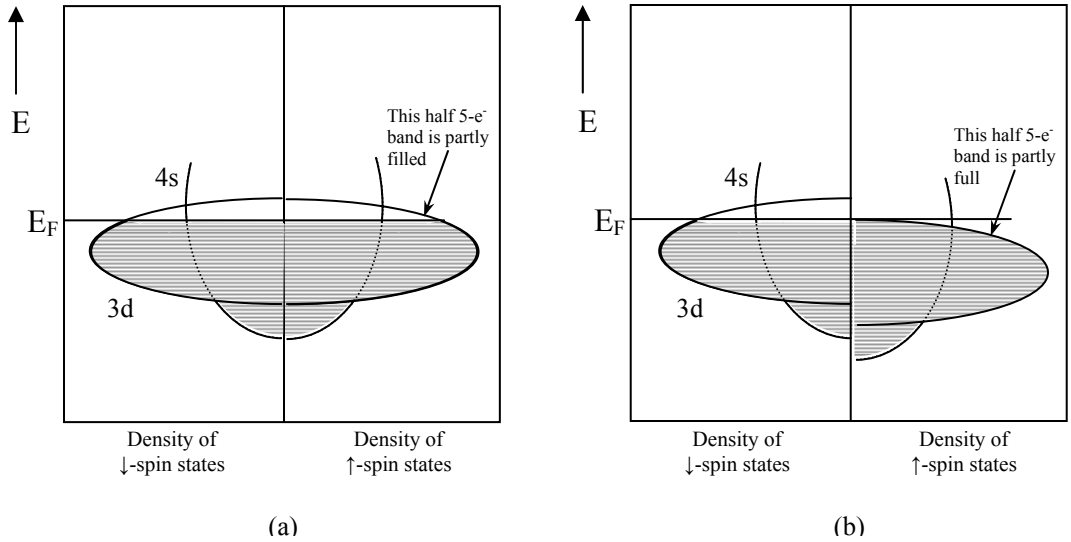

Figure 2.13. The relation of the bands in transitions metals with (b) and without (a, nonmagnetic state) the ferromagnetic exchange interaction. The hatched area is the occupied regions and the s-band can contain a maximum of two electrons, the d-band ten electrons (Berkowitz and Kneller 1969; Tanner 1995).

Figure 2.13 shows the spin configuration in transition metals before and after a magnetic field is applied. This spin configuration is one of the two factors needed by metals to achieve ferromagnetism. The number of ↑-spin electrons is much higher than the number of ↓-spin electrons in the elements from manganese (Mn) to nickel (Ni) in the first row of the transition series. This behavior is the maximum uncouple d-electrons configuration and occurs at the atomic level. However, in the solid level there is a second factor which is the space between atoms or the inter-atomic space. Some atoms can experience a localized uncoupled electron arrangement but the distance of near atoms is too great to get captive coupling between atoms to achieve ferromagnetism. This situation is what happens in some elements of the second row of the transition series.

2.3 Magnetic Flux Leakage Technique In Pipeline Pigging Inspection

This section discusses the basics for understanding of Magnetic Flux Leakage techniques as applied in pipeline inspection. Magnetic Flux Leakage (MFL) techniques are based on magnetizing a specific section of a ferromagnetic material and mapping its surface with some type of flux-sensitive sensor for field leakage. Because the technique generally needs no mechanical contact with the part being evaluated and is amenable to automatic signal recognition schemes, MFL techniques have the advantage of automated, and high-speed inspection. The performance of this method depends on variables including fluid flow velocity, variations in the pipeline material, and pipeline operating pressure.

2.3.1 Classification of Magnetic Inspection Techniques

A magnetic field testing technique is a method in which the magnetic field involved is static, oscillates at low or high frequency. High-frequency methods are classified as microwave radiation, nuclear magnetic resonance, and electron paramagnetic resonance. In magnetic methods, either currents of low frequency or currents of high frequency are used. For example, eddy current methods (high-frequency currents) are treated as a magnetic field method because of their associated techniques of measurement and scanning magnetic fields. Another well-known magnetic field method is the 'magnetic particle method' which indirectly shows the condition of the field from the distribution of magnetic particles on the surface of the tested material.

The magnetic-field-based nondestructive evaluation method described in this section is the magnetic flux leakage technique. This method exploits electromagnetic phenomena in assessing the state or condition of the material (part) being tested. The method directly measures the magnetic phenomenon being exploited (Bray and Mc Bride 1992).

2.3.2 Magnetic Parameters in Magnetic Inspection Techniques

Pipeline materials are basically low-carbon steels (ferromagnetic alloys) and are covered by the manufacturing line pipe standard, API Spec. 5L. The parameters of saturation (B_s or M_s), remanence (B_r or M_r) and coercivity (H_c) of these steels depend on the particular chemical composition, heat and rolling treatment, residual stresses, and density of inclusions.

A rule of thumb is that approximately three times the value of the steel coercivity (H_c) is needed to magnetize common low carbon steels for the purpose of magnetic testing. However, often one can find values outside these typical value ranges. These typical values for industrial steel are: B_s=1.4-1.8 Tesla (14,000-18,000 Gauss), H_c= 2,785-15,915 A/m (3.5 – 20 Oe), and B_r=0.3-1.5 Tesla (3000-15,000 Gauss; Bray and Stanley 1997).

2.3.3 Magnetic Flux Leakage

The magnetic flux leakage (MFL) technique is initiated by an outside artificial strong magnetic field generated by magnets. The sensors detect any anomaly in the magnetic field. In other words, the magnetizing system of the MFL tool creates a magnetic field in the pipeline

steel near the saturation flux density that interacts with steel anomalies to produce local changes (leakage) in this applied field that are physically close to the pipe surface (see Figure 2.14). Although this change in magnetic property reduces the local ability of the pipe steel to carry a magnetic flux, the presence of an anomaly does not guarantee that flux will leak. As an example of this phenomenon, corrosion processes change the ferromagnetic pipe steel into non-ferromagnetic iron oxide with an evident change in the applied magnetic field, but the reduction in material alone may not cause flux leakage because the remaining material will still be able to carry the complete magnetic flux. In consequence, the interpretation of MFL signals is an important constituent in this in-line inspection technique.

The principle of magnetizing requires that the magnetic field should be uniform, consistent and strong enough to cause a measurable amount of magnetic flux to seep out from the pipe at local anomalies. The uniformity of the magnetic field through the pipe wall and its consistence along the pipeline length is needed to produce accurate linear signals and to make possible adequate comparisons among different local measurement, respectively.

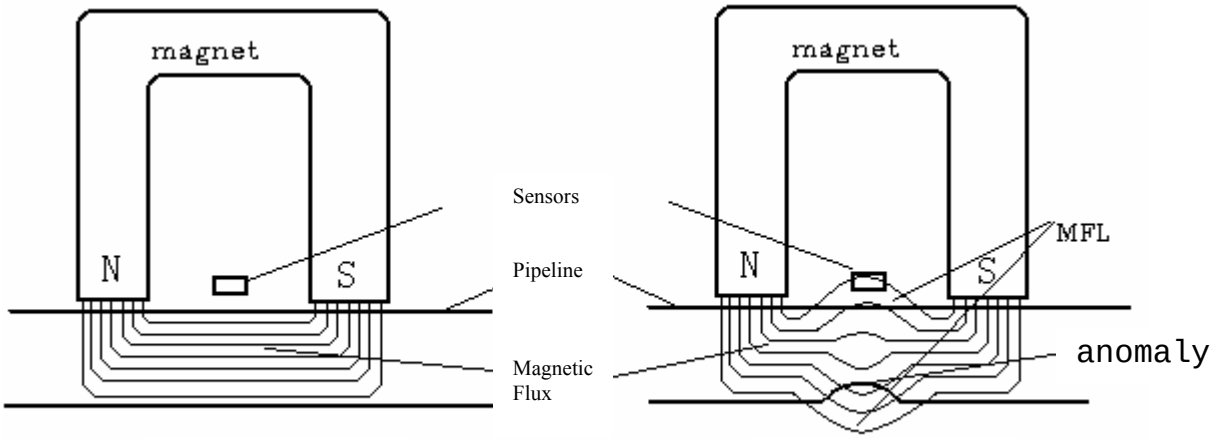

(a) without anomaly (b) with anomaly

Figure 2.14. Magnetic field in the pipeline steel created by a Magnetic Flux Leakage tool (without anomaly, a) and local changes or leakage in this applied field close to the pipe surface due to an anomaly (with anomaly, b) (after Yang *et al* 2001).

Two important variables that impact magnetization are the applied magnetic field intensity (*H*) and the flux density (*B*, or magnetization *M*) in the pipe material. The relationship between both variables is nonlinear in ferromagnetic materials, as was explained in Section 2.2.2. There is a relatively smaller magnetic flux increase at the higher magnetic field intensity than for the same change in flux at lower field intensities. The ratio of flux density and magnetic field intensity of the steel magnetization curve is known as the magnetic permeability of the alloy. Ferromagnetic materials such as low-alloy-carbon steels, which are normally attracted by a magnetic field, have an extraordinary permeability. However, the permeability of ferromagnetic materials changes with the magnetic field intensity and can only be considered constant for relative small change in it. Additionally, a narrowing in the pipe wall thickness causes a reduction of the magnetic permeability of the material producing the flux to leak in alternative direction.

MFL tools are usually designed to create different magnetization levels. In corrosion based metal-loss systems magnetic saturation is applied in the pipe wall thickness in which a narrowing in material will cause flux leakage, while in mechanical damage systems, the MFL tool is designed to produce lower magnetic intensity degrees. In addition, pipe wall thickness is another measurement for MFL tools. Nestleroth and Bubenik (1999) point that variations in wall thickness will change the applied magnetic field intensity, i.e. for heavier wall thicknesses, stronger magnetic field intensity is needed (see Figure 2.15).

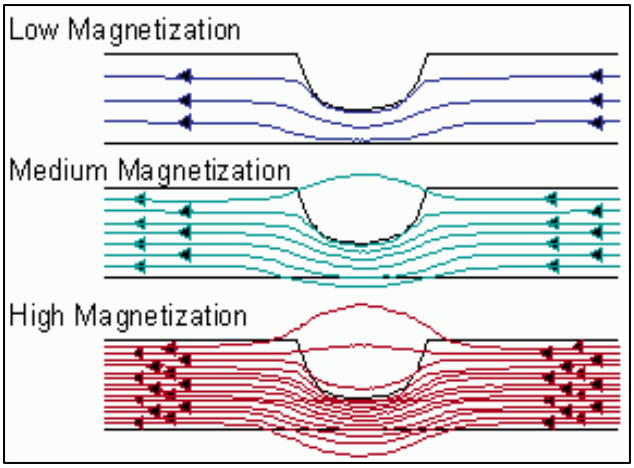

Figure 2.15. Pipeline wall thickness effect on applied magnetic field intensity (after Nestleroth and Bubenik 1999).

The induced magnetic field intensity is affected by other parameters as well, such as variation of material properties, characteristics of magnet-pipe wall contact, MFL tool velocity, and remnant magnetization. As proposed in this research, the remanent magnetization is the most influential factor.

From pipeline inspection standpoint, the remanent magnetization is the magnetic flux density degree left behind in the pipe material after a MFL tool inspection. The remnant magnetization significantly influences the detection and characterization of metal-loss regions. Based on the principle of hysteresis, when the induced magnetic field is removed a magnetization level is locally left in the pipe. Once the pipe steel is re-magnetized, the magnetization curve begins at applied magnetic field intensity equal to zero and a magnetic flux density equal to the remanent flux density.

Figure 2.16 schematically explains the basics of this phenomenon in pigging operations. Because remanent magnetization changes the applied flux levels, it also affects the flux leakage field and the ability to detect and characterize metal loss. The effect of remanent magnetization is a function of defect geometry and number of repeated magnetizations. The remanent magnetization effects reach a limit after 3-5 magnetizations, where flux leakage fields significantly drop (Nestleroth and Bubenik 1999).

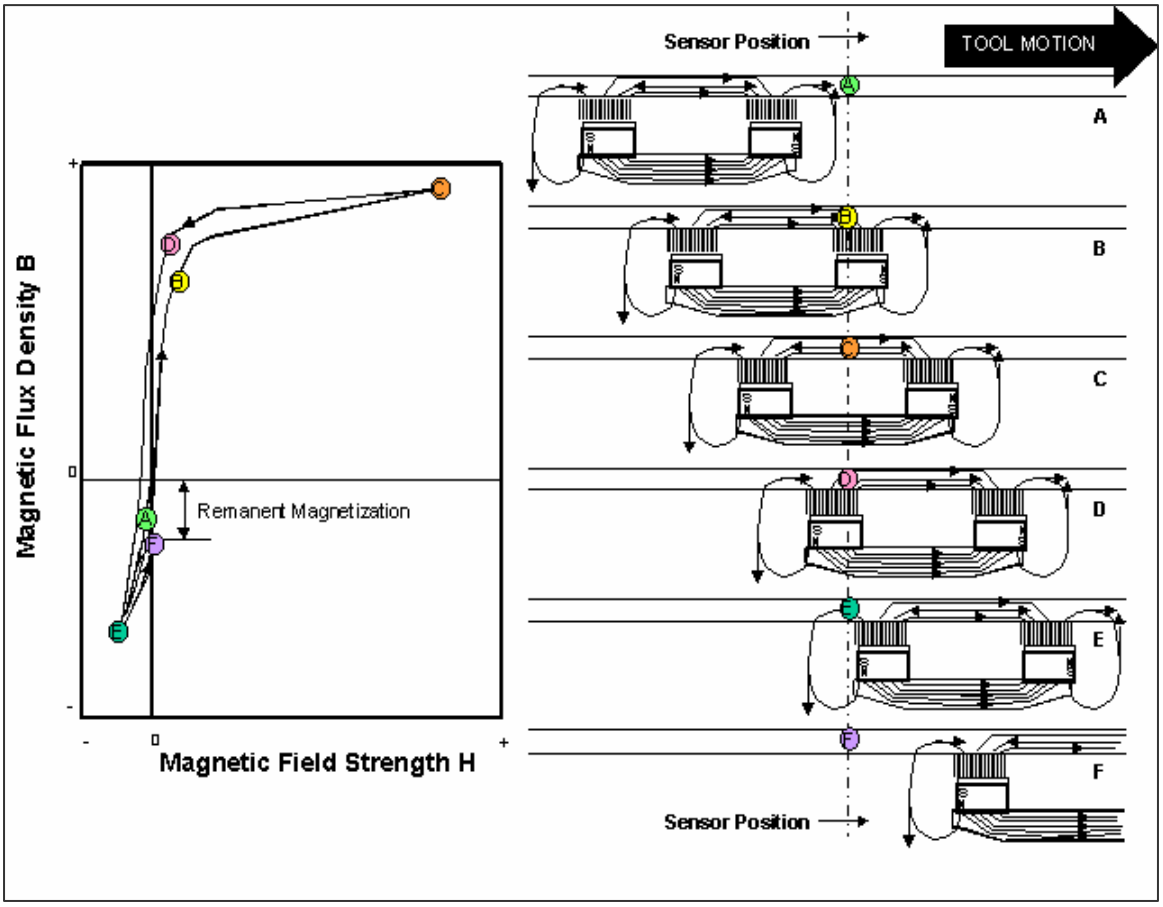

Figure 2.16. Basics of remanent magnetization phenomenon in pigging operations (after Nestleroth and Bubenik 1999).

3. EFFECTS OF HYDROGEN IN PIPELINE STEELS

In this chapter, the hydrogen solubility, diffusion, permeation, removal, and sources, as well as the phenomenology of hydrogen damage in steel are discussed. This discussion is focused on the principal subject related to the hydrogen damage mechanism encountered in this research because of the effect of magnetic flux leakage inspection method.

Hydrogen is possibly the most studied element in the application of metallurgical phenomena in the oil and gas industry because its ubiquitous presence in solution in iron and steel. Hydrogen is a problem in steel because hydrogen is highly mobile as an atom and can both diffuse through the metal crystal lattice and be transported by the movement of dislocations (defects in the metal crystal structure).

3.1 Hydrogen Solubility

The concentration of a diatomic gas such as hydrogen (H_2, the lightest nuclear isotopes) in metals is proportional to the square root of its observed pressure (Sieverts' law), as following

$$C_H = k\,(P_{H2})^{1/2} \qquad (3.1)$$

where C_H is the concentration of hydrogen, k is a constant, and P_{H2} the partial pressure of hydrogen. Sieverts' law, based on the thermal equilibrium reaction of atomic and molecular hydrogen, defines k as $\alpha e^{(-\Delta H/RT)}$, where ΔH is the enthalpy change. However, Hirth (1980), based on a compendium of experimental data, suggests $k=0.00185 e^{(-3440/T)}$, where T is in ºK.

This effect of pressure makes the solubility, *S*, of hydrogen in iron a pressure-dependent function; however, two more parameters affect it: crystal structure (basically, face centered cubic, FCC, or body centered cubic, BCC) and temperature.

From the iron-hydrogen system equilibrium diagram (Figure 3.1), it is well known that the solubility of hydrogen in liquid iron is higher than the solubility in any solid phase of iron. This situation is because the liquid phase is unstressed and, obviously, there is no lattice distortion to limit the occupation of the interstitial places (Pepperhoff and Acet 2001). The solid solubility in FCC γ-iron is higher than in BCC α-iron. Increase in temperature of the system increases hydrogen solubility in both phases.

At temperatures above 400ºC, dissolved hydrogen is contained as atomic hydrogen in the interstices of the metal lattice. On the other hand, at lower temperatures, an excess of hydrogen is observed (it is interstitially insoluble), which is retained in other sites in the steel commonly referred to as "traps". Interrante (1982) states that the hydrogen content, the apparent solubility or measured solubility, can be greater than the solubility limit of the lattice and the excess amount of hydrogen is trapped in various sites that apparently do not affect solubility at high temperature. Further, at room temperature, the dissolved hydrogen may be only a small fraction of the total hydrogen content.

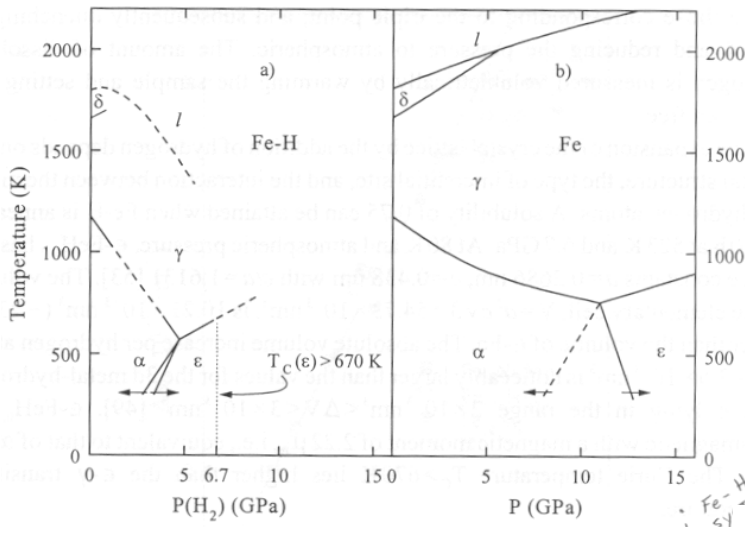

Figure 3.1. Pressure-Temperature diagram of iron and iron-hydrogen Pepperhoff and Acet 2001).

The apparent solubility of hydrogen in steel is considerably increased by factors such as the presence of nonmetallic inclusions and cold working because they tend to increase the number of trapping sites or the volume of internal voids. In other words, the saturation concentration of hydrogen (effective hydrogen pressure) in steel increases with the amount of cold work. For example, hydrogen concentration in low-carbon, low-strength steels may increase up to four times after forty percent cold work (Huang and Shaw 1995). Other external factors that affect the effective hydrogen pressure in the system can significantly act on the saturation concentration and the rate of absorption of hydrogen into the steel. The effective pressure of hydrogen at acid range is greater than that at pH above 8 (basic range).

3.2 Hydrogen Diffusivity

Diffusion is a kinetic process that leads to the homogenization, or uniform mixing, of the chemical components in a phase. Diffusive mixing in solids occurs on the atomic or molecular level. As time increases, the extent of homogenization by diffusion also increases, and the length scale over which chemical homogeneity persists within a phase gradually extends to macroscopic distances. Diffusion that results in the net transport of matter over such macroscopic distances is considered to be a non-equilibrium process. But the phase eventually achieves full thermodynamic equilibrium when transport ceases (Glicksman 2000).

Since the hydrogen molecules are relatively large as compared to the metal crystal lattice only the smaller atomic form of hydrogen can diffuse effectively through the steel lattice. The migration of atoms from one part to another of the lattice represents the primary cause of the movement of hydrogen inside the steel. The hydrogen atom dissociates into a proton and an electron, $H^o \Leftrightarrow H^+ + e^-$, in the metal.

The protons occupy interstitial positions and the electrons are introduced into the d-band of the metal. Relative to the size of the interstitial sites, the protons are vanishingly small. However, the positive charge of the protons has to be screened to preserve electrical neutrality.

The screening occurs by the formation of an electronic cloud of atomic dimensions. However, the screening is not perfect, and repulsive forces occur between the proton and the neighboring positively charged metal nuclei. This leads to a local expansion and thereby a significant distortion of the lattice increasing, in consequence, the number of hydrogen trapping sites. Therefore dissolved hydrogen in metals implies a proton with a screening electron cloud (Pepperhoff and Acet 2001).

The driving force for the diffusion of hydrogen is the gradient in the chemical potential. This potential gradient results either from a gradient in the lattice hydrogen concentration or from a gradient in the hydrostatic component of an elastic stress field (Interrante 1982). The hydrogen migrates from a region of high chemical potential (e.g. higher interstitial concentration) to a region of low chemical potential until the equilibrium is achieved. In addition to the gradient in the chemical potential, both a gradient in an electric field and a gradient in temperature may motivate the diffusion of hydrogen in steel. Therefore, the degree of diffusion is affected by the hydrogen concentration and the lattice diffusivity, *D*.

Dislocation, notches, cracks, inclusions, and bent zones are considered elastic stress gradient factors. These factors act as driving forces for diffusion of hydrogen. These elastic stress fields are called regions of biaxiality, into which the hydrogen diffuses. In this instance, they are tensile in character.

In the regions of biaxiality, the energy of the interstitial hydrogen is higher than that in the regions of triaxiality. The regions of triaxiality are known as regions of locally increased solubility because hydrogen atoms diffuse preferentially into these regions. It means that the bigger the triaxial component, the greater the amount of hydrogen that diffuses. Once external stresses are released, regions of triaxiality reduce absorption of hydrogen and local super-saturation can be achieved. Therefore, precipitation of hydrogen from the solution in the lattice is possible as well as a chemical reaction.

The lattice diffusivity, D (sec^{-1}) can be related to the hydrogen pressure and temperature (TºK, absolute temperature) by the Arrhenius equation

$$D = D_o e^{-Q_g/RT} \qquad (3.2)$$

where D_o is a pre-exponential term (sec^{-1}; effect of hydrogen pressure), *Q* is the activation energy (kJ mol^{-1}), and R the universal gas constant (8.314 x 10^{-3} kJ $mol^{-1}K^{-1}$). Hydrogen solubility is lowest in the BCC α-iron and it is noticeably higher in the FCC γ-iron and even higher in the DHCP ε-iron. Therefore, the lattice diffusivity of hydrogen in latter phases (ε and γ) is much lower than in α-phase. Lattice diffusivity is still lower in austenitic stainless steel because of the relatively high alloy content.

Glicksman (2000) points out that hydrogen diffusion in metals occurs under a wide variety of environmental interactions: aqueous corrosion, electrolysis, electroplating, and welding. In many of these processes and applications cold-worked metals are used due to their high dislocation density.

3.3 Hydrogen Trapping

The energy of motion, G_m, of the hydrogen atom and the features of the traps control both the jump probability of the hydrogen atoms and the tendency of hydrogen to be trapped. Microstructure consisting of a uniform distribution of fine and strong hydrogen traps can increase the hydrogen attack resistance of an alloy. The relationship of the energy of motion and the positions of the hydrogen atom moving through a series of equilibrium positions in a lattice is represented by the sinusoidal line shown in Figure 3.2, where the E_d (proportional to the activation energy, Q) is the amplitude of this wavy line.

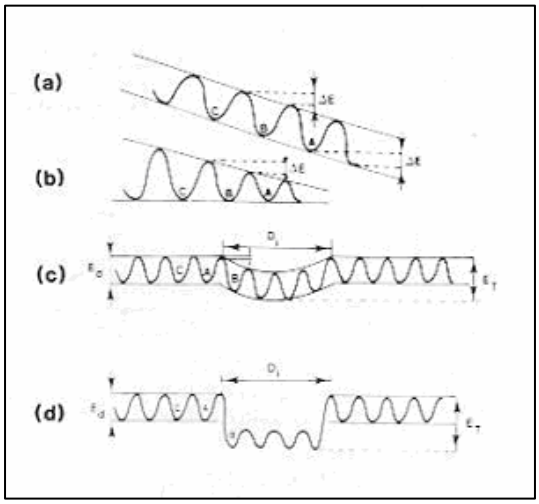

Figure 3.2. Schematic of energy steps necessary to the diffusion of hydrogen atoms through a metal lattice (after Interrante 1982).

Pressouyre (1979) states that when a hydrogen atom jumps from a normal lattice site into a trap (where hydrogen will be accumulated internally as trapped H_2 molecules), the probability of an eventual return to the former site decreases. There are two main reasons why in a crystal lattice, jump probabilities would be modified. There are driving forces (for diffusion) that push the hydrogen atom into a preferential direction, making it more facile, and thus more probable, for the atom in the point B to jump (forward) to point A than to jump (backward) to point C (see Figure 3.2a). Therefore the atom is preferentially attracted to site A. In that case, the lattice is not modified. However, the lattice may be completely modified (see Figure 3.2b), i.e. the average jump height is changing from site to site, and the frequency is affected. In this case the forward jump is made easier by the lattice being stretched open in tension.

The energy of the trap, E_T, and the features of the trap govern the tendency of the trap to hold hydrogen atoms. There are two extreme types of traps: (a) attractive traps (see Figure 3.2c), and (b) physical traps (see Figure 3.2d). Attractive traps are regions of the lattice where the hydrogen atoms are subjected to attractive forces (electrical fields, stress fields, temperature gradients, and chemical potential gradient). A physical trap is a modification of the ideal crystal lattice where energetic conditions make it more favorable for hydrogen to stay. Consequently, it is less difficult for a hydrogen atom to jump out from an attractive trap than from a physical one for the same energy value, E_T. An attractive trap is considered a reversible trap where hydrogen

atom can easily either enter or leave. The amount of hydrogen atoms trapped at any confined site depends of the driving forces, the local concentration of hydrogen, and the characteristics of the traps. The traps in which the hydrogen atoms are trapped can build up without restraint (i.e., large hydrogen concentration) and are called unsaturable traps (see Figure 3.3).

In metals containing a large concentration of lattice hydrogen, the trapped H_2 pressures can approach enormous values. The equilibrium between the trapped molecular hydrogen in an unsaturable trap and the lattice atomic hydrogen is governed by the common dissociation reaction shown here:

$$2H^{+}_{(lattice)} + 2e^{-} \Leftrightarrow H_{2(trapped).} \qquad (3.3)$$

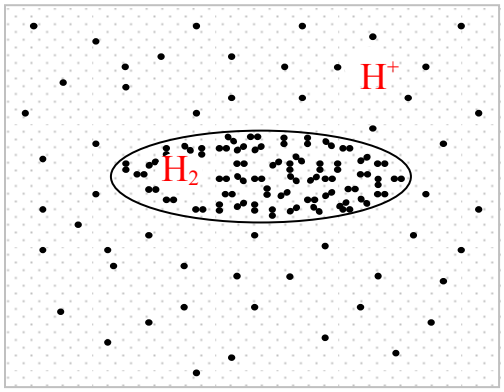

Figure 3.3. Trapped H_2 molecules in a trap surrounded by a lattice saturated with interstitial H^+.

The valence band of the metal (to which electrons from molecular hydrogen dissociation travel) cedes the required electrons to balance the ionization in the trapping reaction and neutralize the interstitial protons. Iron and its alloys are capable of dissolving high concentration of lattice hydrogen showing a high density of electronic states in their *d*-bands. Glicksman (2000) shows that the concentration of molecular hydrogen in traps and the concentration of H^+ in interstitial sites, can be related through the well-known mass-action principle applied to the dissociation reaction. The law of mass-action states,

$$K(T) = [H^{+}]^2 / [H_2] \qquad (3.4)$$

where $[H_2]$ represents the concentration of trapped molecular hydrogen, C_{H_2}, $[H^+]$ is the concentration of protons, C_{H^+}, dissolved interstitially in the lattice, and $K(T)$ is the equilibrium constant. Therefore, the equilibrium constant for the dissociation reaction may be expressed as the concentration ratio of dissolved lattice hydrogen to molecular hydrogen,

$$K(T) = (C_{H^+})^2 / C_{H_2} \qquad (3.5)$$

Insofar as the hydrogen within the metal resides in two distinct forms (trapped molecular H_2 and untrapped H^+), Fick's second law for the overall diffusion of hydrogen in the material is modified. The Fick's second law specifically relates the time variation of the total hydrogen concentration (trapped H_2 plus the untrapped protons) with the divergence of the flux of mobile

hydrogen (H^+ only). The relationship at low temperature of the experimentally observed diffusivity, D_{eff}, and the lattice diffusivity, D_{H^+}, is given by

$$D_{eff} = D_{H^+} C_{H^+} / 2 C_{H_2} \quad (3.6)$$

Johnson and Lin (1980) show that there is another important class of potential trapping sites called *saturable traps*. The most common saturable traps in steels are dislocations, impurity atoms, and internal interfaces. Plausible physical arguments suggest that the capacity for hydrogen of these traps is finite. Based on this model, the trapped hydrogen concentration is saturated as the lattice hydrogen concentration increase. The saturation concentration is equal to the trap density. In this case the diffusion kinetics, especially at low temperature and low lattice concentration, is governed by the trapped concentration.

In summary, Pressouyre (1979) classifies hydrogen traps in steels according to size:

- Point (element such as Mn, Cr, Ti, Nb, etc.),
- Linear (dislocations),
- Planar or bidimensional (particle interfaces, grain boundaries, etc.),
- Volume (voids, cracks, and particles).

Jones (1996) states that these traps may be reversible or irreversible, depending on whether the trapped hydrogen is easily released (time necessary to reach some critical local hydrogen concentration) or tightly bound, as measured by the interaction energy listed in Pressouyre classification. In addition, the traps may be mobile (dislocations) or stationary (solute atoms, particles, grain boundaries).

3.4 Hydrogen Permeation

The diffusant, in many steady-state diffusion processes, is a gas that is forced onto the free surface of the material by application of different partial pressures, which result in different equilibrium concentrations inside the solid. The local solid-gas interface equilibrium conditions (equal thermodynamic activities) control the steady-state solubility of the diffusant at the surface. In the solid-gas interface the dissociation reaction of gas molecules take place in order to form single species that can more easily enter the solid. Since the hydrogen gaseous diffusion (permeation) into the solid is preceded by the dissociation reaction

$$\tfrac{1}{2}H_{2(gas)} \Leftrightarrow H_{(solid\ solution)}, \quad (3.7)$$

the mass-action law is considered to determine the equilibrium constant ($K=e^{-\Delta G^o/RT}$) of this reaction:

$$K(T) = [H] / [H_2]^{1/2}, \quad (3.8)$$

which is equivalent to the Sieverts' law (Glicksman 2000):

$$K(T) = S / P_{H_2}^{1/2} \quad (3.9)$$

where S is the hydrogen solubility. The concentration gradient responsible for hydrogen diffusion can be defined in terms of the concentration differences (input surface concentration – output surface concentration). The permeation rate, *P*, at which the hydrogen passes through a wall or membrane of the steel of fixed thickness, L, is established by the diffusivity and the concentration gradient as

$$P = D\,(C_1 - C_2) / L \quad (3.10)$$

The values of C_1 and C_2 are known as the interstitial solubilities at the input and output surfaces, when these areas are at equilibrium with their corresponding environments. In terms of Sieverts' law, the permeation equation becomes

$$P = D\,(S_2 - S_1) / L \quad (3.11)$$

3.5 Sources of Hydrogen

Energy is required to dissolve hydrogen in iron because it is an endothermic process. The solubility of hydrogen in steels is low and the reason is that under normal conditions the atomic hydrogen concentration in hydrogen gas is extremely low.

To investigate the influence of hydrogen on the physical properties of iron requires, however, larger quantities that can only be introduced if the surface of iron can be supplied with atomic hydrogen in large quantities. This can be achieved by the cathodic charging of iron with electrolytically produced hydrogen in the nascent state (Pepperhoff and Acet 2001).

From an oil and gas pipeline design standpoint, hydrogen may be made available to metal surface from various sources such as hydrogen-bearing environments during welding, heat-treatment, pickling or service. The most common sources are the cathodic reduction of hydrogen and water, which can be present during cathodic protection or corrosion:

$$2H^+ + 2e^- \Leftrightarrow H_2 \quad (3.12a)$$

$$2H_2O + 2e^- \Leftrightarrow H_2 + 2OH^- \quad (3.12b)$$

Processes involving cathodic polarization, such as cathodic protection and electroplating, accelerate hydrogen formation by the cathodic reduction equations (Jones 1996). The electrons required to make possible these reactions are supplied either by impressed current rectifiers or by sacrificial anodes. Consequently, the principal source of hydrogen considered for this research is the cathodic charging technique using a hydrogen-bearing solution and a power supplier.

On the other hand, when steel comes in contact with aqueous environment, another source of hydrogen takes place, the atomic hydrogen liberation from the iron-water reaction:

$$xFe + yH_2O \Leftrightarrow Fe_xO_y + 2yH^+ + 2ye^- \quad (3.13)$$

In addition, when steel pipeline carries H_2S-containing hydrocarbon fluids two new potential hydrogen sources may be present, the diatomic hydrogen liberation from the iron-H_2S reactions and from the dissociation of hydrogen sulfide (Craig 1993):

$$9Fe + 8H_2S \Leftrightarrow Fe_9S_8 + 8H_2 \quad \text{at } T<90ºC \qquad (3.14a)$$

$$Fe + H_2S \Leftrightarrow FeS + H_2 \quad \text{at } T>90ºC \qquad (3.14b)$$

$$Fe + H_2S \Leftrightarrow FeS_2 + H_2 \qquad (3.14c)$$

$$H_2S \Leftrightarrow S + H_2 \quad \text{(in the presence of } FeS_2) \qquad (3.14d)$$

However, some authors refer the general corrosion reaction $H_2S + Fe \Leftrightarrow FeS + 2H$ to describe the interaction of steel and the H_2S-containing environment. Furthermore, in sour environment in contact with water, the H_2S can dissociate into ions according to (Serna *et al* 2003):

$$H_2S \Leftrightarrow HS^- + H^+ \qquad (3.15a)$$

and

$$H_2S \Leftrightarrow 2H^+ + S^{2-} \qquad (3.15b)$$

A corrosion reaction occurs with the steel forming ferrous ions at anodic sites and a reduction of hydrogen at cathodic sites at the steel surface, according to:

$$Fe \Leftrightarrow Fe^{2+} + 2e^- \quad \text{(anodic site)} \qquad (3.16a)$$

$$HS^- + e^- \Leftrightarrow H^\circ + S^{2-} \quad \text{(cathodic site)} \qquad (3.16b)$$

$$xFe^{2+} + yHS^-_{(aq)} \Leftrightarrow Fe_xS_y + {}_yH^+ \quad \text{(overall reaction)} \qquad (3.16c)$$

High strength pipeline steel grades are susceptible to hydrogen embrittlement (HE) and most of the HE failures have been related to the sulfide stress cracking (SSC) susceptibility. SSC is one of the major failure problems that occur in oil and gas pipeline steel when they are exposed to aqueous H_2S environments.

Another important source of hydrogen can take place when CO_2 (one of three primary corrodents: CO_2, H_2S, and O_2) in oil and gas production dissolves in water and steel corrosion occurs. The reaction that most often predominates is (Craig 2002):

$$Fe + H_2CO_3 \Leftrightarrow FeCO_3 + H_2 \qquad (3.17)$$

Additionally, Craig (2002) shows that when water produced from oil and gas wells is handled at the surface (wellhead equipment and pipelines), it may eventually come into contact with atmospheric air. Many basic forms of corrosion products can appear with dissolved oxygen in the water. However, hydrogen can be made available from two reactions that occur only for the gamma (γ) form of iron oxide (FeO):

$$3\ \gamma\text{-FeO (OH)} + e^- \Leftrightarrow Fe_3O_4 + H_2O + OH^- \quad (3.18a)$$

$$Fe^{2+} + 8\ \gamma\text{-FeO (OH)} + 2e^- \Leftrightarrow 3Fe_3O_4 + H_2O. \quad (3.18b)$$

Once the atomic hydrogen H^+ is on the cathodic steel surface, the electrons provided by cathodic protection equipments assists to produce absorbed hydrogen, which can be either absorbed by the steel or recombined to form molecular hydrogen:

$$H^+_{(aq.\ sol.)} + e^- \Leftrightarrow H_{(absorbed)} \quad (3.19a)$$

$$2H_{(absorbed)} \Leftrightarrow H_2 \quad (3.19b)$$

The degree of absorption of hydrogen and the recombination reactions are significantly affected by the action of surface absorbents called "poisons" and inhibitors. In fact, the hydrogen entry is enhanced by dissolved "poisons" (or cathodic poisons), which are common ions that retard the formation of molecular hydrogen and increase the resident time of nascent hydrogen on the surface. The well known poisons include phosphorous, arsenic, antimony, sulfur, selenium, tellurium, cyanide, and their compounds (Jones 1996). In the presence of sulfide, the hydrogen recombination reaction is retarded so that the hydrogen atoms diffuse into the steel rather than recombining on the steel surface. The inhibitors are usually polar organic compounds that commonly block either the absorption of hydrogen or the anodic reaction by forming chemisorptive bonds on active surface sites (Interrante 1982).

Some studies have revealed that hydrogen damage in iron and steels is significantly more aggressive in environment containing H_2S than in gaseous H_2. The explanation of this phenomenon is based on the velocity of absorption kinetics. Although at low temperature (80ºF ~ 26ºC) and on essentially pure iron surfaces, the difference is fundamentally neglected, alloying elements and impurities enhance hydrogen absorption from H_2S environments on steel surfaces. This is of considerable importance in pipeline steels for oil and gas transport.

3.6 Environmentally Induced Cracking – Hydrogen Damage

Environmentally induced cracking include four forms of corrosion that produce cracking of metallic materials exposure to particular environments. These phenomena are:

- Hydrogen damage (usually also known as hydrogen embrittlement),
- Stress corrosion cracking,
- Liquid-metal embrittlement,
- Solid-metal induced embrittlement.

Generally, these forms of environmentally assisted cracking exhibit some similarities such as their common dependence on yield strength and applied stress. Even though there are various theories that are specific to the behavior of certain materials or environments, none of those mechanisms totally explains all behavior observed either under laboratory or field conditions.

As proposed in this research, hydrogen damage (or hydrogen embrittlement, the afore mentioned improper term used to describe a multitude of failure modes involving hydrogen) will be considered as the most relevant environmentally induced cracking phenomenon. Hydrogen damage phenomenon has been classified as "a form of environmentally induced cracking that generally occurs as a result of the combined action of hydrogen and applied or residual tensile stress, into different types of processes of hydrogen degradation of metals". The subjects described in this chapter are closely related to potential hydrogen damage observed during the experimental tests. Any other classical environmentally induced cracking mechanism can be found in any corrosion text (Jones 1996 and ASM Vol. 13A 2002).

3.6.1 Hydrogen Embrittlement

Hydrogen environment embrittlement occurs during the plastic deformation of the alloy lattice in contact with hydrogen-bearing gases or a corrosive reaction and is therefore strain rate dependent. The degradation of the mechanical properties of the material depends on the strain rate and the hydrogen pressure and purity.

Hydrogen stress cracking (commonly known as hydrogen-induced cracking or static fatigue) is characterized by the brittle fracture of a typically ductile alloy under continued load in the presence of hydrogen. Generally, fracture takes place at sustained loads lower than the yield strength of the alloy. This cracking mechanism, commonly considered a sub-critical crack growth mechanism that often produces time-delayed fractures, depends on the hydrogen fugacity, strength level of the material, heat treatment/microstructure, applied or residual stresses, and temperature.

Hydrogen stress cracking, which promotes one mode of fracture and produces sharp singular cracks, is associated with the absorption of hydrogen and a delayed time to failure (called incubation time) during which hydrogen diffuses into regions of high triaxial stress.

The catastrophic cracking of steels in H_2S environments (a common environment in oil and gas pipeline services), referred to as sulfide stress cracking-SSC, is a special case of hydrogen stress cracking. Zhao *et al.* (2003) points out that sulfide stress cracking is the main failure mechanism of hydrogen embrittlement for high-strength pipeline steels, and that pipeline steels are susceptible to SSC in aqueous H_2S environment with the imposed stress, even if their strength values have been limited to the critical yield strength for sour service (Hardness Rockwell C 22 or 690 MPa). In addition, Jones (1996) defines H_2S as one of the most aggressive of the common industrial aqueous corrosive solutes. The sulfide anion acts as a poison that retards recombination of nascent H-atoms on corroding surfaces, increasing the residence time of nascent H, and enhances hydrogen penetration into the metal lattice.

4.8.2 Blistering

Blistering occurs primarily in low-strength alloys when sufficient hydrogen builds up at crystalline or metallurgical inhomogeneities (traps) and then atomic or nascent hydrogen precipitates as molecular hydrogen (H_2). The pressure developed by molecular hydrogen can achieve sufficiently high values to rupture interatomic bonds, forming microscopic voids and

macroscopic blisters (Jones 1996). Blisters are frequently found in low-strength steels that have been exposed to aggressive corrosive environment (such as H_2S) or cleaned by pickling (ASM 2003).

3.7 Hydrogen Damage Mechanism

This section discusses the common mechanism related to hydrogen damage in metals. Although all of them will not be involved with the experimental results in this research, a general description of these possible mechanisms will lead the reader to a better understanding of the experimental phenomenon.

Although several authors have shown that so-called internal and external hydrogen damage are distinguished by hydrogen being present uniformly or in a gradient from the surface, they are not characterized by an inherently different mechanism (Hirth, 1980). Even though some other mechanisms have been recommended, most are considered variations on these basic theories listed here.

3.7.1 Hydrogen Pressure Theory

The hydrogen pressure theory assumes that embrittlement is caused by the diffusion of atomic hydrogen into the metal and its accumulation in the structure crystalline (dislocations) and metallurgical defects such as micro-voids and second-phase interfaces. A high concentration of hydrogen at these microstructural inhomogeneities causes a large internal pressure that enhances micro-void growth and crack initiation.

Hydrogen charged into steel at high fugacity during aqueous corrosion or cathodic charging may also produce an elevated pressure at these discontinuities. Hydrogen stress cracking failures can be caused by charging hydrogen into the steel either with elevated-pressure hydrogen gas or under intense electrochemical charging. On the other hand, even when the source of hydrogen was at low fugacity, dislocation transport due to cold work, for instance, can also create high internal pressure in micro-voids.

3.7.2 Reduced Surface Energy or Surface Absorption Theory

The reduced surface energy or surface absorption theory states that the absorption of hydrogen adjacent to a crack tip decreases the surface free energy of the metal and reduces the energy needed for fracture, which enhances crack propagation. Although there are some arguments against this theory, it may explain the crack propagation of high-strength steels in a low-pressure hydrogen environment.

3.7.3 De-Cohesion Theory

The de-cohesion theory describes the dissolved hydrogen effect of the bond strength (or cohesive force) between atoms of an alloy matrix. Hydrogen tends to diffuse and accumulate ahead of a crack tip (known as a region of hydrostatic tensile stress). This lowers the cohesive force between metal atoms. This weakening of bond strength makes the normal maximum tensile

stress perpendicular to the crack plane equal to or higher than the lattice bond strength causing fracture.

3.7.4 Enhanced Plastic Flow Theory

The enhanced plastic flow theory is based on fractographic evidence from crack surfaces and has been related to hydrogen-dislocation interactions. This mechanism suggests that hydrogen increases dislocation kinetics and creates new dislocations at surfaces (such as crack tip). In consequence, this hydrogen damage phenomenon is the source for reducing locally the material strength and enhancing localized plasticity. Although softening by hydrogen has been observed in certain steels, hardening by hydrogen has also been found (ASM Vol. 13A 2003).

Troiano (1984) states that a combination of hydrogen and internal stress is required for crack nucleation; for example, the enhanced dislocation motion is not itself a model but is a contributing factor to an overall degradation process. It has also been stated that the major effect of hydrogen is to promote the injection of dislocations at the surface (crack tip). Since hydrogen is a relevant factor to cause crack nucleation, it first has to be transported through the solution (environment) to the metal surface, absorbed, and then transported internally by diffusion mechanism or dislocation kinetics. Finally, it is accumulated at a specific internal location (such as internal interface) where it has an effect on nucleation and growth of a crack.

3.7.5 Hydrogen Attack Theory

Hydrogen attack, a strictly high-temperature mechanism, refers to internal (above 200ºC) decarburization or surface (above 540ºC) decarburization of steels, however the mechanism is predominantly the same for both forms. This behavior is defined as a phenomenon that dependents on temperature, time, and hydrogen partial pressure.

3.7.6 Hydride Formation Theory

Hydride formation is the degradation of transition metals and their alloys in hydrogen atmospheres by a mechanism of formation of brittle metal hydrides phase at the crack tip. When sufficient hydrogen is available in the alloy, a metal hydride precipitates. Cracking of the hydride occurs, followed by crack arrest in the more ductile matrix or continued crack growth between hydrides by ductile rupture. Because hydride formation is enhanced by the application of stress, the stress field ahead of the crack tip may induce precipitation of additional hydrides that cleave (ASM Vol. 13A 2003).

3.7.7 Hydrogen Trapping Theory

Hydrogen trapping is the mechanism that represents one of the principal factors to determine the hydrogen damage susceptibility of iron-base alloys. This mechanism was explained in Section 3.3.

3.8 Hydrogen Damage in Steel

Hydrogen concentration, stress intensity, metallurgical structure of steel, temperature, environment, and solution composition are factors that commonly affect the susceptibility to hydrogen embrittlement of steels in hydrogen-containing atmospheres. As it was extensively described in previous section, the *concentration of hydrogen* in steel is a function of hydrogen-bearing environment pressure, alloy crystal structure, and temperature. Relevant factors that affect the effective hydrogen pressure in the system are the hydrogen gas pressure and pH of the aqueous charging medium in contact with the steel and the environment constituents.

The main effect of *microstructural heterogeneities* in steels on stationary hydrogen diffusion at relatively low temperatures is due to the attractive interactions of dissolved hydrogen with the various types of lattice imperfections. In the case of annealed structures of lamellar pearlite or of tempered martensite the internal stresses are decreased, lattice distortions and defects are widely removed and the concentration of carbon atoms is reduced substantially by carbide precipitation (Riecke *et al* 1980). In general, at the same strength level, normalized or bainitic microstructures are less resistant to hydrogen damage than quenched and tempered fine grain steels in which dislocation density is particularly lower.

Recent research has demonstrated that the most resistant microstructure to hydrogen embrittlement is a highly tempered martensitic structure with equiaxed ferrite grains and spheroidized carbides evenly distributed throughout the matrix (ASM Vol. 13A 2003). Untempered martensite demonstrates poor resistance, specifically to sulfide stress cracking. If the final grain size is greater than prior-austenitic grain size, it produces enhanced resistance; however, it must be larger than the plastic zone size (threshold). It has been found that the carbide/matrix interface is an effective, irreversible trap for hydrogen, capable of dramatically modifying hydrogen transport kinetics. Some studies also demonstrate that carbides precipitate preferentially along grain boundaries and dislocations, and free-precipitate microstructures are virtually embrittled (Stevens *et al*. 1980).

Non-metallic inclusions and alloying elements have a profound effect on the hydrogen diffusion, and subsequently on the resistance of steels to hydrogen embrittlement. The hydrogen diffusion coefficient for steel containing elongated sulphide inclusions is higher in the longitudinal direction than in the transversal one. When inclusions are not continuous the coefficient in the longitudinal direction is considerably reduced. Generally, control of common non-metallic impurities (“clean steels”) improves the resistant of steels to hydrogen damage. Evidently, the beneficial nature of such traps is a strong function of (a) their number and total surface area, (b) their interaction energy with hydrogen, and (c) the hydrogen concentration that must be trapped.

Because a particular alloying element may improve the hydrogen embrittlement resistance or may increase susceptibility to cracking, it is difficult to explain the effect of alloying of elements and their concentration in steel. For example, molybdenum (Mo) is beneficial in increasing the resistance of AISI 4130 steels to sulphide stress cracking. Elements such as carbon (C), phosphor (P), sulphur (S), manganese (Mn), and chromium (Cr) impart greater susceptibility to hydrogen embrittlement in low-carbon steels. On the other hand, increasing chromium, nickel

(Ni), and molybdenum content, the permeability and diffusivity of hydrogen decrease, and consequently the susceptibility to hydrogen embrittlement is higher (Elboujdaini *et al.* 2003). To summarize, microstructure control has been established to be a significant requirement for limiting the susceptibility of steels to hydrogen embrittlement.

The susceptibility of steels to hydrogen embrittlement is generally increased as their strength increase. The *yield strength level* of steel can considerably modify the hydrogen embrittlement susceptibility. Some studies demonstrate that threshold stress intensity for cracking or crack growth of steels (such as AISI 4340 steel in aqueous and gas hydrogen) increases with increasing yield strength. Therefore, very high-strength steels (>100 ksi ~ 700 MPa) should not be used in hydrogen environments due to their threshold stress intensities, which are significantly less than those thresholds under benign conditions. Ultrahigh-strength steels (>200 ksi ~ 1400 MPa) are extremely susceptible to hydrogen embrittlement, even though when they are exposed to chlorides-containing solution (principal cause of stress corrosion cracking). However, some steel makers have developed new high-strength material that can be cautiously used in hydrogen-bearing environments.

Threshold stress intensity for cracking or crack growth, below which, for all practical purposes, hydrogen embrittlement cracking does not occur, is also known as stress-intensity value. It is an experimentally determined quantity value that depends on (ASM Vol. 11 2002):

- Nominal strength of the unembrittled component,
- Amount of hydrogen present in the steel,
- Location of the hydrogen in the microstructure,
- Presence of other embrittling elements or microstructural phases.

Hydrogen embrittlement occurs mainly in high-strength steels commonly utilized in oil and gas industry; however, it has been observed in low-strength steels, too. It occurs principally by the loss of tensile ductility or blistering, because hydrogen promotes decohesion of the matrix at inclusion interfaces and carbide particles encourage the formation and/or growth of voids. Cracking has been also detected in low-strength (low hardness) steels under H_2S-containing environments in the absence of stress.

High-strength (high hardness) steels commonly show an incubation time before fracture initiates under sustained loading. Commonly, this phenomenon occurs in combination with sites of high-stress triaxiality. Fracture initiates internally in the steel, usually at notch roots or under plain strain where triaxial stresses are created. Tensile residual stresses may also promote the initiation of hydrogen stress cracking.

Hydrogen embrittlement is most prevalent near ambient temperature (T_{room}), and its tendency decreases with increasing or decreasing temperature. This phenomenon becomes less severe or virtually disappears in steels at higher or lower temperature. Above T_{room}, diffusivity of hydrogen is improved and trapping is diminished, while below T_{room} hydrogen motion is very slow to fill enough traps.

3.9 Hydrogen Damage in Pipelines

Over half the world's oil and gas reserves are located in environments removed from potential users and require large pipelines to transport the hydrocarbons to market. During the last thirty years, pipeline design has advanced due to demands for thicker, larger diameter, and stronger pipes. There are also additional demands on strict dimensional control and accuracy both in diameter and wall thickness.

Pipelines carrying wet sour hydrocarbons can develop hydrogen embrittlement of the pipe steel. In the absence of stress, pipeline steels exposed to sour fluids experience longitudinal cracks through the pipe wall, and the tip of one crack may converge with another in 'stepwise' pattern (stepwise cracking). The most common form of atomic hydrogen available at the internal surface of pipeline is usually from the oxygen-accelerated dissociation of H_2S gas molecule in the presence of water. The fugacity of hydrogen generated during sulfide corrosion is extremely high.

In general, hydrogen-induced cracking mechanism of high-strength pipeline steels in contact with a wet H_2S-containing environment can be explained by the corrosion reaction

$$H_2S + Fe \Leftrightarrow FeS + 2H \qquad (3.20)$$

under a combined action of corrosion and tensile stress. This chemical reaction produces FeS that represents a permeated layer by atomic hydrogen diffusing to favorable sites where molecular hydrogen is formed. Zhao *et al.* (2003) states that a continuous FeS adherent scale produced on the surface of the steel will protect the metal against further attack. However, under the imposed aqueous H_2S environments, the FeS scale does not avoid hydrogen penetration into the plastic region of the crack tip, because the adherent strength between the FeS scale and the matrix is weak and the FeS scale is apt to fall off. Also, there are numerous microcracks and corrosion grooves distributed on the surface of corrosion scales and crystal granules of FeS. Moreover, FeS acts as a cathode to form an active battery with the matrix. All these situations assist in promoting both the above corrosion reaction and the hydrogen penetration that follows.

Hydrogen-induced degradation in pipeline steels generally takes a form of hydrogen-induced blister cracking (HIBC), which is induced by hydrogen trapped at interfaces between matrix and, typically, hot roll-flattened manganese sulfide inclusions. An externally applied stress influences considerably the manner of HIBC extension; in the absence of external stress HIBC develops by 'stepwise' linking of internal blisters along with considerable plastic deformation. Under externally applied stress, the HIBC develops by linking blisters formed perpendicular to the applied stress (Oriani *et al*. 1985).

Elongated sulfide inclusions, such as type II MnS, and glassy silicates are particularly favorable sites for the formation of molecular hydrogen in the steel. Lower volume fractions of inclusions correspond to higher resistance to hydrogen damage. The hydrogen trapped principally at elongated MnS inclusions are responsible for hydrogen-induced cracking due to either internal pressure or decohesion of the inclusion-matrix interface. However, ellipsoidal sulfide inclusions, such as type I MnS, have better hydrogen-induced cracking resistance.

Atomic hydrogen is also available from other sources such as cathodic protection and aqueous environments.

A flat inclusion-matrix interface will accelerate stress-induced hydrogen diffusion into the crack tip region, when it is separated and pressurized with hydrogen gas to form a crack. Around a global or ellipsoidal inclusion, on the other hand, no stress-induced diffusion takes place because of the lack of triaxial stress concentration. In consequence, inclusion shape control is essential for improvement to the hydrogen damage resistance of pipeline steels (Oriani *et al.* 1985).

Non-metallic inclusions act as hydrogen traps and offer low resistance to hydrogen embrittlement. Once hydrogen is trapped at an inclusion, it may achieve a high internal pressure, reducing as well the interatomic cohesive forces and surface energy at the inclusion surface ($\sigma^H_C < \sigma^o_C$). This phenomenon significantly affects the dislocation motion in the plastic zone. This theory is schematically illustrated in Figure 3.4.

A crack will be initiated or assisted when the sum of all applied (σ^H_a) and residual (σ^H_r) stresses is greater than the cohesive strength (σ^H_C). The amount of hydrogen trapped in the inclusion and the specific quantity of hydrogen trapped at which a crack will be induced by hydrogen depend on various inclusion parameters: shape, size, distribution, density, neighboring structure and impurities (which reduce inclusion-matrix interface cohesion strength).

As it was previously reported, pipeline steel microstructure also plays an important role in hydrogen embrittlement resistance. Elboujdaini *et al.* (2003) reports that heavily banded microstructures could enhance hydrogen-induced cracking by providing low fracture resistance paths for cracks to propagate more easily. However, Serna *et al.* (2003) states that banded structure presented by microalloyed steels may contribute to increase in hydrogen damage resistance at atmospheric conditions.

In ferritic pipeline steels, bainite and un-tempered martensite are the most susceptible microstructures whereas quenched-tempered and normalized are the most resistant to hydrogen embrittlement. In other words, many studies have demonstrated that the microstructure after normalizing, i.e. fine ferrite-pearlite structure, and after quench and temper treatment, i.e. tempered martensite, of different pipeline steel grades (up to X62) reduces hydrogen-induced cracking susceptibility.

However, Zhao *et al.* (2003), studied three common pipeline steel microstructures, and defined the acicular ferrite-dominated structure as the optimum candidate microstructure for pipeline steels in hydrogen-gearing environments (in particular, oil and gas sour service), while ultra fine ferrite microstructure is next. The acicular ferrite microstructure is also known as Widmanstätten ferrite or bainitic ferrite (Gräf *et al.* 2002). The ferrite-pearlite microstructure has the worst hydrogen embrittlement (sulfide stress cracking) resistance carbides and MnS inclusions precipitate along the banded pearlite where hydrogen diffuses to their interfaces reaching the critical hydrogen concentration quickly.

3.10 Hydrogen Embrittlement of Cathodically Protected Steels

Hydrogen diffusion into iron and steel is strongly affected by various electrochemical and environmental factors; typically, it increases with cathodic polarization. Steel pipelines are commonly cathodically protected either with sacrificial anodes or impressed current. Although the cathodic protection of such tubulars usually does not cause hydrogen embrittlement, high-strength steel can be embrittled by cathodic protection. Nevertheless, experiments using relative low-strength pipeline steel demonstrate that at considerably large (more negative) cathodic current density (overprotection), steel ductility can be reduced. Since excessive cathodic protection would result in undesirable hydrogen evolution, the lack of steel ductility is considered to be the result of hydrogen degradation due to cathodically evolved hydrogen at crack tips and pipe surfaces. If pipeline is additionally protected with external coating, overprotection currents generate electrochemically hydrogen atoms on coating defects such as "holidays." Thus, the pipeline material can absorb those atoms enhancing hydrogen-induced cracking.

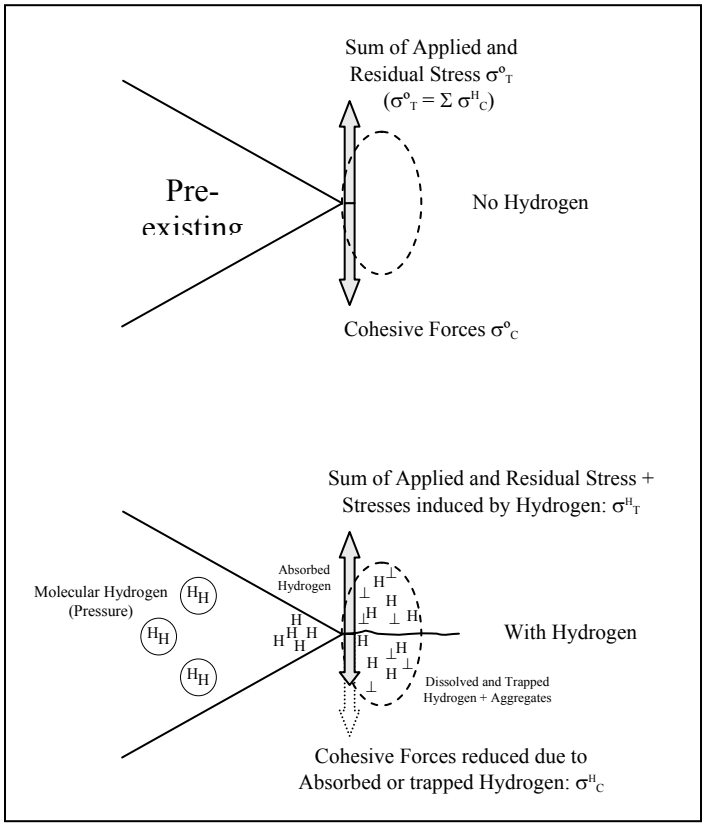

Figure 3.4. Effects of hydrogen on preexisting defects (Oriani et al. 1985).

Sometime a rectifier is used to supply impressed current for cathodic polarization of the pipeline steel. Since this mechanism of protection depends on external current polarizing cathodic elements of local half-cells to the open-circuit potential of the anodes, at a specific time, the cathode and anode potentials on the pipeline surface become equal and corrosion currents no longer flow. Consequently there is no tendency for metal ions to enter into solution (Das *et al.*

1977). However, in the extreme case of overprotection copious evolution of hydrogen atoms occurs at the pipe surface by the reduction of dissolved oxygen. The amount of evolved hydrogen generated by overprotection increases as a function of applied polarization potential and time and could be partially absorbed by the steel leading to catastrophic failures as a result of hydrogen embrittlement. The concentration of hydrogen at the pipe surface is also dependent on hydrogen entry and diffusion, and the surface features such as surface irregularities, oxides, and scales. Moreover, the hydrogen gradient in the metal matrix depends on the loading time, the diffusion rate, and the possibility for the hydrogen to escape (Olsen *et al.* 2001).

Considering high-strength steel pipelines in aqueous environment, cathodic polarization, which promotes the evolution of hydrogen at the steel surface, causes an increase in crack growth rate while anodic polarization, which stimulates corrosion, decreases the crack growth rate at low pH values but increases it at high pH values (Oriani *et al.* 1985). An increase in hydrogen uptake ("hydrogen entry" or "hydrogen diffusion") and in hydrogen embrittlement at low anodic polarization was observed for high-strength low-alloy steels in NaCl solutions and low-carbon steels in carbonate/bicarbonate solutions. High hydrogen uptake may occur within occluded cells, such as cracks, pits, and crevices, when the external surface of the steel is anodically polarized. At anodic potentials, hydrogen evolution in the occluded cells results from a shift of a potential in the negative direction due to the ohmic potential drop, so that the thermodynamic conditions for the hydrogen evolution are attained (Flis and Zakroczymski 1992).

Some researches point out that hydrogen-induced cracking in pipelines under cathodic protection can be defined as a function of surface mechanical conditions (such as defect size) and the characteristics of the cathodic current. To prevent initiation of hydrogen-induced cracking at surface defects in pipeline under cathodic protection, inspection of casting and surface defects, evaluation of applied stresses, current and the critical crack-tip opening displacement with cathodic protection are the methods that may be adopted (Hagiwara and Meyer 2000).

3.10.1 Cathodic Protection as Hydrogen Embrittlement Test

This discussion includes experimental results from updated researches focused on the effect of cathodic polarization of the high-strength pipeline steels on hydrogen embrittlement (HE) tests. A better understanding of these results is possible if the open-circuit potential concept is clarified.

As soon as the potential becomes more electronegative with respect to Open-circuit-potential, steel is at a cathodic potential. The discharge of atomic hydrogen (H^+), called reduction or forward reaction, is produced at cathodic potentials. HE tests use cathodic potentials to produce hydrogen at the surface and to put it into the steel in order to determine its effect in combination with stresses (applied or residual).

As some authors establish that any cracking study of high-strength steels at potentials more electronegative than the open-circuit potential is considered as a HE, consequently, cathodic protection of pipeline steels becomes an industrial-scale-size HE test. The reason is because any

cathodic protection method is continuously producing hydrogen at the surface of the pipeline steel. HE susceptibility increases because more hydrogen may be located into the steel.

Because HE tests combine hydrogen damage with stresses, the most severe HE test under cathodic protection is generated when hydrogen is produced near stressed pipeline section. As a result, any plastically deformed pipe segment may be the best coupon that counts for this severe test.

3.11 Hydrogen Effect on Magnetic Properties of Steel

The behavior of hydrogen in ferromagnetic materials has been studied by a very sensitive method called *magnetic aftereffect*. When a magnetic field near a hydrogen-charged ferromagnetic material is abruptly changed, a redistribution of hydrogen atoms occurs. Those atoms diffuse to energetically to more favorable sites inside the magnetic domain walls. This phenomenon gives rise to relaxation of the magnetic reluctance. The characteristic time for this *aftereffect* is related to the diffusion coefficient of hydrogen.

An interstitial alloy is an alloy formed when some of the interstices or holes in the densely packed host metal structure (tetrahedral or octahedral spaces between the atoms) are occupied by small atoms of non-metallic elements such as hydrogen, carbon, nitrogen (N), and boron (B). When interstitial atoms are located in tetrahedral positions they are surrounded by four atoms, and when they are located in octahedral positions by six atoms.

The number of interstitial atoms that are actually accommodated in the structure is much less than the available interstitial sites. Introducing a metalloid atom into an interstitial position leads to lattice distortions, since the atom requires more place than is offered by the interstitial void. A chemical binding phenomenon also takes place between the metal and the metalloid atoms. It is caused by the distribution of the electrons of the metalloid atoms to the 3d-band of the host metal. In general, the hydrogen concentration in many transition metal alloys depends on the magnetic properties of the metal because of the number of outer electrons per constituent atom.

The electrons on the interstitial hydrogen atoms are contributed to the d-band of iron and its alloys. The increase in the valence electron concentration and the lattice expansion causes change in the magnetic properties. These alterations appear to be almost equivalent to the change that would occur if the electron concentration of the metal were changed by substitutional alloying. The alloys with higher electron concentrations are strong ferromagnets, while those with lower electron concentrations are alloys with strong volume dependent magnetic properties (Pepperhoff and Acet 2001). Each alloy has its own ability to have its hydrogen solubility altered by a magnetic field.

Hydrogen donates its electron to the d-band and influences the banding conditions. Since hydrogen strongly influences the physical properties of 3d-metals, the concentration dependence of the magnetic properties of the metal-hydrogen system can be based on a simple band model, and with it, predictions can be made on the properties of the less investigated metal-hydrogen system (Pepperhoff and Acet 2001).

4. THEORETICAL BASICS – THERMODYNAMIC MODEL

In the attempt to assess the effect of magnetization on the hydrogen damage in pipeline steels, a mathematical relationship was developed from thermodynamic basics. From a thermodynamic analysis of an electrochemical cell, the examination and quantification of the driving forces for potential electrochemical reactions may be determined. The cathodic reaction of hydrogen $2H^+ + 2e^- \rightarrow 2H$, the most common electrochemical reaction that makes hydrogen to be available to pipeline steel surface in service, is analyzed in terms of thermodynamics. An additional component, external work due to magnetization of the system, is included into the thermodynamic analysis of the system.

The absorbed hydrogen concentration in pipeline steels, [H], is the amount of total hydrogen atoms that are taken up by the material and distributed throughout its bulk. Hydrogen sources are numerous; however, from the pipeline service standpoint, hydrogen is available to metal surface from hydrogen-bearing environments that surround the pipes and the cathodic protection system. On the other hand, the magnetic flux density, B, is the amount of magnetism induced into a body by a magnetizing force. In terms of pipeline inspection techniques, the magnetic system of MFL tools produces the magnetizing force, which is induced into pipe steel. Thus, [H] can be related to B by a mathematical equation obtained from a thermodynamic and electrochemical analysis. These terms are based on the hydrogen dissociation chemical reaction and the work experienced by the steel under the magnetic flux density induced by MFL tools.

Since hydrogen atoms donate their electrons to the d-band of transition metal, these bestowed electrons modify electron spin configuration and, consequently, the material behavior under a magnetic field. This phenomenon varies the entropy of the system resulting in a variation of the external work. A thermodynamic expression of equilibrium is utilized to derive the relationship between the magnetic field strength and the activity of hydrogen. At constant pressure and temperature, the auxiliary function

$$dG = -external\ work. \tag{4.1}$$

Modifying the derivation from the Nernst's equation by adding the second external work term ($-\Delta M\ B$) to the electrochemical potential term ($-n_eFE$), the differential Gibb's free energy, dG, is given by:

$$dG = -\Delta MB - n_eFE \tag{4.2}$$

where ΔM is the change in magnetization, B is the magnetic flux density, n_e is the number the electrons exchanged in the electrochemical reaction, F is Faraday's constant, and E is the electrochemical potential. Considering the region of hydrogen solubility where the appropriate reaction, in terms of electrochemistry, is given as:

$$M + H^+ + e^- \rightarrow M\text{–}H(s) \tag{4.3}$$

where H(s) is a hydrogen atom in solid solution in the solid metal matrix, M. The half-cell electrochemical potential, E, in Equation (4.2) belongs to reaction (4.3). Therefore, Equation (4.2) becomes:

$$dG = -\Delta M\, B - n_e F\,[E^o - \frac{RT}{n_e F}\ln\left(\frac{[H]}{[M][H^+]}\right)] \tag{4.4}$$

where E^0 is the standard half-cell electrode potential for Reaction (4.3) and is dependent on the composition of the metal, M, used. Note that [H] is used for simplicity to represent the concentration of hydrogen in the metal, which is shown as M-H(s) in Reaction (4.3). For a given alloy composition, the activity of the metal, M, may be taken as unity. At equilibrium, $dG = 0$, and for a given metal composition, the hydrogen concentration as a function of the change in magnetization is given by:

$$\ln[H] + 2.303\ pH\ - \frac{n_e\, FE^{\,0}}{RT} = \left(\frac{\Delta M}{RT}\right)B \tag{4.5}$$

Rearranging Equation (4.5), the hydrogen content under a magnetic flux density is determined by:

$$[H]_{B=B} = [H]_{B=0} * e\left(\frac{\Delta M}{RT}\right)B \tag{4.6}$$

where the equilibrium hydrogen content $[H]_{B=B}$ (equilibrium point) is determined under a magnetic flux density (B), and $[H]_{B=0}$ is the hydrogen solubility (equilibrium point) under no applied magnetic field and is given by

$$[H]_{B=0} = e\left(\frac{n_e FE^0}{RT} - 2.303pH\right) \tag{4.7}$$

at constant pH, temperature and for fixed alloy composition, $[H]_{B=0,}$ is a constant. Equation (4.6) shows how the absorbed hydrogen concentration increases with magnetic flux experience. This expression indicates that the hydrogen solubility will increase exponentially with increasing magnetic flux.

Rearranging Equation (4.5), in terms of the natural logarithm, the graphical expression is developed, shown in Figure 1, where the slope of the straight line (ΔM/RT) is a material property.

$$Ln\left[H\right]_{B=B} = Ln\left[H\right]_{B=0} + \left(\frac{\Delta M}{RT}\right)B \tag{4.8}$$

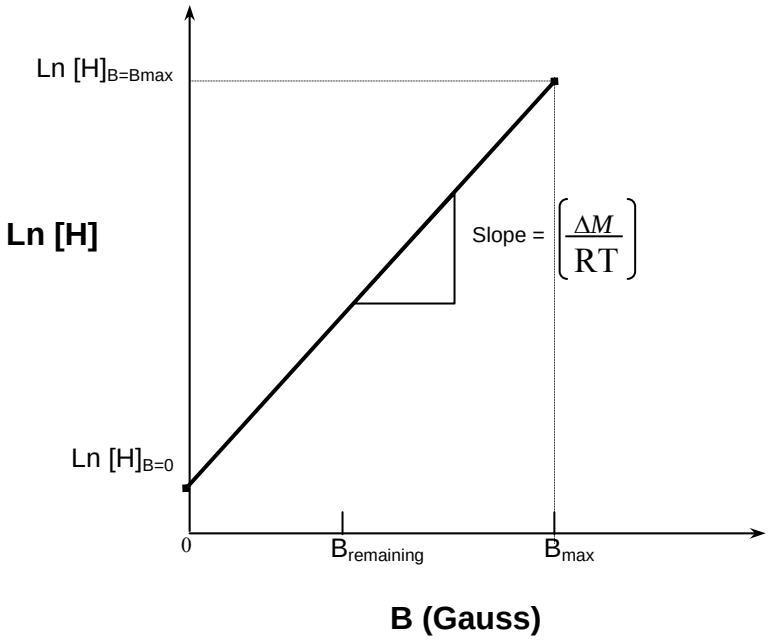

Figure 4.1. Schematic representation of Equation (4.8).

5. EXPERIMENTAL PLAN

The objective of this study is to assess the effect of a high-strength magnetic field generated during pigging operations on the hydrogen-induced cracking (HIC) susceptibility of pipelines steels. To achieve this purpose, and considering the sources of hydrogen and the mechanical integrity of the pipe within pipeline service life, two main groups of experimental variables have been defined.

The effect of magnetization on absorbed hydrogen concentration and hydrogen induced cracking in pipeline steels is evaluated in this chapter. The studied pipeline steels were characterized from mechanical properties tests, microstructure analysis, and chemical composition tests. The magnetic force required to saturate the tested steels was determined from a magnetic property hysteresis test.

5.1 Experimental Variables

The two groups of variables are closely related to the magnetization effect on hydrogen concentration in pipeline steels, the magnetization effect on hydrogen concentration in coldworked steel samples, and the magnetization effect on hydrogen induced cracking for thick high strength pipeline steels. The independent variables are (a) pipeline steel grade, (b) wall thickness, (c) magnetic flux density, (d) residual stress, and (e) hydrogen charging time (hydrogen availability), while the dependent variable is the absorbed hydrogen concentration. The hydrogen concentration will be influenced by the manipulation of the independent variables in this experimental study.

The pipeline steels commonly used in the oil and gas industry are covered by the American Petroleum Institute's (API) technical standards. The forty-third edition of the API Specification 5L, Specification for Line Pipe, classify the line pipe steels in standard grades. The steel grades covered by this specification run from the standard Grade A25 to Grade X80. Today, most of the pipeline networks are designed conventionally to protect against thermal effect, ice mechanics (arctic service), high pressure, and environmental concerns. These requirements are satisfied by using thicker walls and higher steel grades. The selected steel grades to evaluate the magnetic effect on HIC susceptibility in pipeline steels in this research are Grades X52, X70, and X80, which are considered for purposes of this study as high-strength steels because they have yield strength levels above 70 ksi (482.6 MPa).

Because thicker line pipes are used to achieve today's design requirements, different wall thickness pipes were obtained from various sources to be evaluated. The steel pipes of Grades X52 and X70 were obtained from a local energy company (Xcel Energy, Inc) and the Grade X80 from the National Institute of Standards and Technology (NIST) Laboratories in Boulder, Colorado. The wall thickness range run from $^{5}/_{16}$ to ¾ inch (7.94 to 19.0 mm); i.e. the steel pipes of Grades X52, X70, and X80 have a wall thickness of $^{3}/_{8}$ (9.53 mm), $^{5}/_{16}$ (7.94 mm), and ¾ inch (19.0 mm), respectively.

The Magnetic Flux Leakage (MFL) tools use strong permanent magnets to create a uniform, consistent magnetic flux density in the pipeline steel up to the magnetic saturation. As soon as the MFL tool passes by a certain point within the pipeline, the magnetic field is discontinued and a remanent magnetic flux density is left behind. The magnetic flux density values to be evaluated in this study are zero (no magnetic field applied) and the magnetic saturation value. The effect of the remanent density is also analyzed in Chapter 7 using a mathematical and graphical technique. It is important to note that the magnetic saturation of pipeline steels depends upon the material strength and the wall thickness of the pipe. The number and power of the permanent magnets positioned in the MFL tool define the applied magnetic flux density.

Pipeline integrity is usually affected by well-known damages called dents. Pipes with this type of mechanical damages (local indentation with an external gouge that results in reduction of pipe structural integrity) are also inspected using MFL tools. Updated research uses geometric models (shapes of dents) to model the probability of detection for dents using high-resolution inline inspection tools. A sharp dent with an opening angle is the model selected for this study because it represents the worst realistic scenario. With an opening angle (bending angle) range of 120º to 60º, residual stresses are induced into the steel, making possible to achieve the effect of magnetization on hydrogen concentration in coldworked steel samples.

Even though several electrochemical techniques were selected initially (early stages of this research project) to assess the magnetization effect on HIC in pipeline steels, the cathodic hydrogen charging was finally considered as the most suitable and relevant method. In consequence, cathodic hydrogen charging time ranging from 1 to 6 hours became the last experimental variable included in this study.

5.2 Assessment of the Magnetization Effect on HIC in Pipeline Steels

The design criteria based on current operational conditions and confidence assessments of the present and future condition of a pipeline (pipeline integrity management) lead the oil and gas industry to use high strength steels, thicker pipe wall, cathodic protection techniques, and high frequency of usage of MFL tools. These requirements suggest that the exclusivity of most of today's applications include the use of thicker, higher strength, cathodically protected steel pipes and more frequent inspection techniques using larger magnetization strengths. Consequently, these operational characteristics ask some pertinent questions: do increased magnetism and high frequency of usage of MFL tools lead to hydrogen effects with cathodically protected steel pipelines? Does this effect lead to more severe hydrogen damage? If there is a potential of enhanced hydrogen cracking due to inline inspection tools, what are the possible precautionary actions? An experimental plan was defined to answer the first two questions, but the last one, because of the significant impact in the industry, requires a broad discussion with pipeline industry.

To set up an experimental plan for the assessment of the magnetization effect on HIC in pipeline steels, several references were consulted. Even though the preliminary plan included electrochemical techniques based on rate of permeability and solubility of hydrogen in pipeline

steels, a direct hydrogen concentration method was finally selected. Because the magnetization effect must also be included in the experimental plan, minor modifications of the selected technique are needed.

The hydrogen concentration in a material has been experimentally measured using the electrochemical techniques called the Devanathan cell and the Barnacle Electrode cell. The first cell was developed by Devanathan and Stachurski (Devanathan and Stachurski 1962) for the accurate measurement of the instantaneous rate of permeation of electrolytic hydrogen through a metal membrane; while the second, a modification of the Devanathan cell, measures the hydrogen activity (diffusion) correlating hydrogen concentrations with delay failure in high-strength steels. The Devanathan cell, a extremely sensitive electrochemical method, requires that a diffusion gradient exist within the metal membrane or foil by producing hydrogen on one side, such as by cathodic charging, and removing it on the other side by anodic polarization with a very sensitive potentiostat. On the other hand, the *barnacle electrode* employs only the extraction part of the *Devanathan cell*, assuming that hydrogen is previously homogeneously distributed all through the sample (initial hydrogen concentration). The Barnacle Electrode method replaces the potentiostat of *Devanathan cell* by a nickel/nickel oxide electrode to act as a stable and non-polarizing electrode (cathode) that keeps zero hydrogen concentration at the extraction-side-surface of steel (anode) by oxidizing the exiting hydrogen atoms to water. This technique is commonly used to measure both the hydrogen concentration and transport simulating pipeline service conditions.

The first stage of this research was based on the construction and setup procedures of the Devanathan cell and the Barnacle Electrode. Test procedures were based on ASTM G148 (Standard Practice for Evaluation of Hydrogen Uptake, Permeation, and Transport in Metals by an Electrochemical Technique) and ASTM F-1113 (Standard Test Method for Electrochemical Measurement of Diffusible Hydrogen in Steels - Barnacle Electrode). Several experiments were run using Devanathan cell, where a potentiostatic/galvanostatic unit (EG&G PARC model 273A) was used. The initial data obtained was not used in the study due to inconsistencies in the galvanostatic unit.

A direct hydrogen concentration determination technique is able to perform an elemental analysis. A hydrogen determinator, such as LECO-Hydrogen Determinator RH-40, requires that a material sample is previously charged using either operational conditions (same concept for the Barnacle Electrode) or any single electrochemical or high temperature diffusion method. Because the steel samples are obtained from uninstalled line pipes, the cathodic hydrogen pre-charging was conducted in a 'cathodic charging cell', in which the material sample is the cathode and a platinum wire is the anode. This method produces hydrogen from the electrolyte (acid solutions) at the sample surface, inducing hydrogen to be absorbed by the material.

To determine the nature and size of the magnetic effect on the hydrogen activity in pipeline steel, a minor modification of the electrochemical technique was required. Initially, it was planned that a magnetic field would be applied using a DC-magnetic coil around a iron-base nail that is placed close to the specimen to simulate the whole effect of the magnetic flux leakage tool, i.e. the peak magnetization during and remaining magnetization after pigging. However, the strong and continuous magnetic field needed to simulate pigging operations could not be

achieved in this way. In consequence, permanent magnets were obtained to accomplish the magnetic saturation value for the high-strength steel to be evaluated.

With the purpose of assessing the magnetization effect on HIC in pipeline steels, several sets of comparative experiments were designed. The first set compares the hydrogen concentration in the selected, as-received steels with and without an applied magnetic field after several periods of charging time. The second set compares hydrogen concentration in coldworked-steel samples with and without an applied magnetic field after three hours of charging. The last set of experiments compares the hydrogen damage after charging for vary periods of time. The hydrogen damage test do not follow any standard corrosion test in terms of solution concentration and time (Table 5.1); however, this hybrid, comparative test makes available results of how a strong magnetic field affects the hydrogen damage phenomenon in high-strength pipeline steels under laboratory conditions.

Table 5.1. Comparison between NACE standard methods and the hybrid method

Test Method	Description	Evaluation
NACE TM 0284	"Evaluation of Pipeline and Pressure Vessel Steels for Resistance to Hydrogen-Induced Cracking"	Resistance of unstressed pipeline steels to stepwise cracking induced by absorbed hydrogen.
NACE TM 0177	"Laboratory Testing of Metals for Resistance to Sulfide Stress Cracking and Stress Corrosion Cracking in H_2S Environments"	Resistance of metals subjected to tensile stresses to cracking failure in environments containing H_2S
Hybrid	----	Resistance of high-strength pipeline steels under bending stresses to strong magnetic field effect on hydrogen damage by absorbed hydrogen.

5.3 Characterization of Pipeline Steel Samples

Because the steel pipe samples of Grades X52 and X70, from a local energy company, were unidentified, a set of standardized tests was run to determine their mechanical properties and chemical compositions. The steel pipe sample Grade X80, from a local standards laboratory, was clearly identified. A micro-hardness test, microstructure analysis, and atomic absorption spectrometry analysis were conducted to verify the mechanical properties and chemical composition. The tests are performed according to API Spec5L testing procedure, which refers to the requirements of ASTM A370. Microstructural analysis was required to complete the characterization of the as-received material.

5.3.1 Tensile Test and Micro-Hardness Test

Four standard size tensile test specimens from large-diameter tubular products were cut from both steel pipes of Grades X52 and X70; two specimens from each steel grade. The tensile

tests were accomplished according to the API Spec 5L requirements using the material test system MST Alliance RT/100 (see Figure 5.1). The nominal load capacity of the system is 100 kN (22,500 lbs). Table 5.2 shows the mechanical properties of the steel tested (see Figure 5.2) in this study, and the properties of the specified steel as per API Spec. 5L requirements.

Microhardness testing is an indentation method for measuring the hardness of a material on a microscopic scale. The microhardness, refers to static indentations made with the Vickers diamond pyramid indenter, and is measured in HV (Hardness Vickers) units. The hardness can be converted into tensile strength or ultimate tensile strength units (psi) and other hardness scales (e.g. Rockwell). Conversion tables are available for steels and other alloys.

A microhardness test was run for the pipeline steel of Grade X80 sample. The average value in terms of hardness scales and tensile strength is reported in Table 5.3.

Figure 5.1. Load Measurement System - Tensile Test Machine (Alliance Model RT/100)

5.3.2 Chemical Composition and Microstructure

The steel samples used for the laboratory tests were low-carbon steel, produced according to API 5L Grade X52, X70, and X80 specifications. Table 5.4 shows the chemical composition of the steel tested in this study, and for the steel matching the API Spec. 5L requirements.

The microstructures of all the samples were examined using standard optical microscopy, where typical photomicrograghs are shown in Figures 5.3 and 5.4. The microstructures revealed

typical characteristics for these low-carbon high-strength pipeline steels. The X52 pipeline steel sample exhibited a mixed ferrite structure with small concentration of carbides at grain boundary next the coarse grains, few grains of pearlite, and greater fine ferrite grain concentration. The grain size ranges from 4 to 20 μm (see Figure 5.3 a-b).

The X70 pipeline steel sample also displayed a mixed ferrite structure with small concentration of carbides at grain boundary besides the coarse grains and few grains of pearlite, where the grain size ranges from 3 to 12 μm (see Figure 5.3 c-d). The elongated nature of the grains reflecting the rolling direction and texturing are evident in these micrographs.

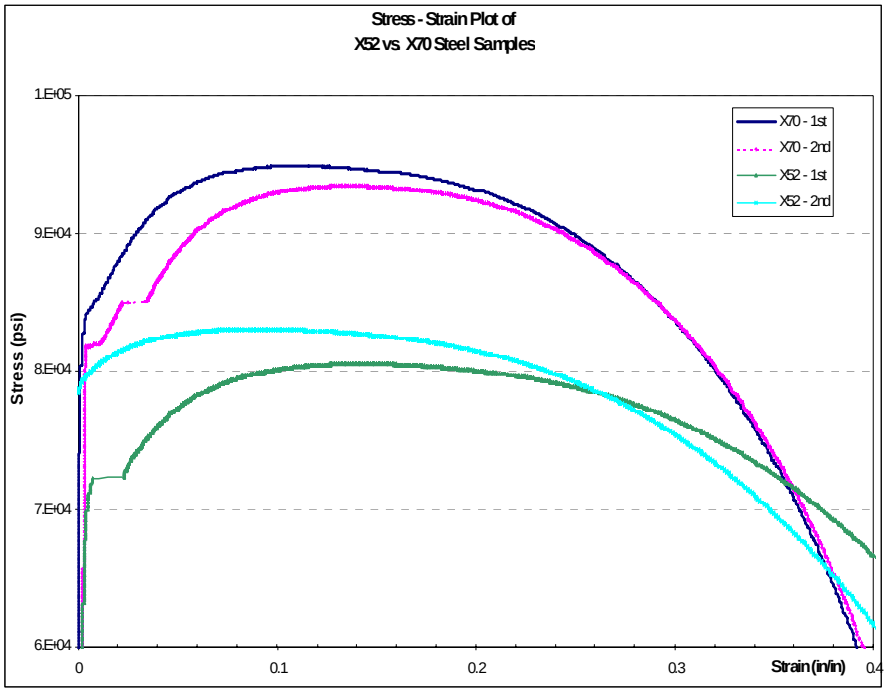

Figure 5.2. Tensile test diagram of tested steel of Grades X52 and X70.

Table 5.2. Mechanical properties of tested steel of Grades X52 and X70.

Sample	**API Spec. 5L Requirements**		**Tensile Test**	
	Yield Strength Minimum psi (MPa)	UTS Minimum psi (MPa)	Yield Strength psi (MPa)	UTS psi (MPa)
X52 – a	52,000 (358.5)	66,000 (455.0)	78,998 (544.7)	80,523 (555.2)
X52 – b			72,227 (498.0)	83,020 (572.4)
X70 – a	70,000 (482.6)	82,000 (565.4)	81,892 (564.6)	94,893 (654.3)
X70 – b			83,346	93,429

Table 5.3. Mechanical properties of tested steel of Grade X80.

Steel Sample	Mechanical Properties			API Spec.5L
	HV	HR_B	Tensile Strength (psi)	UTS Minimum (psi)
Grade X80	207	94	100,000	90,000

The micrograph of the pipeline microalloyed steel sample of Grade X80 exhibited an acicular ferrite structure with sub-grain formation and grain sizes ranging from 4 to 20 μm (see Figure 5.4). The X80 pipeline steel sample showed no difference between microstructure of a longitudinal section and a transversal section. The whole set of microstructures are typical of API pipeline low-carbon heat-treated steels.

Table 5.4. Chemical composition of tested steels (weight percent).

Material	***Carbon (%)***	***Manganese (%)***	***Phosphorus (%)***	***Sulfur (%)***	***Titanium (%)***
X52 Tested Steel	0.061	1.31	0.005	0.0069	--
	0.0609	1.30	0.004	0.0069	--
	0.0606	1.31	0.005	0.0073	--
X70 Tested Steel	0.074	1.41	0.012	0.0029	--
	0.0655	1.41	0.005	0.0033	--
	0.0718	1.42	0.012	0.0031	--
X80 Tested Steel	0.06975	1.34	0.004	0.0040	0.012
	0.06957	1.35	0.004	0.0040	0.009
	0.07342	1.36	0.004	0.0030	0.008
API X52 - Weld PSL2	0.22 max.	1.40 max.	0.025 max.	0.015 max.	0.04 max.
API X70 - Weld PSL2	0.22 max.	1.65 max.	0.025 max.	0.015 max.	0.06 max.

API X80 - Weld PSL2	0.22 max.	1.85 max.	0.025 max.	0.015 max.	0.06 max.

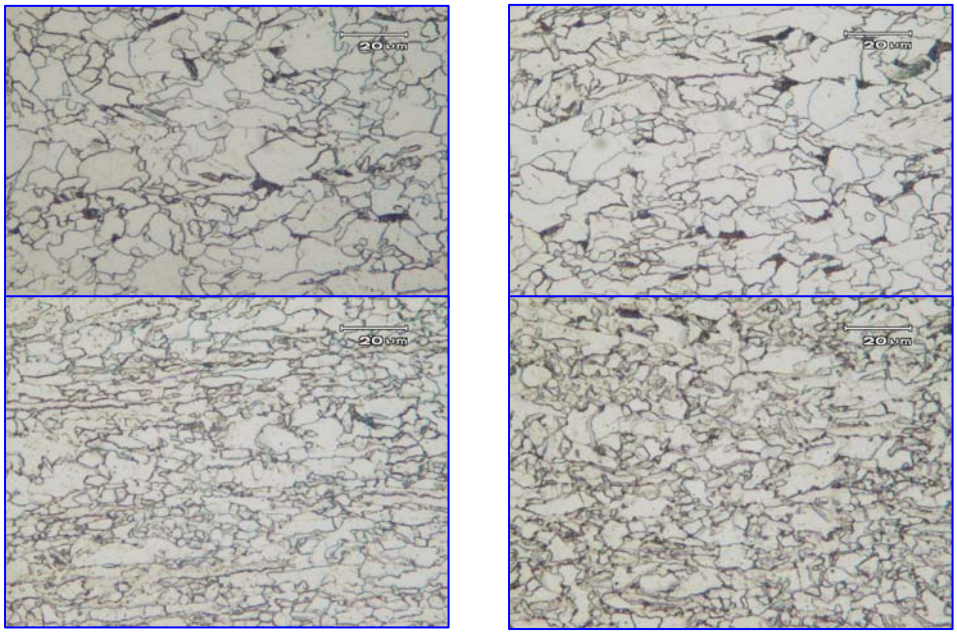

Figure 5.3. Microphotography of both X52 (a-b) and X70 (c-d) steel samples showing a mixed ferrite structure with small concentration of carbides at grain boundary besides the coarse grains, few grains of pearlite, and greater fine ferrite grain concentration in Grade X52. Longitudinal sections, a-c. Transversal sections, b-d.

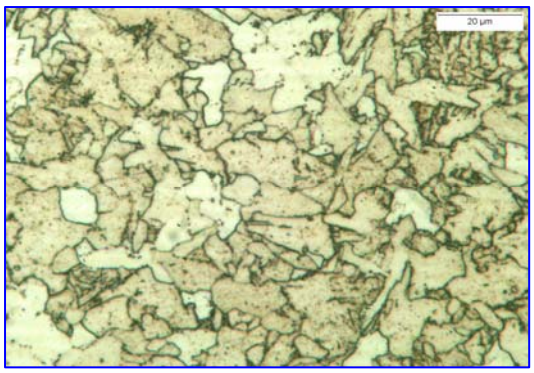

Figure 5.4. Microphotography of steel sample Grade X80 showing an acicular ferrite structure with sub-grain formation.

NOTE: ***The results presented for steel grades X-52, X-70 and X-80 refer to the specifications of these steel samples. The actual yield strengths for these grades were closer to 70 ksi (X-52), 80ksi (X-70) and 90 ksi (X-80). Thus the data for hydrogen absorption and its effect on the observed hydrogen cracking susceptibility should be considered for the actual strengths.***

5.4 Magnetic Properties of Steel Samples

As it was described in Sections 2.2.2, 2.3.2 and 2.3.2, MFL tools magnetize the pipeline steel and detect anomalies in the pipe wall. The pipeline materials, low-carbon steels, are soft-

ferromagnetic alloys. The parameters of saturation, remanent magnetization, and coercivity of these steels depend on the particular chemical composition, heat and rolling treatment, residual stresses, and density of inclusions. Remanence, which is a measure of the remaining magnetization when the driving field is dropped to zero, is the most important factor for the purpose of this work.

A rule of thumb is that approximately three times the value of the steel coercivity is needed to magnetize common low carbon steels for the purpose of magnetic testing. However, detailed research has found values for the magnetization that are outside of the typical value ranges. These typical values for industrial steels are: B_s = 1.4-1.8 Tesla, H_c = 3.5 – 20 Oe, and B_r = 0.3-1.5 Tesla.

To establish the magnetic flux density required to saturate the X52 and X70 steel samples, a magnetic property hysteresis test was run in the Electronics and Electrical Engineering Laboratory – Electromagnetic Division of the National Institute of Standards and Technology (NIST) in Boulder, CO. Magnetization hysteresis loops were measured with a transverse-field vibrating-sample magnetometer at room temperature in maximum applied fields of 0.6 T (6000 Gauss). Magnetization was computed as magnetic moment per unit mass of metal and expressed in units of Kilogauss.

Figure 5.5 shows the magnetization curves obtained from the test. The saturation magnetic flux density (B_s) for the radial or transverse samples is approximately 1.8 Tesla (18,000 Gauss) and for the longitudinal samples is 1.6 Tesla (16,000 Gauss). Notice that in the radial direction of the pipe the maximum saturation magnetic field density (B_{sR}) of both steels, Grades X52 and X70, is slightly greater than in the longitudinal direction (B_{sL}), due to the rolling texturing obtained in the tested specimens. Moreover, the magnetic field required to saturate the steel in the radial direction (H_{sR}) is significantly lower then the field needed in the longitudinal direction (H_{sL}) of the pipe. The radial-direction B_{sR} is barely greater than the longitudinal-direction B_{sL} probably because of the test specimen shape; while H_{sR} is considerably lower then H_{sL} because of the orientation of grains after hot rolling.

On the other hand, the remanence point of pipeline steel of Grade X52 is shown in Figure 5.6. Remaining magnetic flux density in both lateral and radial sample is approximately 1 Tesla (10,000 Gauss). This parameter was considered when the experimental results were analyzed.

5.5 Magnetic Flux Density Generation

To reach the saturation flux density on the steel samples, an electromagnet based upon the Biot-Savart law (Cullity 1972) was initially constructed as a magnetic induction source. The electromagnet was made using a pure iron rod and a wrapped, high electric conductivity-isolated wire, through which an electrical current passes. However, the magnetic flux density measured from this straight electromagnet was insignificant (less than 500 Gauss).

Because of the failure of the electromagnets to reach any significant magnetization level, strong permanent magnets (neodymium-iron-boron), like those used in Magnetic Flux Leakage In-Line Inspection tools, were chosen as the magnetic induction source of the magnetic drive

system. A unique configuration of larger pyramid-shape (maximum energy product N45) and smaller square-shape and circular-shape magnets (maximum energy product N50) constitute the magnet setup (se Figure 5.7). This individual configuration generated a magnetic induction greater than 0.97 Tesla (9,700 Gauss) (see Figure 5.8).

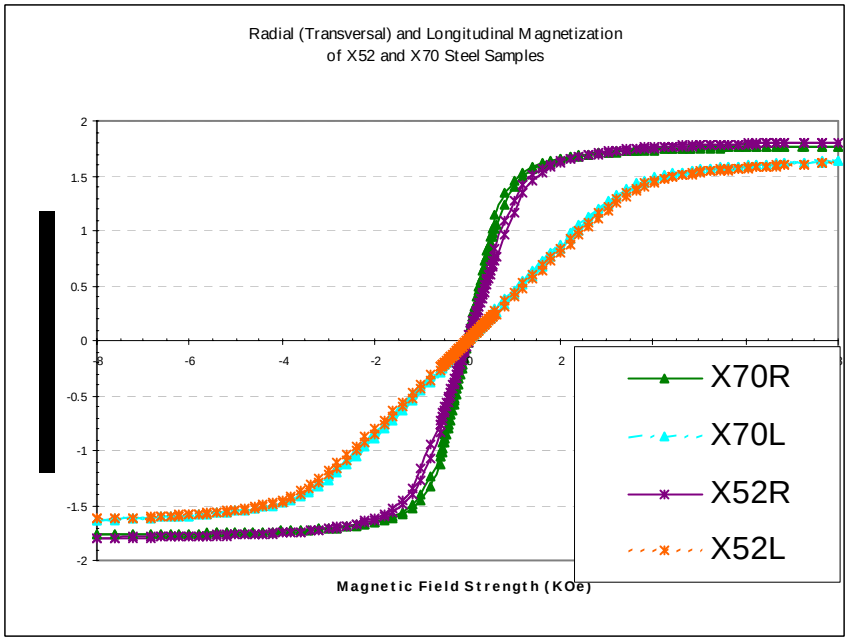

Figure 5.5. Magnetization test results for radial steel of Grades X52 and X70 in radial and longitudinal directions.

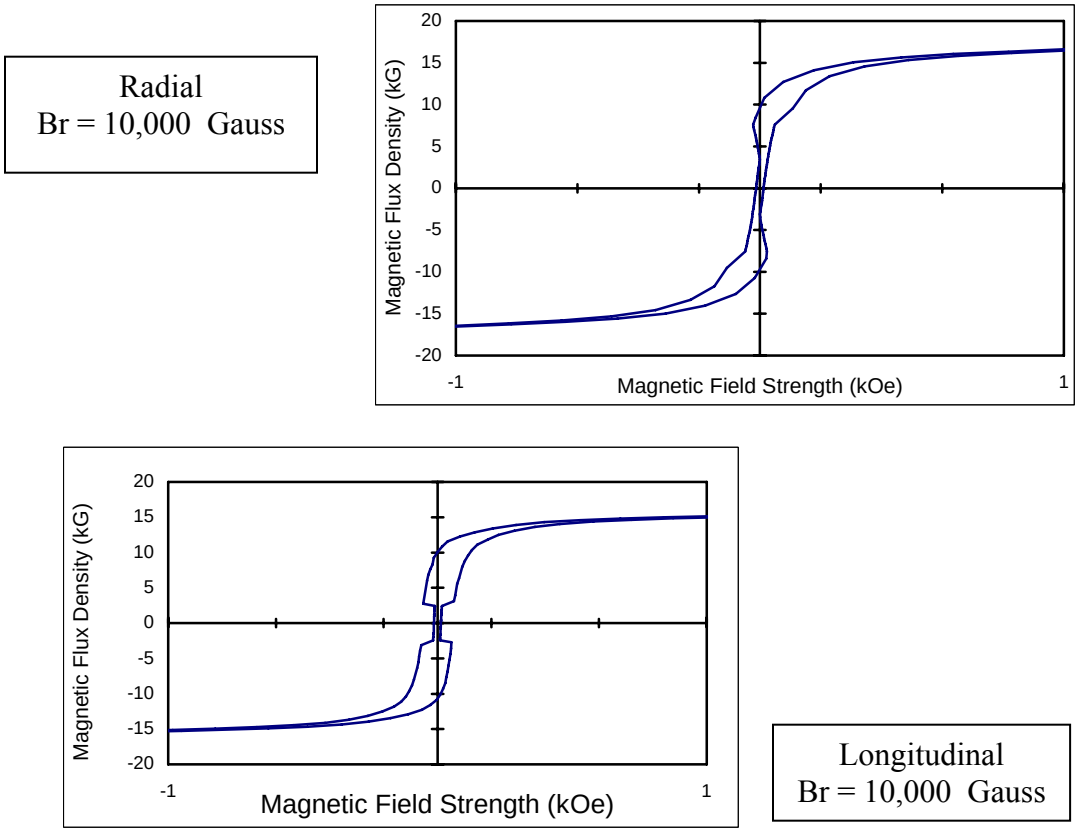

Figure 5.6. Remaining Magnetic Flux Density (Br) – Steel of Grade X52.

Figure 5.7. Magnet configuration. Larger 2 in^2 (1290.3 mm^2)-pyramid-shape magnet and smaller circular-shape and square -shape magnets.

With the purpose of increasing the magnetic flux density of the system, two similar configurations are bonded as north-south pole. The assembly of these permanent magnets produced a magnetic induction greater than 1.9 Tesla (19,000 Gauss). This value is high enough to saturate the high strength pipeline steel samples.

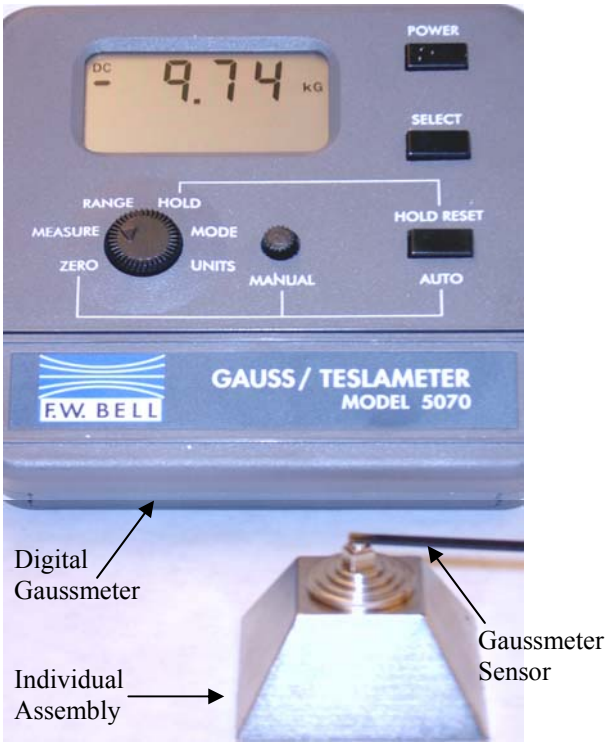

Figure 5.8. The individual assembly of pyramid and small permanent magnets generates a strong magnetic flux density: 0.96 Tesla (9,600 Gauss).

5.6 Magnetic Set-Up Frame

Because the individual set of permanent magnets generated a strong magnetic flux density at the top of the assembly, the force due to the north-south pole attraction was extremely high. This attraction force between the two sets of permanent magnets was so high, that it was not possible to manually handle the magnet without danger of hand damage. As it was unexpected, initial setting-up methods caused damage of some small magnets. This unpredicted collision between the permanent magnets destroyed some of the small 1 mm (0.039 in)-thick square-shaped and circular-shaped magnets. With the intention of preventing more destruction of small magnets and uncontrolled set-up methods, an engineering design concept was employed. An aluminum base magnet-setup frame achieves the safe and controllable sample-magnet assemblage.

Principles of mechanical engineering and screw-powered systems were considered for designing the frame. Figures 5.9 through 5.12 illustrate the engineering drawings to be used for constructing the assembly tool. Two principal notched, guided 1 in (25.4 mm)-thick aluminum sheets hold the two sets of permanent magnets that are bonded and separated by a power screw. The material of the power screw and bearing box, based upon availability and cost, is low carbon steel. Unfortunately, this selection createed another engineering problem: the magnetic attraction of them to the magnets. The magnetic attraction between the magnets and the powered system is reduced only by distance. A 1 in (25.4 mm)-thick and a ½ in (12.7 mm)-thick aluminum sheets separate them sufficiently to control manually the magnet setting.

This magnet-setup frame (see Figure 5.13) reduced considerably the sample-magnet assembly time.

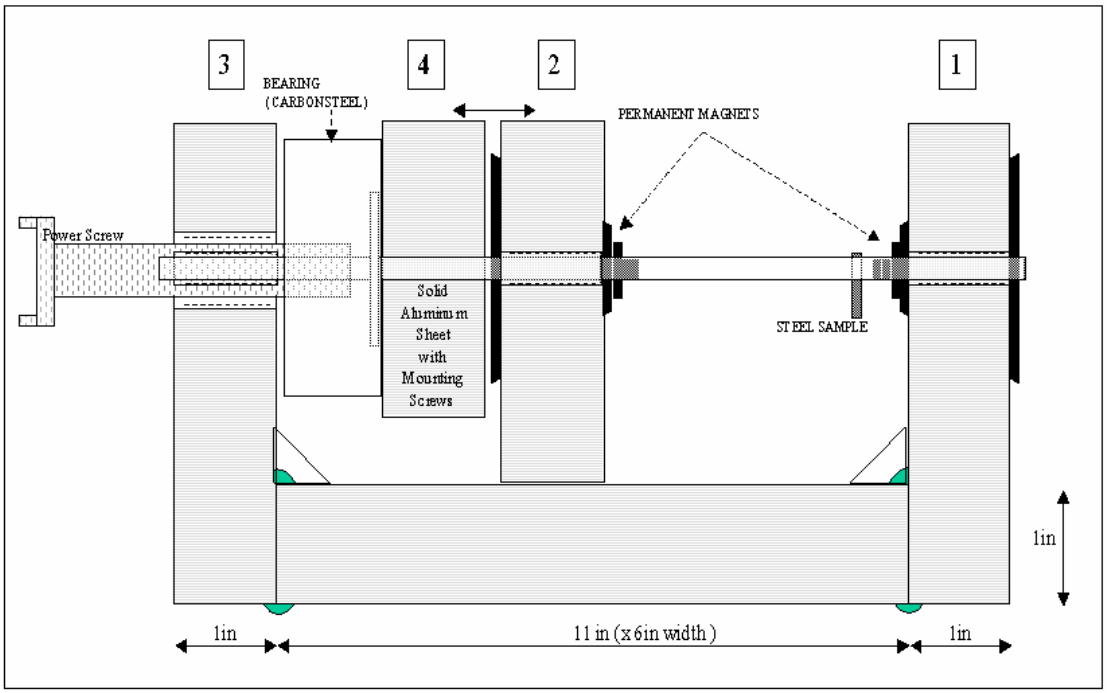

Figure 5.9. Engineering diagram of the magnetic-setup frame.

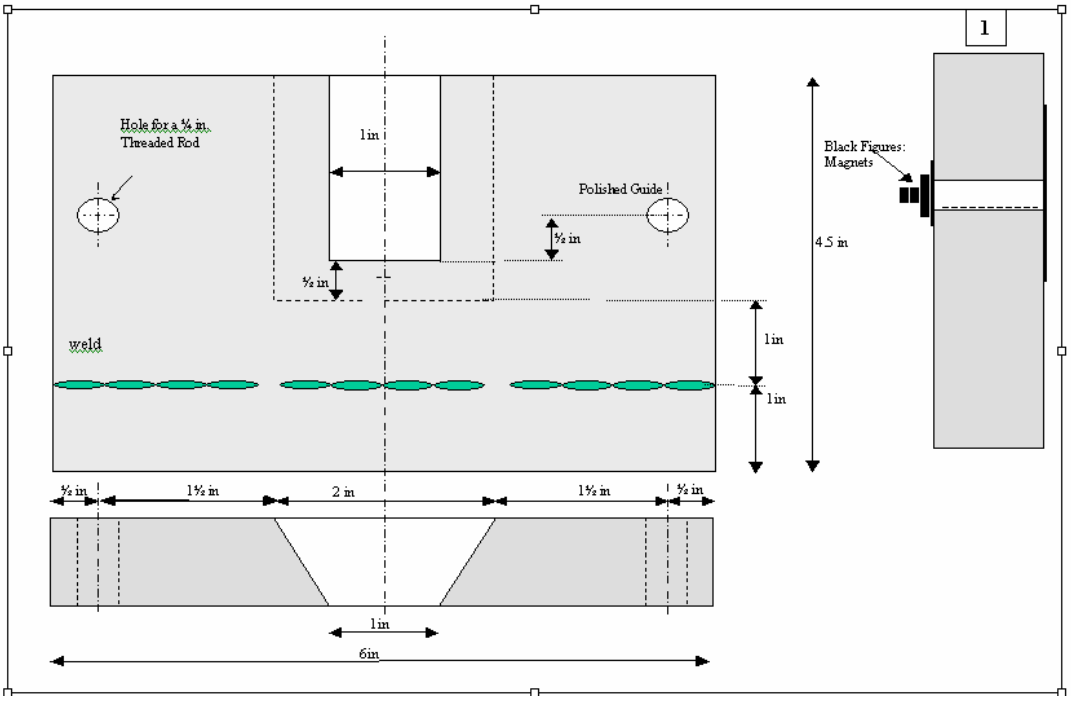

Figure 5.10. Engineering diagram of fixed aluminum sheet No. 1 from Figure 5.9.

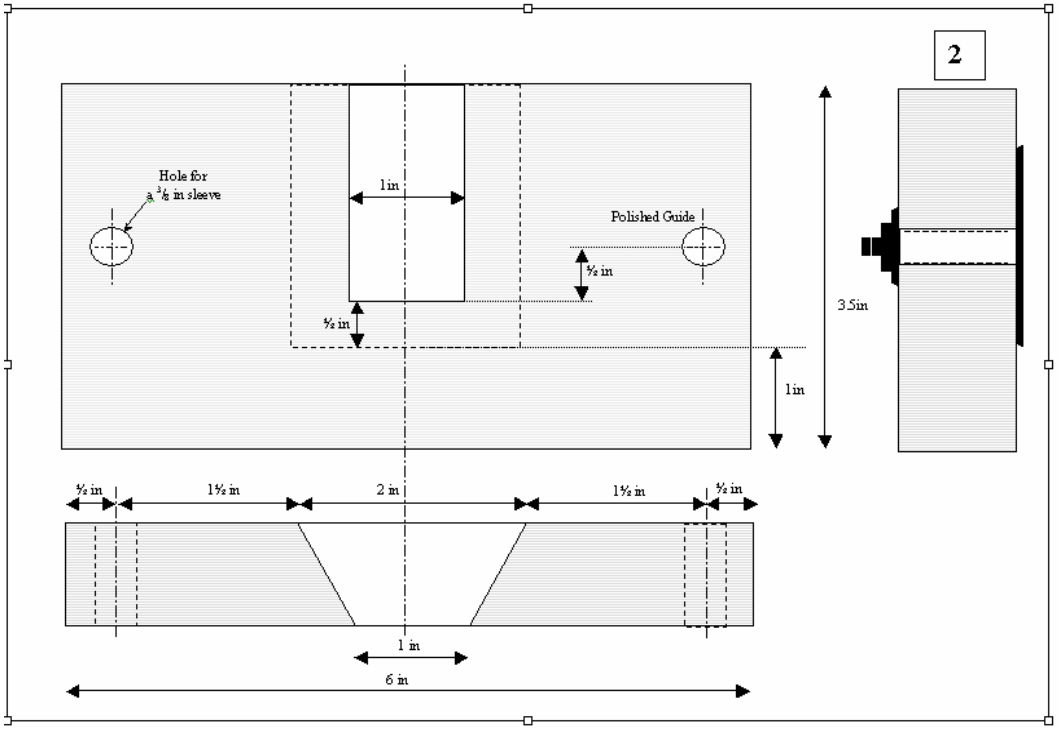

Figure 5.11. Engineering diagram of traveling aluminum sheet No. 2 from Figure 5.9.

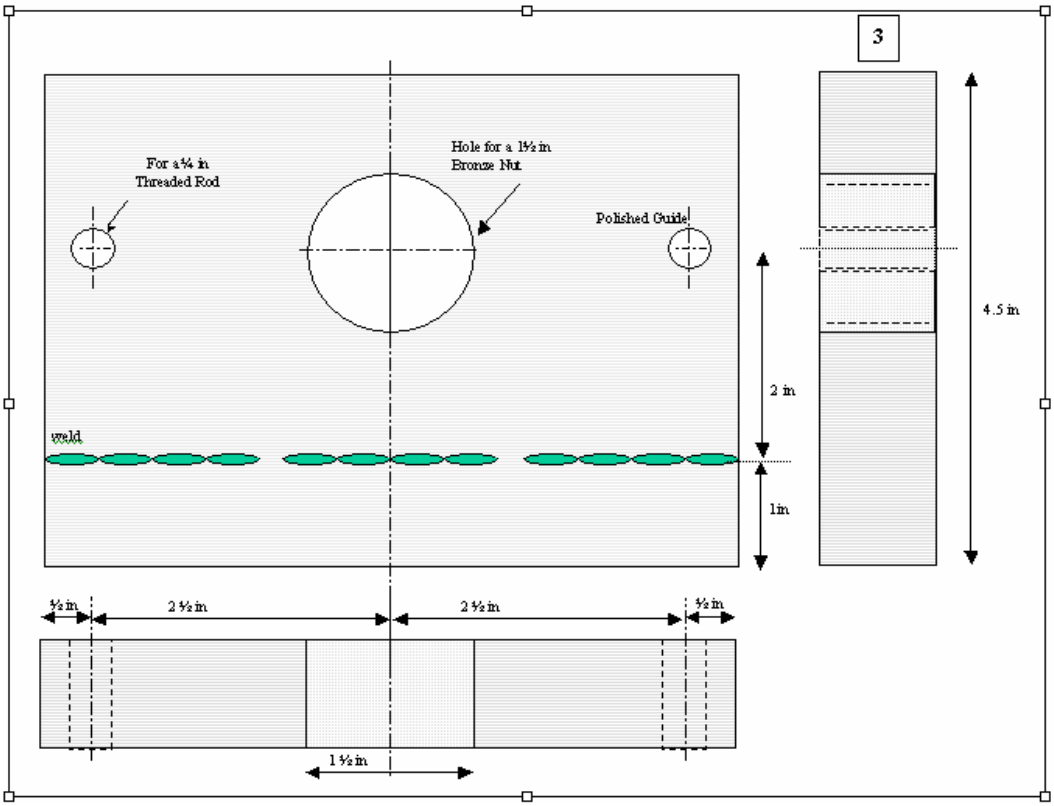

Figure 5.12. Engineering diagram of fixed aluminum sheet No. 3 from Figure 5.9.

With the purpose of determining the magnetic flux density saturating the pipeline steel samples, a Gauss meter sensor is placed between the samples and the permanent magnets. The recorded magnetic induction value exceeded the digital Gauss meter range: 2 Tesla – 20,000 gauss (see Figure 5.14). The achieved magnetic flux density value was greater than the saturation (B_s) value obtained from the magnetization tests (see Figure 5.5).

5.7 Electrochemical Techniques (H Diffusion / H Solubility)

The assessment of magnetization effects on hydrogen damage of pipeline steels started with the measurement of the absorbed-hydrogen concentration with and without magnetic flux density after several periods of charging time. This set of cathodic charging experiments showed the fact that the hydrogen concentration was affected by the magnetic flux density without differentiating the effect either on hydrogen diffusion or hydrogen solubility. Consequently, an electrochemical technique would be used to determine the effect of magnetic flux density on the permeation rate and mobility of electrolytic hydrogen. To experimentally perform this technique, the Devanathan-Stachurski cell (covered by the standard ASTM G148) and the Barnacle Electrode (covered by the standard ASTM F1113) were initially selected for use in this investigation.

It is worth noticing that although these techniques are extensively described in this section, Devanathan and Barnacle Electrode cells are not the methods from where concluding results

were obtained. Several unrealistic results using Devanathan cell led to the changed experimental plan. The cell could not be calibrated due to improper grounding of the galvanostat.

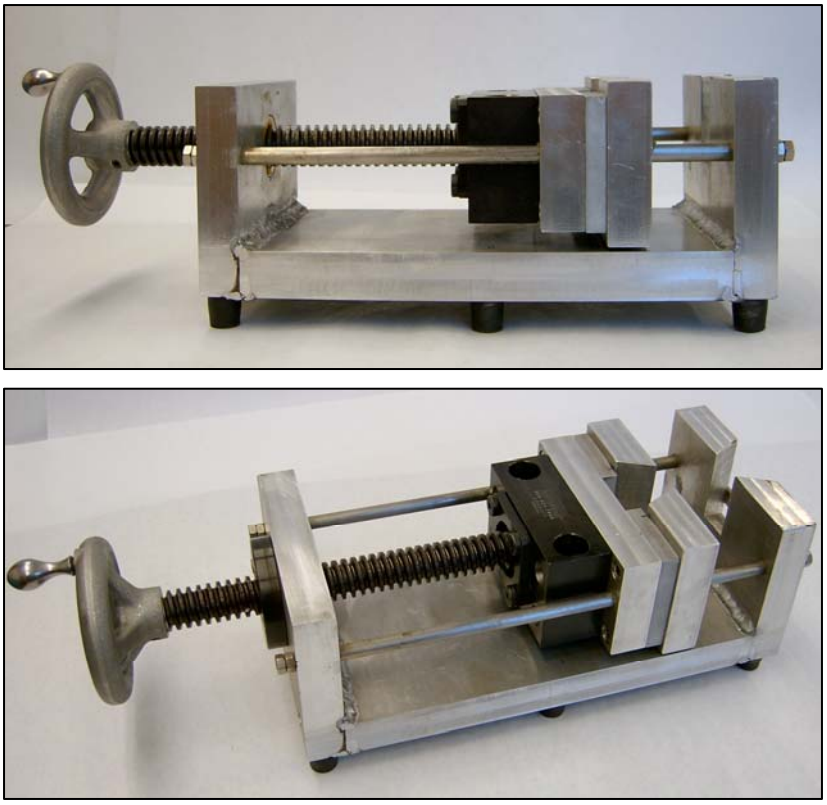

Figure 5.13. Magnetic-Setup Frame.

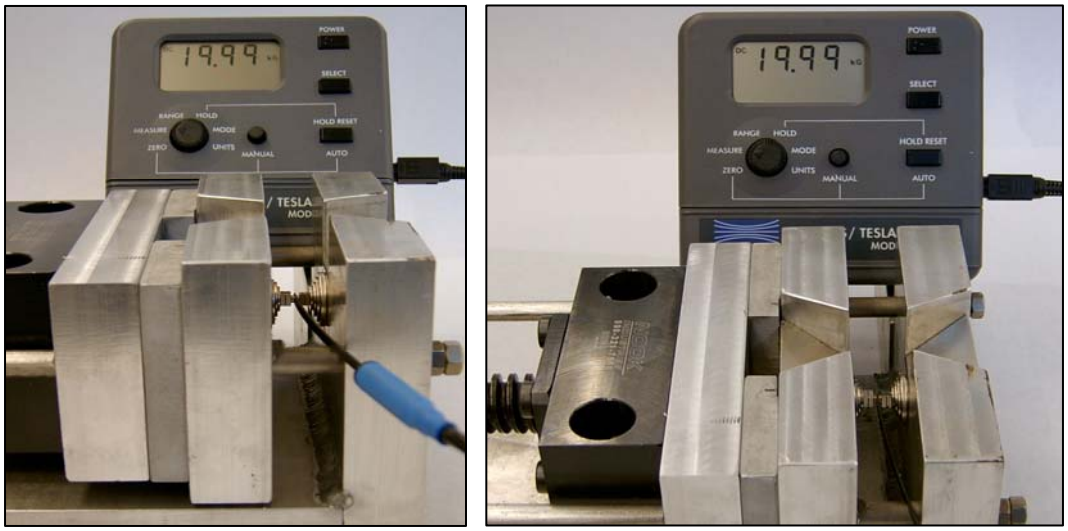

Figure 5.14. The recorded magnetic induction measurement between the steel sample and the permanent magnets. The magnetic flux density obtained exceeds the Gauss meter range of 2 Tesla (20 kilo-Gauss).

5.7.1 Devanathan-Stachurski Permeation Cell

Based on the theory that the rate of permeation of hydrogen is controlled by diffusion in a material, the Devanathan-Stachurski electrochemical cell measures the instantaneous rate of permeation of electrolytic hydrogen through membranes of materials. This technique is used to evaluate the severity of hydrogen charging produced by diverse sources (corrosive environments and cathodic polarization) and to determine the effect of processing, metallurgical, and environmental variables, as well as properties of materials on diffusion of hydrogen in metals.

The Devanathan-Stachurski cell utilizes a metallic membrane forming the partition wall between two compartments of a twin electrochemical cell with electrodes in each one. One side of the membrane (the charging side) is covered with absorbed atomic hydrogen produced by cathodic reduction at a certain fixed level (current), while on the opposite oxidation side, the amount of atomic hydrogen is zero always.

The charging cell contains an acid solution while the oxidation cell contains an alkaline electrolyte. The first cell promotes hydrogen charging while in the second cell the membrane surface is kept passive at a potential high enough to oxidize by anodic polarization (potentiostatic circuit) any hydrogen coming through the membrane. The current in the anodic potentiostatic circuit obeys the Faraday's Law measuring the instantaneous rate of permeation of hydrogen.

In other words, in the charging or cathodic electrochemical unit the hydrogen evolution reaction is produced. Applying a fixed and constant current to the specimen surface the reaction takes place. While the anodic or oxidation electrochemical unit is where the hydrogen atoms arrive and are oxidized after permeating through the membrane.

5.7.1.1 Apparatus

The Devanathan-Stachurski cell (see Figure 5.15) consists of two identical electrochemical units, charging and oxidation, terminating in standard ½ in (12.7 mm) pipe flanges. Each flange holds a Teflon O-ring facing the refined and flat membrane. The assembly is joined with the membrane in between the O-rings. The electrode in the charging compartment is bright platinum auxiliary and the electrodes in the oxidation cell are a bright platinum auxiliary and Haber Luggin capillary-calomel reference.

The charging or cathodic unit is filled in with 1.3 liters of an acid solution, and a constant current density of 50 mA/cm^2 (500 A/m^2) was applied to the cathodic surface of the specimen. The anodic unit is filled in with 1.3 liters of a solution of 0.1N sodium hydroxide and was potentiostatically maintained at 50 mV_{SCE}. It is applied to the anodic surface of the specimen to force the hydrogen concentration on the surface to be zero. Both solutions are previously deaerated by pure argon for 30 min. prior to the test. Pure argon is injected into the outlet compartment to promote stirring. A palladium coating, commercially known as Pallamerse, is applied on the exit surface of the membrane to ensure zero hydrogen concentration on the charging side. Enhanced efficiency of the hydrogen atom oxidation reaction is reached once the anodic surface is coated (palladium). Palladium-coating serves as a catalyst for the hydrogen ionization reaction $H^\circ \rightarrow H^+ + e^-$.

The test is performed and the experiment parameters are controlled electronically using two Princeton Applied Research Model 273A potentiostatic/galvanostatic units. Commercial computer software is utilized to record the oxidation current. The technological features of this particular galvanostatic unit are inappropriate for hydrogen permeation experiments. The invalid results were acquired because this electronic device is not sensitive to very low current changes, which is typically required for this experimental method.

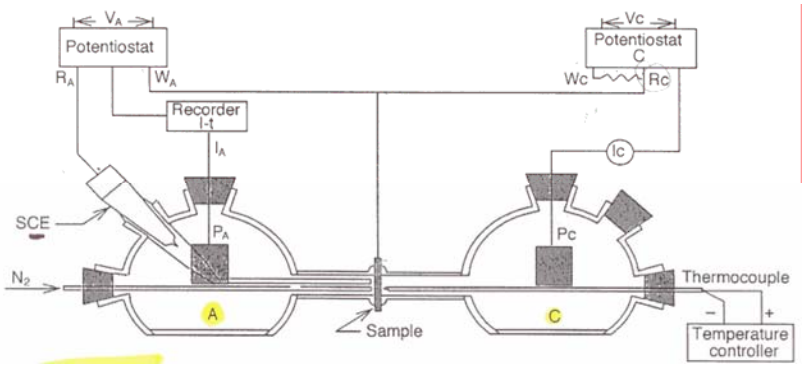

Schematic Diagram (Yen, S.K., et al.)

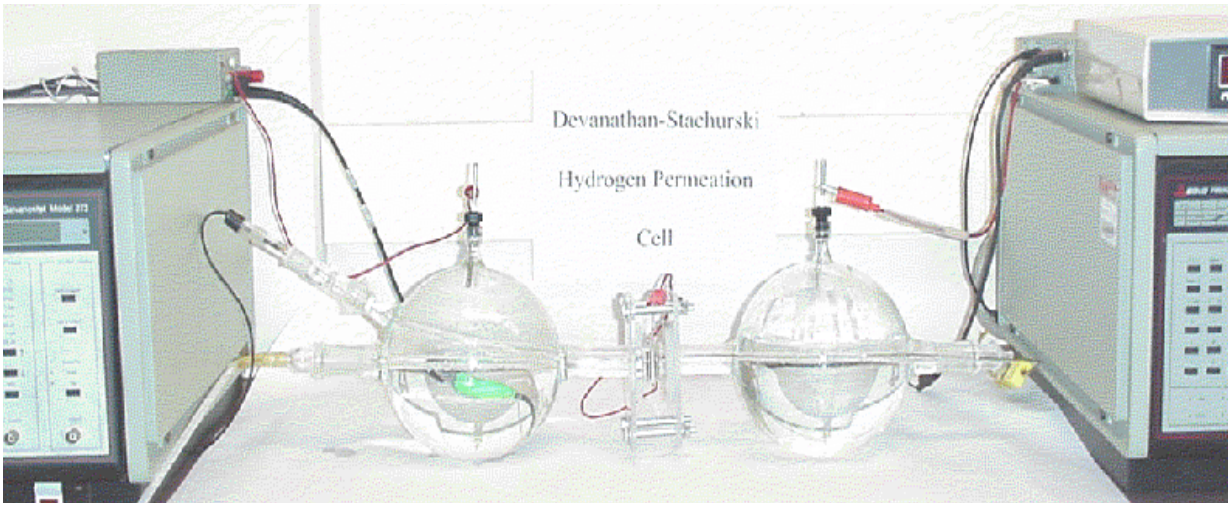

Figure 5.15. Hydrogen permeation cell (Devanathan-Stachurski) and schematic diagram. C: cathodic unit. A: anodic unit. P_C-P_A: auxiliary platinum electrodes. R_C-R_A: reference P_C electrodes. W_C-W_A: working electrodes.

5.7.1.2 Test Environment

The test environment was designed to facilitate the ease and reliability of making hydrogen permeation measurements. Because the laboratory environment is prepared using analytical grade reagents, a pre-electrolysis treatment was not used. Commercial pure distilled water was

also utilized to prepare the environment. The volume of solution to metal area ratio was as high as 550 ml/cm^2.

For the reason that pH and temperature of the solutions have a significant effect on hydrogen permeation, both parameters were continuously monitored. The experiments were carried out at room temperature and a constant pH. Any variation was recorded. The charging cell was thermostatically controlled at room temperature for the period of the experiment.

From previous works, the initial acid solution to fill the cathodic cell was 0.2N acetic acid (CH_3COOH) - 0.1N sodium acetate ($CH_3COOHNa$) solution. However, preliminary experiments showed a low rate of reaction between the solution and the steel sample. Because the charging or cathodic solution is strongly affected bythe hydrogen permeation rate, this represented a critical parameter of the Devanathan-Stachurski technique. Consequently, any variation from its original selection would have been straightforwardly accepted if preliminary results identifed it as an uncertain parameter. Therefore a new cathodic solution was developed and was:

- 1N H_2SO_4
  1M = mass/L / GFW (gram formula weight)
  1N = 1M * Z
  Acid: Z is the number of hydroxide ions liberated
  1M = mass/L / (98) = mass/L / 98
  1N = 1M * Z (sulfuric acid=2) = mass/L / 49
  Concentration: 49 gr./L (1N)
  Liquid Solution Density: 1.84 gr/cc.
  Final Concentration *1N H_2SO_4* = 49 / 1.84 = 26.6 cc/L

In contrast, the alkaline anodic solution to fill in the anodic cell was 0.1N sodium hydroxide. This oxidation solution was not modifed because of the slight effect on measurements. The calculations were:

- 0.1M NaOH
  1M = mass/L / (23+16+1) = mass/L / 40
  1N = 1M * Z (=1) = mass/L / 40
  Concentration: 40 gr./L = 1N
  0.1M = 0.1 * 1N
  Concentration *0.1M NaOH* = 4gr/L

5.7.1.3 Specimens

Specimen characteristics were critical parameters to determine hydrogen permeability rate. The preliminary specimens used in this study were 1.60 mm (0.063 in) thick, 1 in^2 (645.16 mm^2) total area, flat, and surface grinding finished. However, since thickness, total area, and surface finish had a significant effect on the hydrogen permeation experiment, these parameters could be considerably modified if needed. Thicker samples increased experiment time, small specimens affected electrical contact area, and surface finish at oxidation side affected hydrogen extraction.

Mechanical cutting was the selected method to machine the specimens because electrochemical discharge machining could introduce hydrogen into the metal, modifying the initial concentration. The initial selected surface finish was given by a common surface grinder, it was up to #600 grit at both charging and oxidation side. Both surfaces were similarly treated in order to experimentally demonstrate the principal subject of this work.

After polishing, the specimens were cleaned in non-chlorinated solvents for five minutes to remove traces of chemicals and to be degreased before the experiment and then rinsed with acetone for five minutes. Finally, the sample was dried by warm air blowing on it just before the electrochemical cell assembly.

Although it is well know that a palladium coating on the charging face of the specimen affects the sub-surface hydrogen concentration, a thin palladium coating is applied. This suitable material *"can minimize variations in surface conditions during the permeation transient and yield repeatable transients provided the specimen thickness is adequate"* (ASTM G148 1997). This surface was considered acceptable for these experiments.

5.7.1.4 Test Procedure

This test procedure is based on ASTM G148-97 "Standard Practice for Evaluation Uptake, Permeation, and Transport in Metals by an Electrochemical Techniques." The deaeration began by actively purging on the immediate addition of the solution to the charging cell. It rapidly removed oxygen that could contaminate the solution and affect the environment concentration and specimen surface.

The commercial software M365 SoftCorr III from Princeton Applied Technology was used to monitor the total oxidation current as a function of time. The experiment was run until the anodic current achieves steady-state condition. The preliminary test results permitted refinement to all experimental parameter.

5.7.1.5 Environmental Control and Monitoring

Based on ASTM G148-97 "Standard Practice for Evaluation Uptake, Permeation, and Transport in Metals by an Electrochemical Techniques."

5.7.1.6 Procedures for Analysis of Results

Based on ASTM G148-97 "Standard Practice for Evaluation Uptake, Permeation, and Transport in Metals by an Electrochemical Techniques." When the instantaneous rate of hydrogen permeation was recorded, the hydrogen diffusion coefficient can then be calculated by a variety of methods (Devanathan and Stachurski 1962). As propose of this study, the time lag method, the breakthrough time method, and the rise time method were used.

5.7.1.7 Reporting

Based on ASTM G148-97 "Standard Practice for Evaluation Uptake, Permeation, and Transport in Metals by an Electrochemical Techniques." In addition, a record of the diffusion coefficient values plotted D_{eff} as a function of the magnetic field was accomplished.

Based on previous studies on hydrogen permeation in pipeline steels, the expected plot of the recorded anodic current as a function of time is shown in Figure 5.16. When the instantaneous rate of hydrogen permeation is recorded in this way, the hydrogen diffusion coefficient can be calculated by a variety of methods (Devanathan and Stachurski 1962). As propose of this study, both the time lag and the breakthrough time methods were selected for this stage of the research. They are shown as follow:

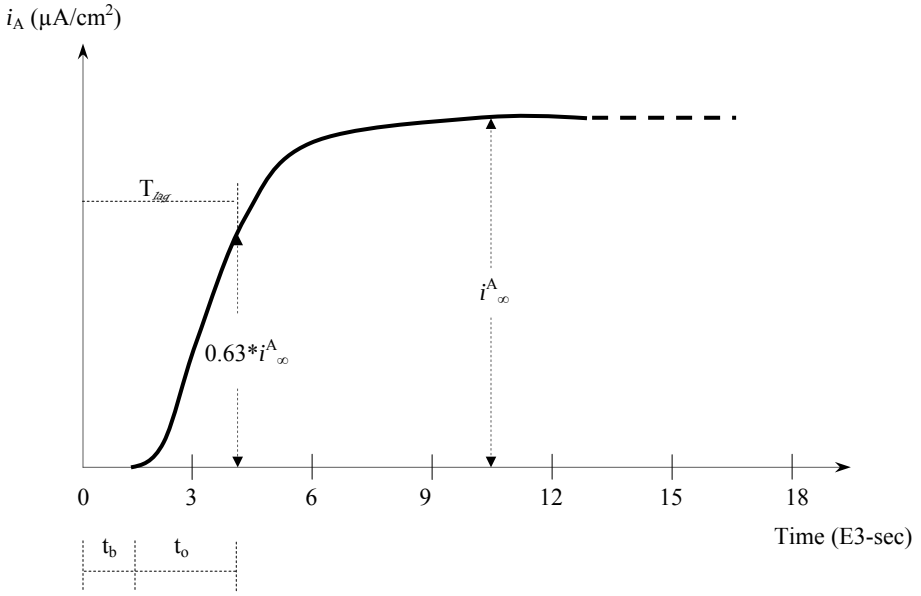

Figure 5.16. Typical transient record (Devanathan and Stachurski 1962).

5.7.1.7.1 Time Lag Method.

The time lag is the classic method of obtaining the diffusion constant. Time lag represents the elapsed time at which the hydrogen flux (J) through the steel specimen equals 0.63 times the steady-state hydrogen flux (J_{ss}), or $J_{(t)}/J_{ss}$= 0.63. The steady-state hydrogen flux is the amount of hydrogen passing through the membrane-exposed area at the time when the anodic (permeation) current reaches a steady value (i^A_∞, plateau). The effective diffusion constant or coefficient may be calculated by relating time lag and the thickness of the membrane (L) as follows:

$$D_{eff} = \frac{L^2}{6 * T_{lag}} \ (cm^2/sec) \qquad (5.1)$$

5.7.1.7.2 Breakthrough Time Method

As time lag is defined as the summation of rise time constant and breakthrough time, the effective diffusion constant is related to the breakthrough time by the following equation:

$$D_{eff} = \frac{L^2}{15.3 * T_{lag}} \ (cm^2/sec) \qquad (5.2)$$

5.7.2 Barnacle Electrode Cell

The barnacle electrode method has been developed to determine mobile hydrogen concentration under service environments and to correlate hydrogen concentration with delayed failure in materials such as high-strength steels.

The principle of the barnacle electrode method is based on the electrochemical technique used in the Devanathan Permeation Cell. The barnacle electrode method essentially makes use of the extraction side of the Devanathan cell and requires that the sample be previously charged with a uniformly known distribution of hydrogen. This method was originally considered to evaluate the magnetization effect on HIC in pipeline steels; however, because the previously described galvanostatic unit must be utilized as well as in the Devanathan cell, this electrochemical cell was finally not considered. Nevertheless, the concept of pre-charged samples with hydrogen was the principal idea to develop the selected electrochemical technique: cathodic charging along with hydrogen concentration measurement using an elemental analyzer. Although the Barnacle Electrode apparatus was constructed (see Figure 5.17A), some specimens were obtained from the tested pipeline samples (see Figure 5.17B), and the procedure had been revised from the standard ASTM F-1113, this method was not pursued any further.

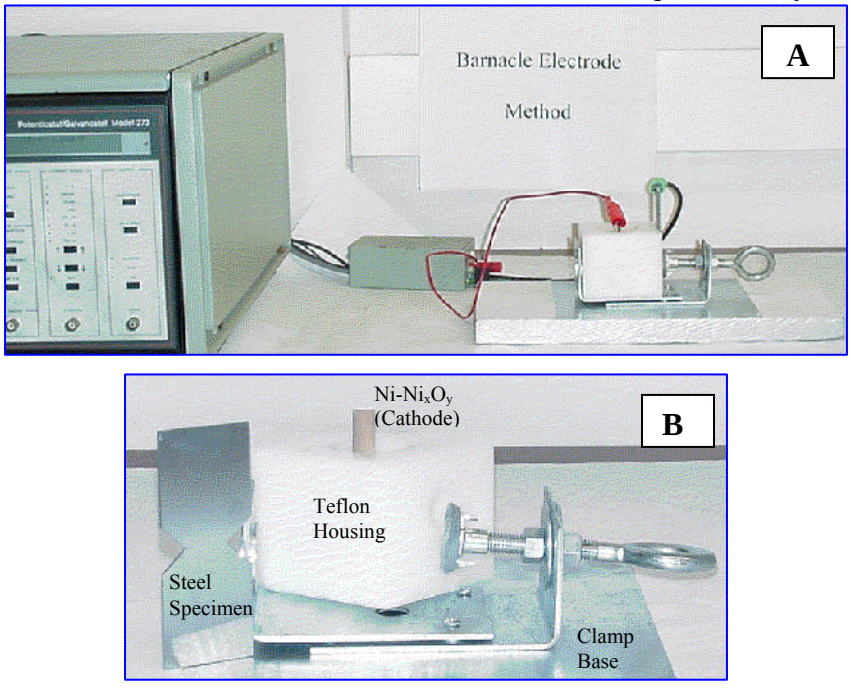

Figure 5.17 Barnacle Electrode Method – Configuration and Apparatus.

5.8 Hydrogen Cathodic Charging and Hydrogen Content

This electrochemical technique and direct hydrogen content measurement method represent the principal procedure to assess the magnetization effect on hydrogen concentration and hydrogen damage in pipeline steels in this research. Hydrogen is produced at the steel surface, not unlike a cathodic protection system, and then is induced into the steel as a function of time. The cathodic charging cell utilizes an acid solution as electrolyte and the final total absorbed hydrogen content is measured using the elemental analyzer. The results are plotted in a comparative graph, where hydrogen content without magnetization is compared to hydrogen content after the sample is magnetized. This procedure is applied for determining the magnetization effect on hydrogen content in straight as-received samples and in bent samples. The comparative HIC evaluation utilizes just the cathodic charging cell because the hydrogen determinator device is not required.

To determine hydrogen concentration in a steel sample after a hydrogen charging experiment the LECO-Hydrogen Determinator RH-404 was used. Because this elemental analyzer requires a 1 g-sample, several 0.35x1.0 in (8.89x25.4 mm) parallelepiped-shape specimens were sectioned from the selected steels (API 5L Grades X52, X70, and X80). One group of samples was employed for the hydrogen charging experiment without magnetization and the second group for the experiment was conducted under a strong and uniform magnetic field. The same methodology was applied when the coldwork effect was included in the investigation. All the specimens were subsequently cleaned in non-chlorinated solvents, rinsed with acetone for five minuets, and baked at 400ºC for one hour to remove any remaining hydrogen from manufacturing.

For the first experiment, the samples were mounted on an epoxy resin. The epoxy resin reduces the galvanic cell effect in the Hydrogen-Charging System and ensures complete submergence of charged area into the solution. The uncharged hydrogen concentration was determined with a three-specimen set using the LECO-Hydrogen Determinator RH-404. The other mounted-specimen set, were electrically connected to a copper wire and was surface finished until a common bench grinding finish was obtained. The sample was submerged into the charging solution as is showed in Figure 5.18. On the other hand, after several experiments, it was realized that if an alligator clip is electrically isolated with coating and then submerged into the charging solution, no electrical interference would be produced. This is why a different electrochemical cell apparatus was used. This device is shown in Figure 5.18

For the magnetization experiment, the samples were placed between two sets of permanent magnets as is extensively explained in the previous sections on Magnetic Flux Density Generation and Magnetic-Setup Frame. The sample-magnet assembly was submerged into the charging solution (see Figure 5.19). To avoid any attraction between the magnets, a plastic frame was placed between them. The charging solution was prepared using analytical reagents and commercial pure distilled water. Even though the massive coated magnets are not electrically in contact with the sample (anode), some bubbles were produced on magnets surface due to the high acidity (pH ~ 0.4) of the charging solution.

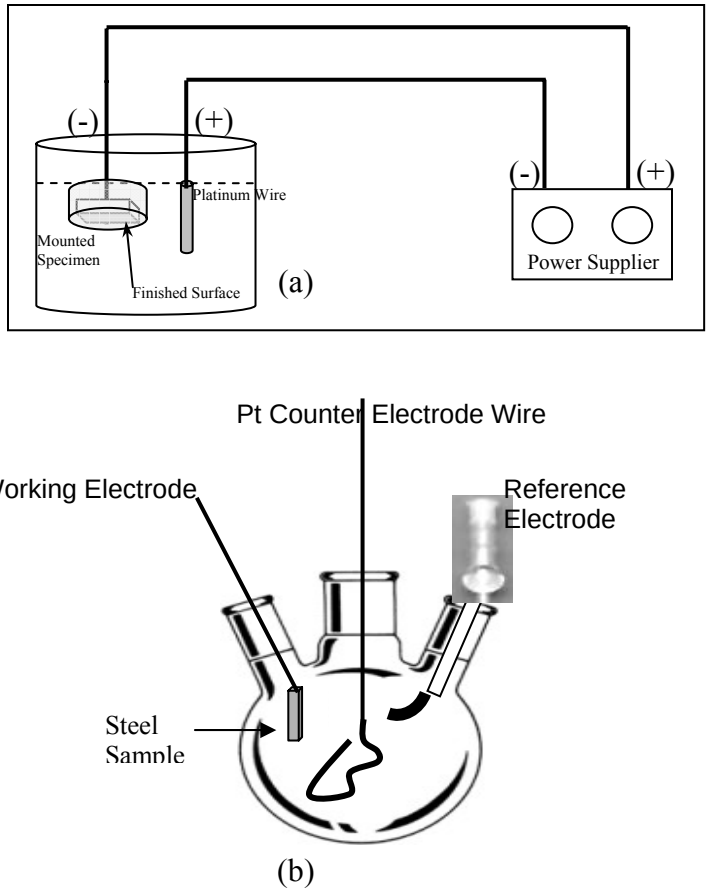

Figure 5.18. Schematic diagrams of hydrogen cathodic charging equipments (a and b) for the charging experiment without a magnetic field applied to steel samples.

The cathodic charging was carried out electrolytically in a fresh-500 ml solution of 1N H_2SO_4, using a platinum wire as cathode and the steel sample as the anode. The temperature (T_{room}) and pH (up to 0.4 at t = 0) of the solution were continuously monitored. The test is performed and the experimental parameters were controlled electronically using a potentiostatic/galvanostatic unit (Princeton Applied Research Model 273A) and the commercial measurement software M352 SoftCorr III (see Figures 5.20 and 5.21). With the purpose of establishing the required potential to promote hydrogen-atom oxidation reaction, a polarization curve was obtained (see Figure 5.22). Even though there are three different types of steels, the polarization curve for the steel of Grade X52 can be used for the other two steel grades. Small variations in composition of steels do not affect the polarization curve significantly. This experimental curve showed that the hydrogen charging experiment must be run at a potential greater than 500 mV to ensure hydrogen dissociation. Consequently, the current rate was fixed at 0.05 A/cm^2.

The exposed area of each specimen was monitored and recorded in the corrosion software setup files. The achieved hydrogen concentration ([H], ppm) values were plotted as a function of time (t, hr) with the purpose of distinguishing the effect of the magnetic flux density. The charging time was fixed in intervals of 1, 2, 3, 6, and 8 hours to establish the equilibrium

hydrogen concentration. That is, the plateau of hydrogen concentration curve which represent the equilibrium point (see Figure 5.23).

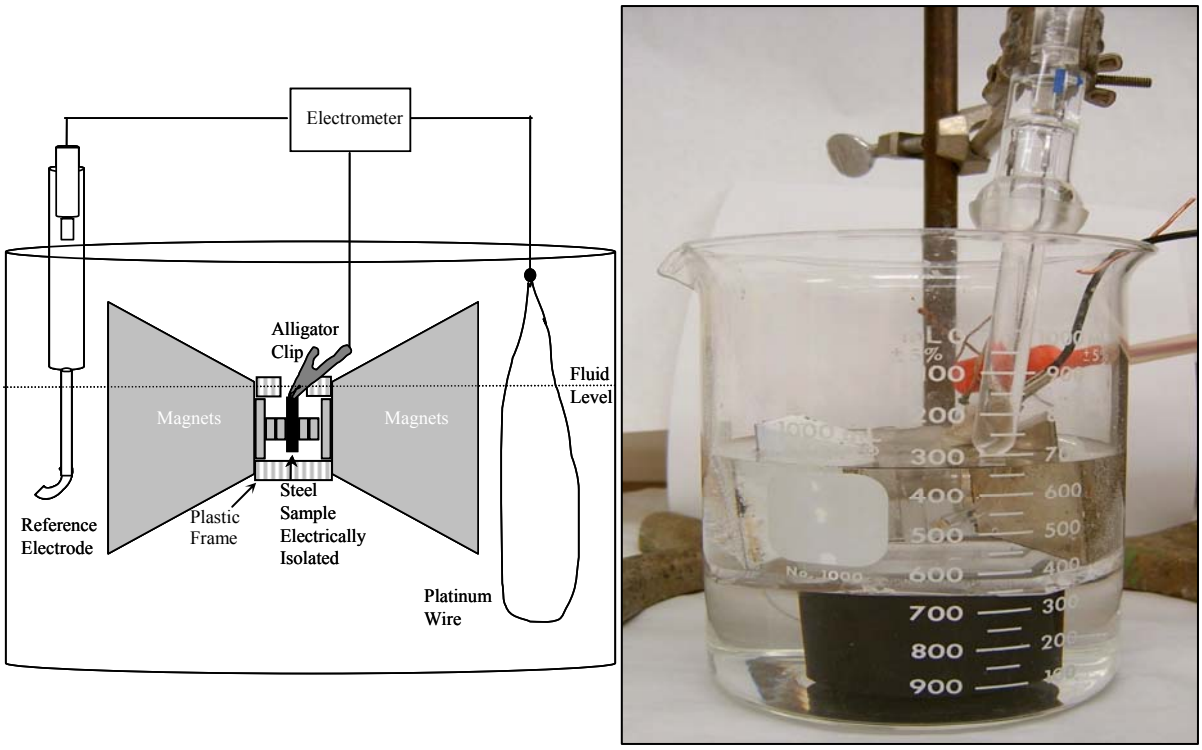

Figure 5.19. Magnet-sample setup submerged in charging solution (1N H_2SO_4).

Figure 5.20. Potentiostatic/Galvanostatic Unit Princeton Applied Research Model 273A.

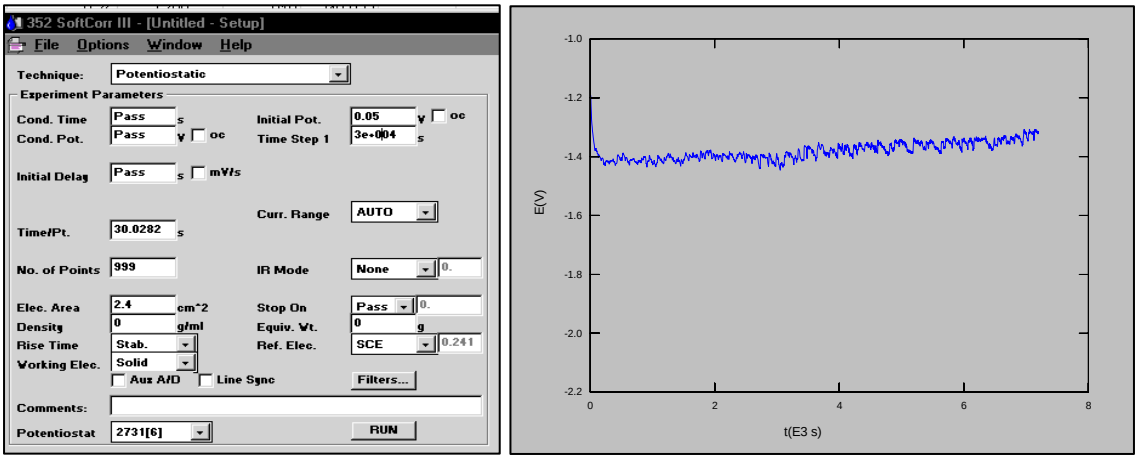

Figure 5.21. Windows of commercial corrosion software: 352 SoftCorr III. Setup data and (b) Potential-time plot.

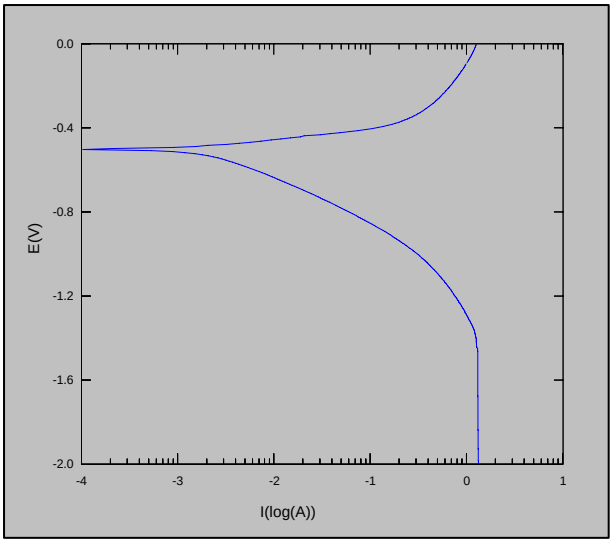

Figure 5.22. Polarization Curve of steel Grade X52 (Software: 352 SoftCorr III).

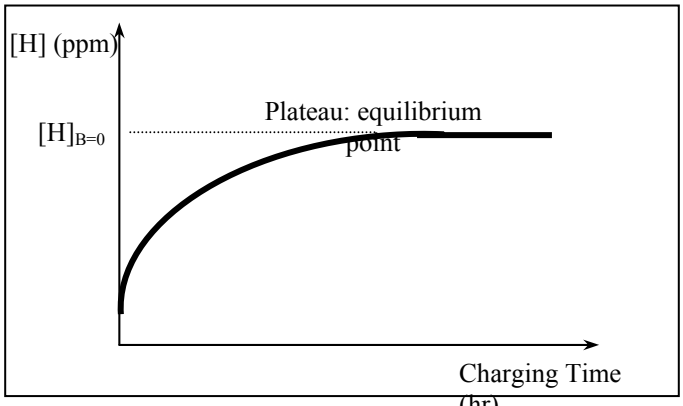

Figure 5.23. Schematic representation of the equilibrium value.

5.9 Hydrogen Content Determination

Once steel samples were charged with hydrogen, the hydrogen content was measured using the LECO Hydrogen Determinator RH-404 (see Figure 5.24). This determinator utilizes the inert-gas fusion technique to measure specifically the total hydrogen concentration in inorganic materials. These materials, such as steel, require high-temperature fusion to effectively release hydrogen.

Measurement and furnace units constitute the LECO Hydrogen Determinator RH-404. The weight and physical dimension of a steel sample used for testing was limited. The normal specimen weight range is 0.5-1.0 gram while the maximum diameter is 7.5 mm (0.295 in) and the maximum length is 18 mm (0.708 in).

Consequently, to satisfy these limitations, the pipeline steel specimens are sectioned in small pieces, which are charged before hydrogen content detection. The weight of steel samples is roughly one gram while the physical dimensions are approximately 4 mm wide x 5 mm high x 10 mm long (0.157 in x 0.197 in x 0.394 in).

With the purpose of calibrating the LECO Hydrogen Determinator RH-404, three steel standard 5.8 ±0.4 ppm-samples were used before any pipeline steel (Grades X52, X70, and X80) samples are dropped into the electrode furnace. Figure 5.24 shows the calibration point before the hydrogen content was determined for a six hour charging steel X52-sample under a magnetic flux density of 2 Tesla (20,000 Gauss).

5.10. Residual Stress (Cold-Work) Effect on Hydrogen Concentration due to Magnetization

Although it is widely known that cold work increase hydrogen absorption in low-carbon steels, the effect of high magnetic flux density on hydrogen intake in cold-worked high strength steels was undetermined till now. To assess this phenomenon, conventional small specimens such as those used in hydrogen charging tests are sectioned for cold-worked steel samples.

Magnetic flux leakage (MFL) in-line inspection tools are capable of detecting mechanical damage components such as dents, cold work, residual stresses/strains, and removed metal. Part of the detecting-signal generated at a mechanical damage defect is due to geometric changes; i.e., for instance, a reduction in wall thickness due to metal loss causes flux to leak out. The rest of the signal is largely due to magnetic changes; i.e., for instance, changes in magnetization properties that result from stresses, strains, or damage to the microstructure of the steel.

Pipeline steel is considered to be cold worked if its grains are in a distorted condition after plastic deformation below recrystallization temperature. Plastic deformation produces an increase in the number of dislocations resulting in a higher state of internal stress. Because plastic deformation or cold working affects the lattice structure, all the steel mechanical properties that are dependent on lattice structure are also significantly affected. These properties are tensile and yield strength, hardness, and ductility. Tensile strength, yield strength and hardness are increased, while ductility is decreased in steels. Distortion of the lattice structure

hinders the passage of electrons, decreases electrical conductivity and reduces corrosion resistance in alloys.

(a) Measurement Unit (b) Furnace

Figure 5.24. Photograph of LECO RH-404 Hydrogen Determinator. Standard 1 gr-5.8 ppm samples are used before pipeline steel experiments to ensure calibration. The monitor displays hydrogen content of a standard steel sample: 5.78 ppm of hydrogen.

The state of a cold-worked material is defined in terms of percentage cold-work or percent area reduction. That is: percentage cold-work = [(Initial Area – Final Area) ÷ Initial Area] x 100. To assess the magnetization effect on hydrogen absorption in pipeline steels under high level of residual stresses, cold-worked steel specimens have been tested. Although cold-work is measured in terms of area reduction, any mechanical testing method that induces high level of residual stresses in the pipeline steel can be employed. For example, a bending testing machine induces enormous amount of residual stresses in a material even though the percentage of cold-work can not be measured using conventional equations. Within the purpose of this research, the effect of diverse levels of residual stresses or cold-work on the absorption of hydrogen in pipeline steels under an applied magnetic field has been illustrated as a comparative study.

Although the initial plan contemplated the use of conventional deformed tensile test sample, a different method of applying residual stress was finally chosen.

With the purpose of reducing cost and time, previous work regarding pig dent inspection and technology were studied in order to identify an alternative technique of stressing. For example, Beuker and Rahe (2005) defined an analytical, geometric model to introduce a high-quality in-line inspection process for mechanical damage, dents, that can improve the management of the pipeline integrity evaluation. This geometric model applies three different shapes of dents, from which the ‘sharp dent with an opening angle’ was selected as the best model to simulate residual stress levels. Figure 5.25 shows the geometric model.

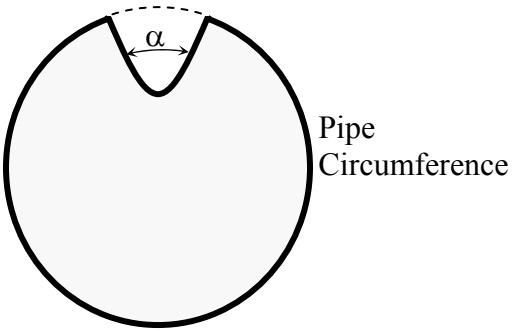

Figure 5.25. Geometric model used by Beuker and Rahe (2005) and considered as a reference to define cold-work bending samples.

Taking advantage of the available bending machine and three sets of angle blocks, the bending specimens were produced. The first set corresponds to the as-received pipeline sample and is called 180º specimens; i.e., unbent specimens. The other three groups correspond to the bent samples at different bending angles; i.e., 120º, 90º, and 60º specimens. This bending method corresponds to a 'free bending technique.'

Pipeline steel samples were loaded to various levels of bending stresses and the effect of the residual stresses under a magnetic induction on hydrogen absorption was measured. To achieve comparable results, the experiment was run under same characteristic of the hydrogen-charging test for steels of Grades X70 and X80 because they are higher-strength steels.

The three sections of pipe to be evaluated were obtained from API welded pipes (see Figure 5.26a). The bending-test specimens were sliced from these as-received short sections of pipes (see Figure 5.26b) and loaded to various levels of bending stresses. No standard bending test specimens were designed, but a conventional bending machine was utilized.

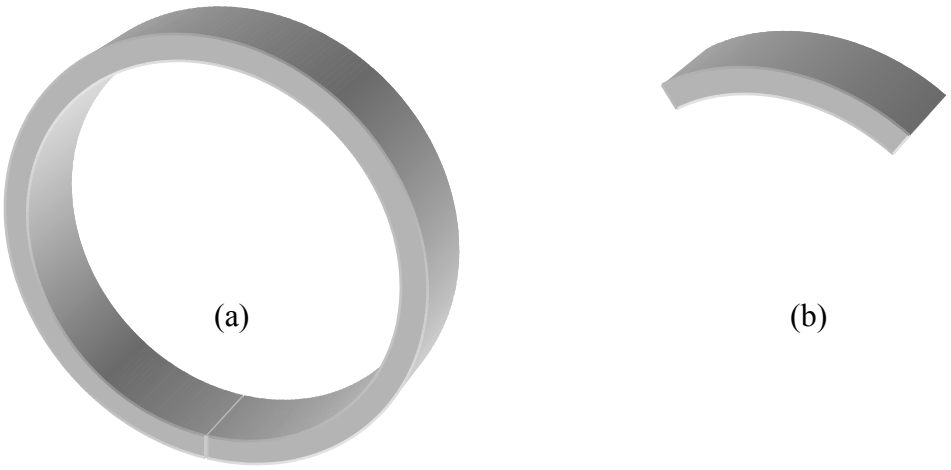

Figure 5.26. Schematic representation of the evaluated line pipes sections (a) and bending specimens (b) for steel of Grades X70 and X80.

With the purpose of applying a constant bending load and, at the same time, various stress levels, the coldwork test specimens were bent at different angles (see Figures 5.27). This model was chosen based on the fact that any third-party mechanical damage in line pipes would likely cause angle-shaped dent (see Figure 5.25). The primary purpose of this test was to compare the coldwork effect on hydrogen content in pipeline steels without magnetization and under a strong magnetic field for different residual stress levels, which were given by the bending angles.

The hydrogen concentration [H] values were plotted as a function of bending angles. The 180º bending angle refers to the straight-section of line pipe. The 120º, 90º, and 60º specimens are shown in Figure 5.27. The 60º bending angle represents the highest induced-residual stress level. This level of cold-work was considered as the ideal condition for any hydrogen-induced cracking test. It is well known that excessive cold-working may fracture the material before reaching the desired size and shape. Therefore, all specimens were optically and microscopically evaluated just after bending. No cracks were found on high-level residual stress surfaces.

Hydrogen-charging samples were sectioned from cold-worked bending test samples loaded under different bending angles (residual stresses). Absorbed hydrogen concentration at a constant charging time of three hours was measured and plotted. The coldwork effect on hydrogen absorption in pipeline steels after charging for a period of three hours was shown in a plot similar to Figure 5.28. The coldwork charging time was chosen as three hours because after three hour charging in a 1N H_2SO_4 solution and at 0.05 A/cm^2 current rate, the equilibrium point was reached for the steel of Grades X70 and X80.

5.11 Hydrogen Damage due to Magnetization

There are two standard test methods for evaluating the resistance of materials to hydrogen damage. NACE TM0284 “Evaluation of Pipeline and Pressure Vessel Steels for Resistance to Hydrogen-Induced Cracking” and NACE TM0177 “Laboratory Testing of Metals for Resistance to Sulfide Stress Cracking and Stress Corrosion Cracking in H2S Environments.” However, the evaluation of hydrogen damage in the tested pipeline steels due to magnetization refers primarily to a comparative technique and no standard procedure are applied. NACE TM0284 evaluates the resistance of pipeline steels to stepwise cracking induced by absorbed hydrogen and consists of exposing unstressed specimens to a synthetic solution. In contrast, NACE TM0177 evaluates the resistant of metals subjected to tensile stresses to cracking failure in environments containing H_2S. Test conditions and environment may cause failure by blistering or stepwise cracking. Both tests are commonly conducted at room temperature.

For the purpose of this research, the selected testing method utilizes neither standard solutions nor standard specimens, but a combination of conditions and techniques. The cathodic charging cell with 1N H_2SO_4 solution and preloaded (bent) samples with high concentration of tensile stresses were considered. This non-standard method was designed to preserve the concept that hydrogen embrittlement evaluation is a time-dependent test.

Because conventional tests were performed to determine the effect of hydrogen damage together with applied or residual stresses, the selected evaluation method was conducted using a cold-worked, bent specimen in a 1N H_2SO_4 solution at a current rate of 0.05 A/cm^2. A bending

angle of 60º generates the highest stress level within the whole set of bending specimens. Consequently, several 60º-bent samples were submerged in the solution with and without magnetization for periods of 12, 24, 36, and 72 hours. The specimens were electrically isolated using epoxy coating over the sample except for a small test area. The exposed surface area varied; however, it was carefully protected before painting using a fixed-size tape of approximately 0.5-1.5 cm^2. Figure 5.29 shows a typical cold-worked, 60º-bent Grade X70 specimen utilized in the HIC test. Although the steel bent-sample looks like a 90º turn (optical illusion), this is a 60º-bent specimen.

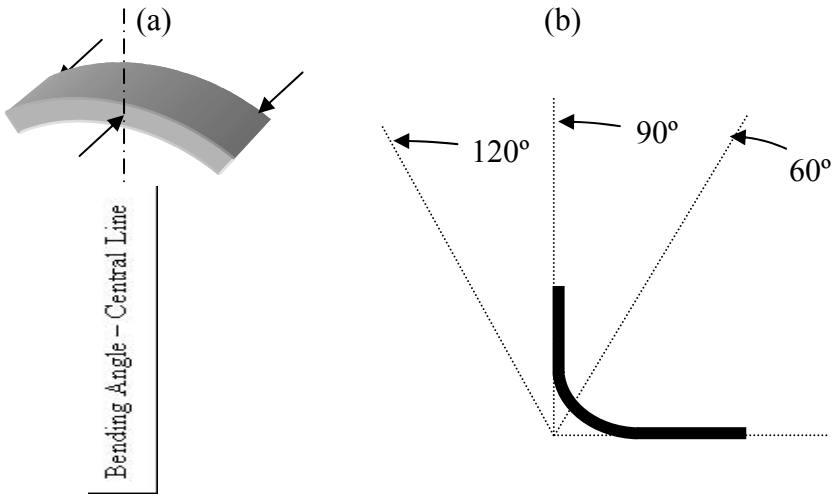

Figure 5.27. Bending load application points (a) and bending angles (b) for coldwork test.

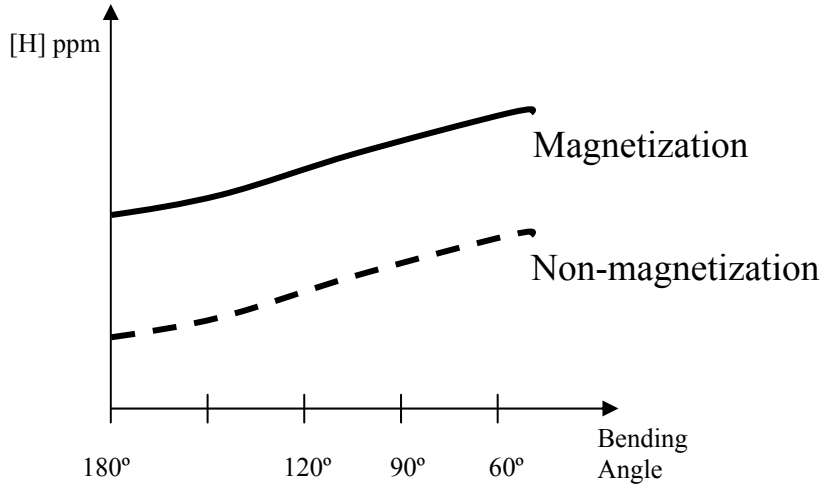

Figure 5.28. Estimated bending angle (coldwork) effect on absorbed hydrogen content.

The specimens were cautiously evaluated employing a stereomicroscope for general examination and an environmental scanning electron microscope (ESEM, Figure 5.30), where evidences of pitting and cracking were observed.

A comparative analysis, with and without magnetization, was based on the presence of pits and cracks after charging time. If there were a significant magnetization effect on hydrogen adsorption in the tested pipeline steels, the presence of these hydrogen damage evidences would be larger when the samples are magnetized during charging time.

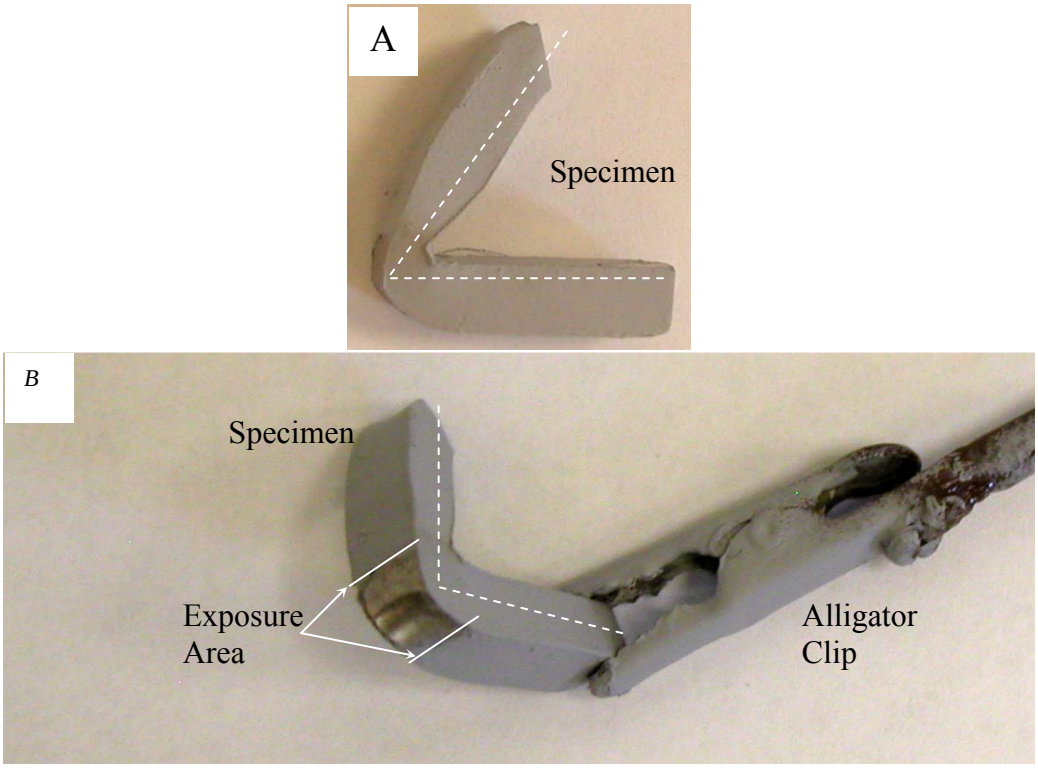

Figure 5.29. Typical cold-worked, 60º-bended Grade X70 specimen - HIC Test. Notice that both the steel sample and the alligator clip are electrically isolated by gray-colored coating. A-top view and B-isometric view.

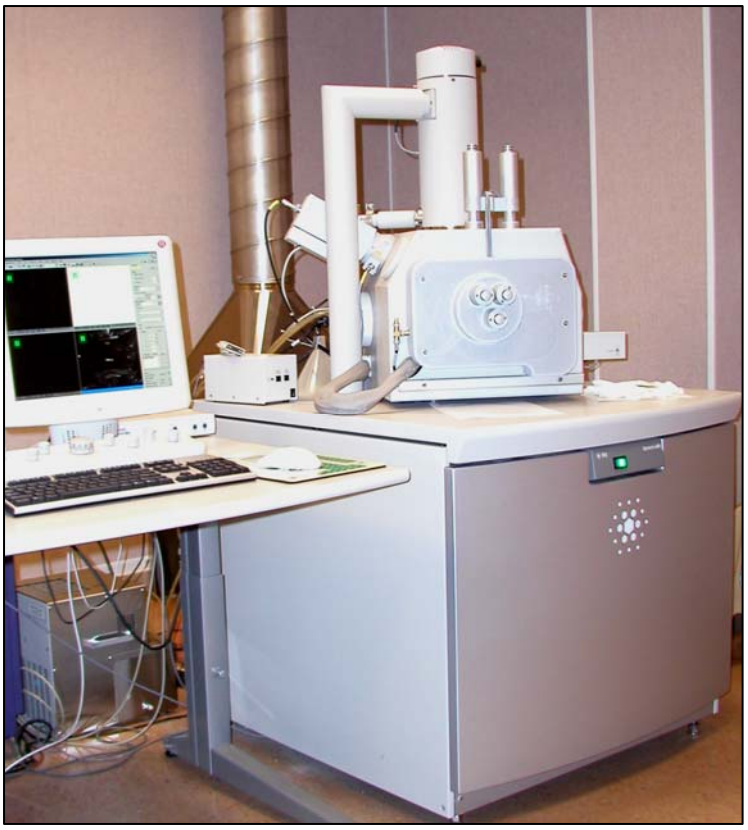

Figure 5.30. Environmental Scanning Electron Microscope FEI Quanta 600.

6. EXPERIMENTAL RESULTS

This chapter presents the results obtained following the experimental procedures described in Chapter Five. The results of the polarization curve test and the assessment of the magnetization effect on hydrogen content in the tested pipeline steels using the cathodic charging cell is discussed in this chapter. Steels of Grades X52, X70, and X80 were used for the magnetization effect on absorbed hydrogen content test, while the other two experiments used only steel of Grades X70 and X80. The two tests were: magnetization effect on hydrogen absorption in cold-worked steel samples and magnetization effect on HIC in thick, high-strength pipeline steels.

6.1 Polarization Curves using Devanathan Cell

As it has been explained, the Devanathan cell was initially selected as the hydrogen permeation test apparatus until unexpected results were obtained. However, the Devanathan cell was used to obtain the polarization curve for the pipeline steels. With the polarization curves the applied cathodic over-potential to ensure the hydrogen evolution reaction: $2H^+ + 2e^- \rightarrow H2$ is determine. Figures 6.1 and 6.2 illustrate the cathodic polarization curves for steel Grades X52 and X70 in 1N H_2SO_4. The polarization curves were obtained using the Galvanostat mode of the Potentiostat/galvanostat unit (Princeton Applied Research Model 273A). The experimental curves demonstrate that the hydrogen charging experiment must be run at a potential greater than -550 mV (-0.550V) to ensure the hydrogen dissociation reaction. Consequently, the current rate was fixed at 0.05 A/cm^2 to guarantee the required cathodic over-potential for further samples.

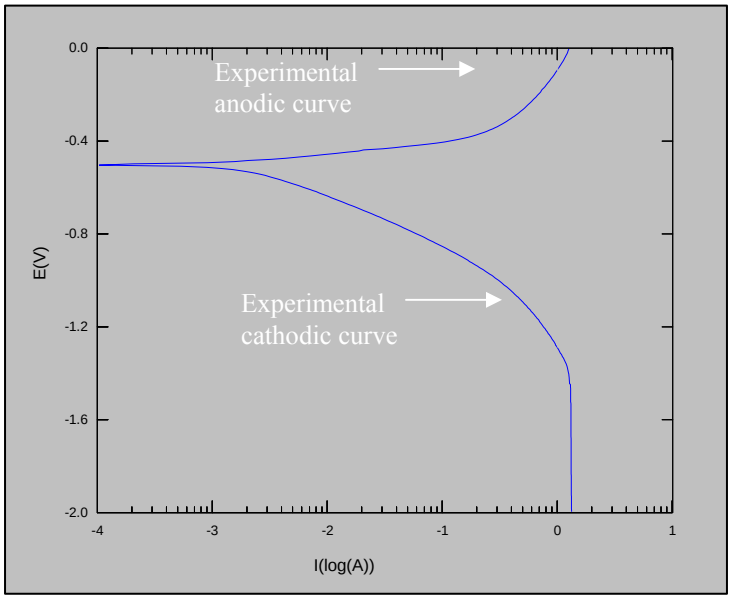

Figure 6.1. Polarization curve for steel of Grade X52 where the cathodic over-potential needed to ensure hydrogen dissociation reaction is below –0.550 Volts.

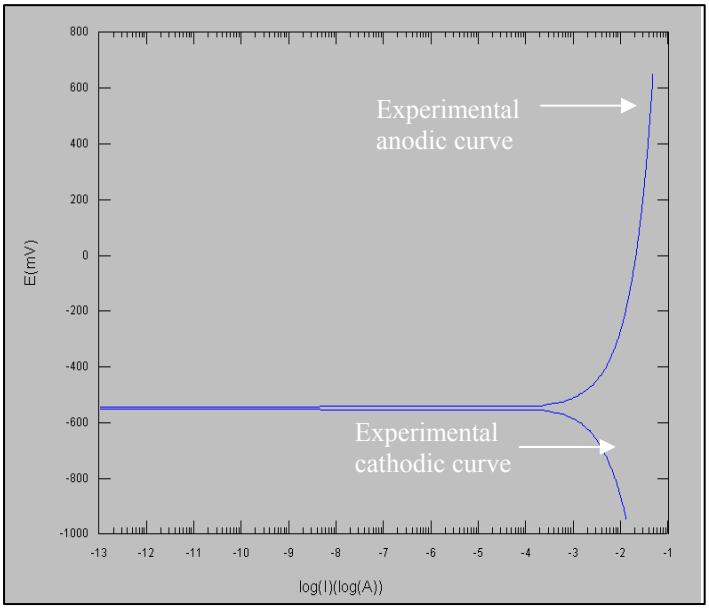

Figure 6.2. Polarization curve for steel of Grade X70 where the cathodic over-potential needed to ensure hydrogen dissociation reaction is below –0.550 Volts.

6.2 Magnetization Effect on Absorbed Hydrogen Concentration

With the purpose of assessing the effect of a strong, continuous magnetic field on absorbed hydrogen content in pipeline steels, several steels of Grades X-52, X70, and X80 samples were cathodically tested. A set of specimens was run without a magnetic field and another set under a two Tesla (20,000 Gauss) magnetic induction to allow comparison.

The hydrogen cathodic charging technique represents the primary electrochemical method to produce hydrogen at the steel surface, similar to a cathodic protection system, and then, induce it into the steel after time. The cathodic charging cell utilizes an acid solution as electrolyte and the final total absorbed hydrogen content is measured using the elemental analyzer. For this electrochemical technique the M352 SoftCorr III data acquisition system from Princeton Applied Technology, and the potentiostat/galvanostat unit Princeton Applied Research Model 273A were used. The setup data and potential-time plots for the pipeline steel of Grade X52 at different charging times are shown in Figure 6.3. Notice that the current rate fixed at 0.05 A/cm^2 and applied on specific electrically exposure-area generates the current value shown in the setup data window as ‘current – step 1’. The ‘time – step 1’ is filled out with the charging time value in seconds; i.e. for a 12-hour experiment, the charging time is 43,200 seconds. Figure 6. 4 also illustrates that, causally, two specimens have identical dimensions, and, therefore, the setup data window shows the same information but the plot is somewhat different. In both cases the hydrogen dissociation reaction is ensured by the applied potential. In the case of pipeline steels of Grades X70 and X80, the results are very similar.

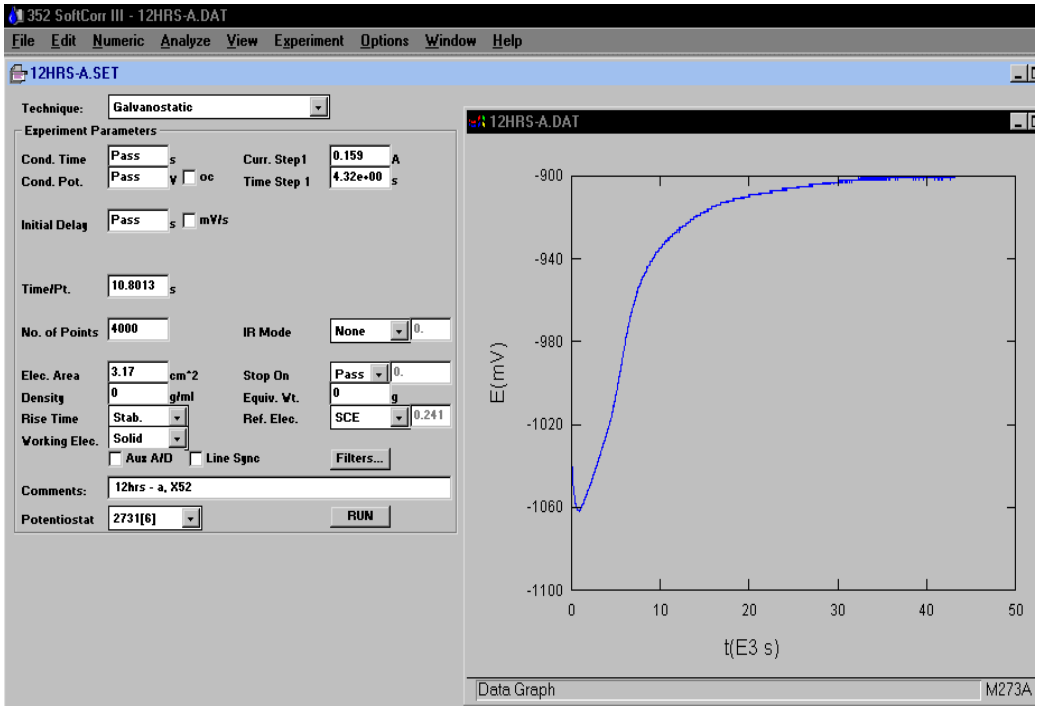

Figure 6. 3. Setup data defined for cathodically charging the pipeline steel of Grade X52 for 12 hours, and the potential-time plot evidencing the experimental potential ensures hydrogen dissociation reaction.

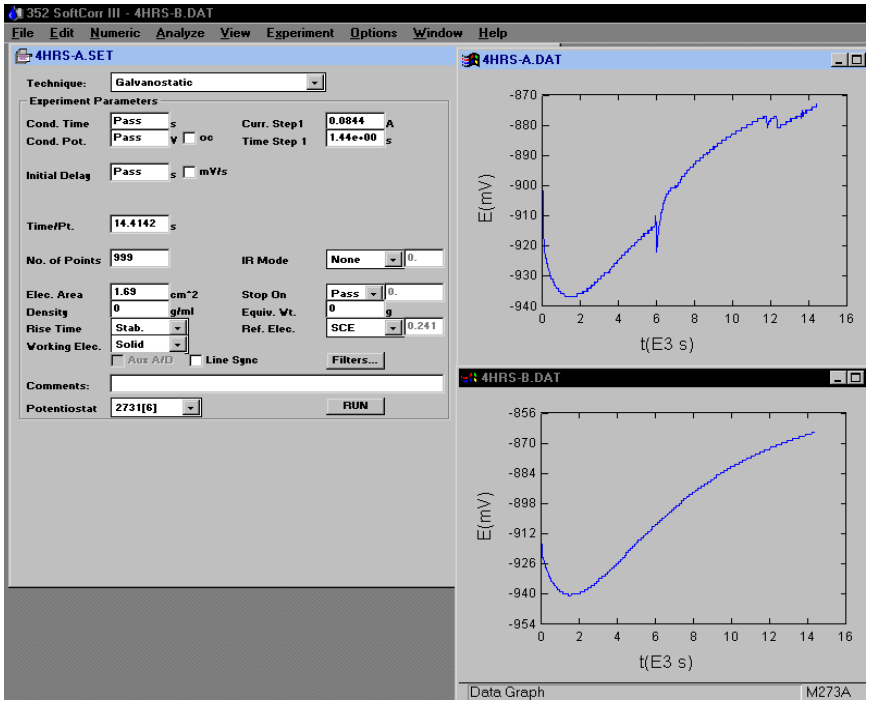

Figure 6. 4. Setup data defined for cathodically charging the pipeline steel of Grade X52 for 4 hours, and the potential-time plots for two similar specimens.

The absorbed hydrogen concentration for each pipeline steel grade at different cathodic charging times has been plotted in Figures 6.5, 6.6, and 6.7. Figure 6.8 shows the comparison results.

Because the steel of Grade X52 samples were machined first and, as a result, the primary samples to be tested, the experimental plot reveals more points for this material. The reason is because the potential equilibrium point, the charging time after which no more hydrogen is absorbed, had to be defined. Therefore, some samples were charged for 1, 2, 3,6, 8, and 12 hours. Other steel grade samples were charged for up to six hours, because the curve tendency was, at that time, well known.

It is important to clarify that the experiments were individually conducted using fresh charging solution from an eight-gallon container with 1N H_2SO_4. The solution concentration was always the same within all of the experiments. The potentiostatic unit was turned on thirty minutes before each experiment and the commercial corrosion software was set up using identical operational parameters, such as the cathodic current rate fixed at 0.05 mA/cm^2. The electrically exposed area of each steel specimen was previously measured and incorporated into the setup data.

The magnetic flux density was continuously measured before experiments. The same configuration of magnets was applied in order to accomplish a magnetic induction of approximately two Tesla (20,000 gauss) around the specimen although the sample geometries were not always the same. Furthermore, each set of magnets was electrically isolated with an epoxy coating few days prior to setting up the apparatus in order to prevent current leaks during the experiments.

Because the LECO Hydrogen Determinator RH-404, device used to determine hydrogen concentration after charging, limits the weight and dimension of the steel samples to approximately 1 gram and 7.5 mm (0.295 in) diameter by 18 mm (0.708 in) length, the steel hydrogen charging sample were very small. To machine these small specimens employing a conventional cut off machine and a precision diamond saw commonly used in metallographic laboratories became an issue. Even though the purpose of sectioning the samples perfectly identical was always present, the final result revealed specimens with unequal dimensions. This situation is the reason why the magnetic flux density around the steel samples had to be measured and monitored continuously.

The steel pipe sample of Grade X70 is 9/32 in (0.67 cm) thick, while the steel pipe sample of Grade X80 is 5/8 in (1.53 cm) thick. All charging specimen of steel pipe Grade X70 was 0.281 in (0.69 cm) thick. To present a comparison evaluation under the same external magnetic field, all pipe Grade X80 specimens sectioned from the pipe sample were cut into two pieces. That is, each charging specimen was approximately 0.31 in (7.6 cm) thick.

The plotted results indicate that a strong and continuous magnetic field caused a tremendous effect on absorbed hydrogen concentration in high-strength pipeline steels. After reaching the saturation level or equilibrium point (plateau), the absorbed hydrogen concentration

in the pipeline steel of Grade X52 under a two-Tesla (20,000 Gauss) magnetic induction was 6.1 times the concentration under cathodic charging conditions without an applied magnetic field (see Figure 6.5). The absorbed hydrogen concentration in the magnetized steels of Grades X70 and X80 were 2.6 and 1.6 times the hydrogen content under non-magnetization conditions (see Figures 6.6 and 6.7). According to Figures 6.15-6.18, the saturation magnetic flux density points or equilibrium hydrogen content in pipeline steels of Grades X52, X70, and X80 were reached approximately after four (4), two (2), and one (1) hour of cathodic charging in 1N sulfuric acid, respectively.

Correlating Equation (4.8) with the plotted results in Figure 6.5, the equilibrium point of absorbed hydrogen concentration under initial experimental conditions (without magnetization, B=0) is represented by $[H]_{B=0}$, i.e. the natural logarithm at magnetic flux density of zero ($\ln[H]_{B=0}$). This point is reached at plateau level; that is, $[H]_{B=0}$=1.29 ppm where $\ln[H]_{B=0}$= 0.2231. On the other hand, the plateau level of the magnetic flux density curve represents the absorbed hydrogen concentration at the specific magnetic induction of two Tesla (20,000 Gauss) and charging time and current density. For example, at $[H]_{B=2T}$ =7.9 ppm, Equation [8] from Section 4 for steel of Grade X52 becomes

$$\ln[7.9\,ppm] = \ln[1.29\,ppm] + \left[\frac{\Delta M}{RT}\right] * 20{,}000G \qquad (6.3)$$

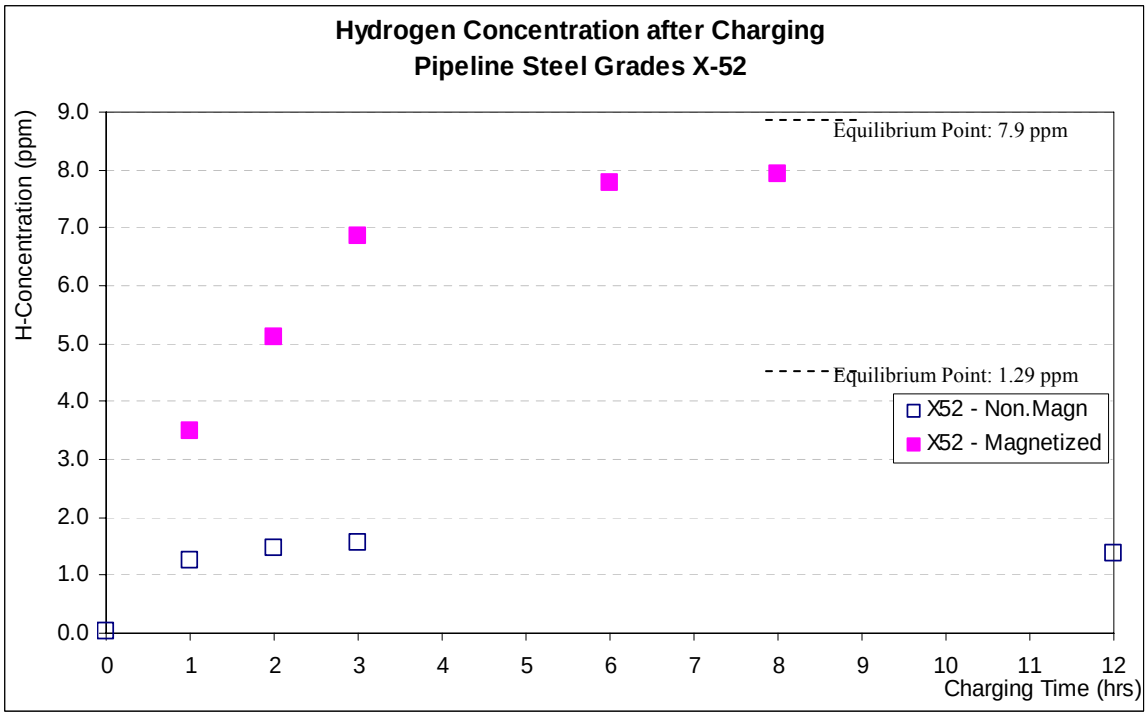

Figure 6.5. Absorbed hydrogen concentration in pipeline steel of Grade X52 at different cathodic charging times. It shows for comparison the experimental results without magnetization and under a two Tesla (20,000 Gauss) magnetic induction (indicated as "X52 – Magnetized"). The equilibrium points or saturation levels (plateau) are indicated.

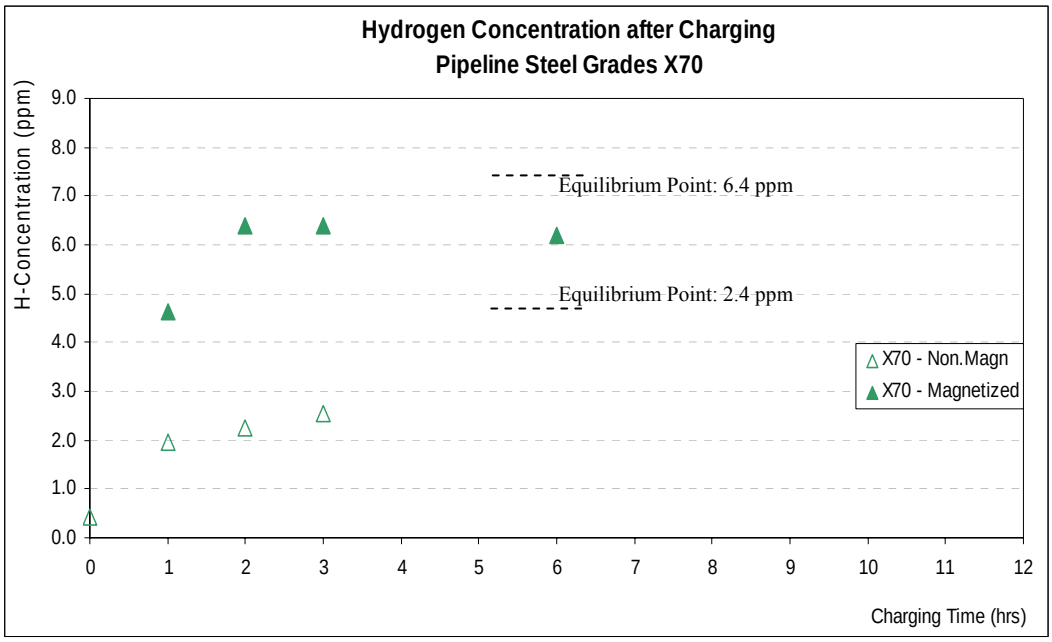

Figure 6.6. Absorbed hydrogen concentration in pipeline steel of Grade X70 at different cathodic charging times. It shows for comparison the experimental results without magnetization and under a two Tesla (20,000 Gauss) magnetic induction (indicated as "X70 – Magnetized"). The equilibrium points or saturation levels (plateau) are indicated.

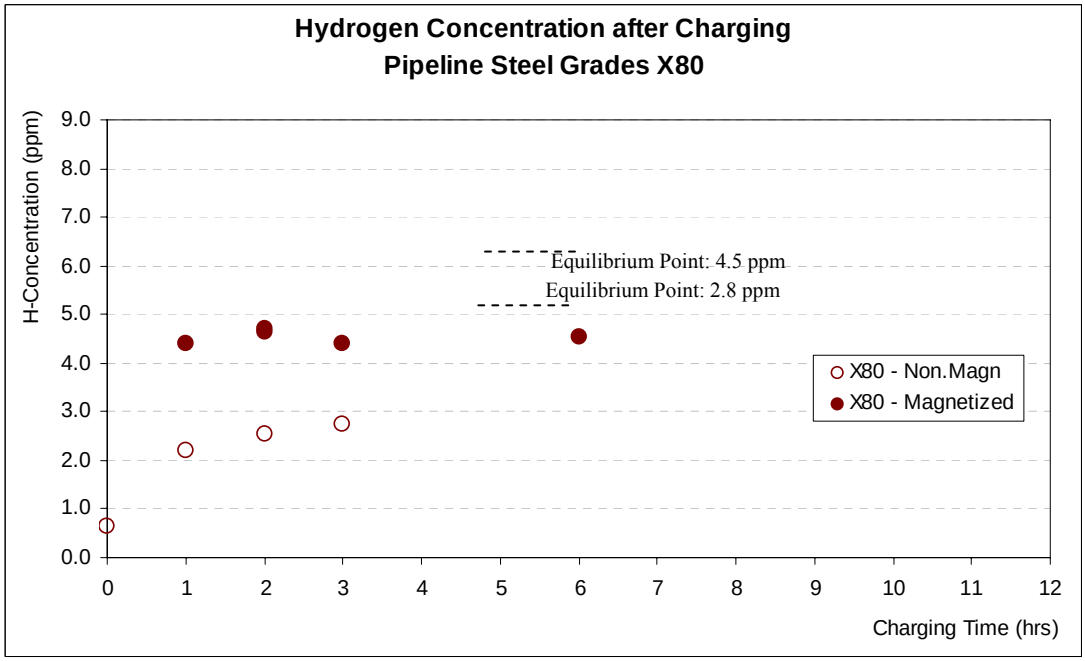

Figure 6.7. Absorbed hydrogen concentration in pipeline steel of Grade X80 at different cathodic charging times. It shows for comparison the experimental results without magnetization and under a two Tesla (20,000 Gauss) magnetic induction (indicated as "X80 – Magnetized"). The equilibrium points or saturation levels (plateau) are indicated.

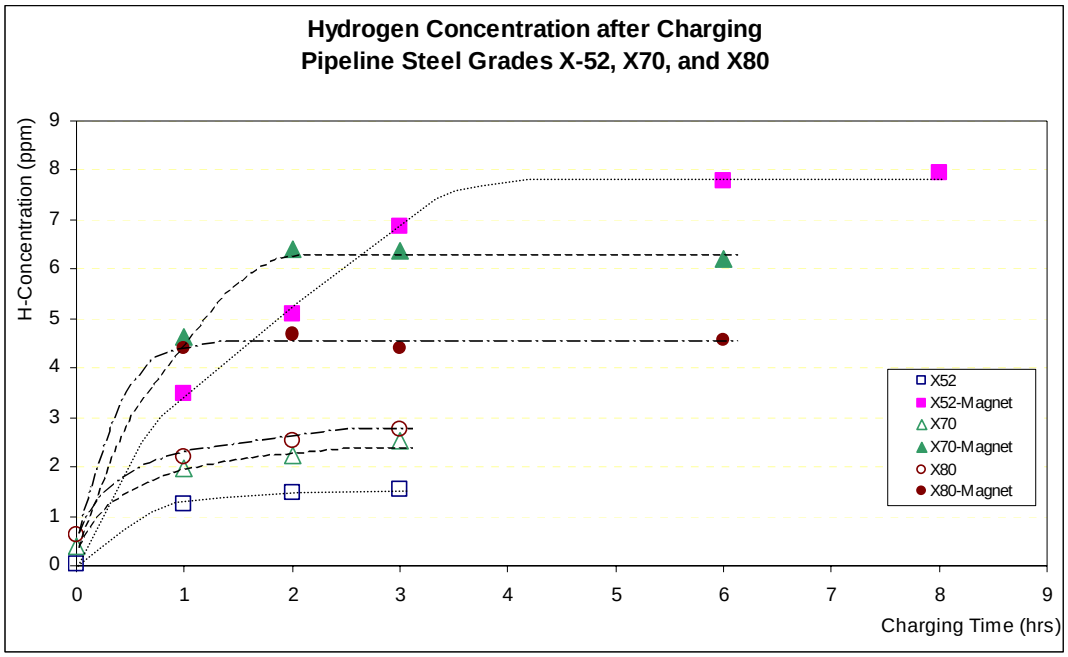

Figure 6.8. Comparison plot of the absorbed hydrogen concentration in pipeline steels of Grades X52, X70, and X80 at different cathodic charging times.

The slope of this straight line, $\Delta M/RT$, is a property of the assessed pipeline steel under the experimental conditions and is related to the magnetic permeability of the material. Different pipeline steels generate different straight-line slopes because they have diverse strength levels and microstructures. It is commonly expected that the magnetic properties of pipeline steels will vary with pipe grade.

Figure 6.8 illustrates the graphical expression of the experiment using the experimental data from Table 6.1. The $[H]/[H]_{B=0}$ ratios equal 6.1, 2.7, and 1.6, for steels of Grades X52, X70, and X80, respectively, leading to the following statement:

"A magnetic induction of 20,000G and 0.05 A/cm^2 current density can increase more than six times the absorbed hydrogen concentration of pipeline steels."

A question to be addressed is: how much is the absorbed hydrogen content increase under the remanent magnetization left by the Magnetic Flux Leakage tool after inspection operations? This fundamental question can be addressed by the analysis of the in-between points in Chapter Seven.

6.3 Magnetization Effect on Hydrogen Concentration in Coldworked Steel Samples

To assess the effect of high magnetic flux density on hydrogen intake in cold-worked high strength steels, conventional specimens (similar to those used in Section 6.2) were sectioned from cold-worked steels of Grades X70 and X80 samples and then charged using the previously

described hydrogen cathodic charging cell. The results are plotted in terms of total absorbed hydrogen content as a function of bending angles (level of residual stresses).

Table 6.1. Experimental data from Figure 18 at Magnetic Flux Density of 20,000Gauss.

Parameter	Steel X52		Steel X70		Steel X80	
	Without Magnetization	Magnetization	Without Magnetization	Magnetization	Without Magnetization	Magnetization
Equilibrium Hydrogen Concentration **[H]** (ppm)	1.250	7.900	2.100	6.500	2.800	4.500
Ln [H]	0.223	2.067	0.742	1.872	1.030	1.504
[H] / $[H]_{B=0}$ Ratio	6.3		3.1		1.6	
ΔM/RT	---	0.0001	---	0.00005	---	0.00002

A better understanding of the obtained results is possible if a brief description of the bending-angle effect on the specimens' microstructure is discussed. Cold-work produces a considerable increase in the number of dislocations, which results in a higher state of internal stress or residual stress due to the interaction of those dislocations. In terms of steel microstructure, cold-work highly elongates grains in the working direction and increases the number of precipitation sites. Severely deformed materials develop a preferred orientation (known as fiber texture) which causes anisotropy in mechanical properties. The development of texture always accompanies the formation of deformation bands (region of distortion where portion of grains rotate towards another orientation) and shear bands (distortion regions extended across many grains).

Bending is a forming process by which a straight length is transformed into a curved length (see Figure 6.9). During bending, the plastic strain is proportional to the distance from the neutral axis, which remains at the center fiber if the change in thickness is neglected. Fibers on the outer surface are stretched and fibers on the inner surface are compressed. The strain increases with decreasing radius of curvature, and for a given bending operation, the bending curvature cannot be larger than a certain value, otherwise the material will crack. Radius of curvature in a 60º bending specimen is smaller than this in a 120º bending specimen.

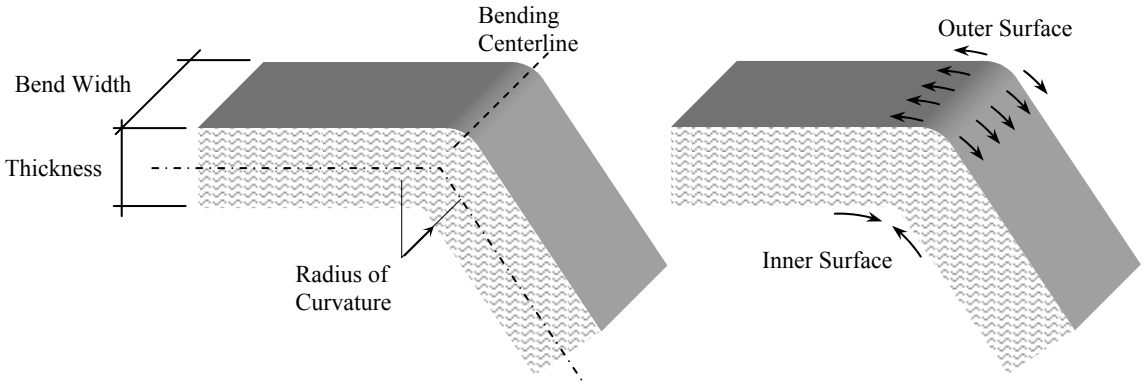

Figure 6.9. Straight length transformed into a curved length due to bending process. Notice that the fibers on the outer and inner surface are strained and contracted, respectively.

Figure 6.10 shows the three tested bending angles applied to the evaluated pipeline steels of Grades X70 and X80. It is quite remarkable that the manufacturing process of line pipe includes 'pipe forming by rollers.' That is, a straight steel sheet has been transformed into a curved pipe. Consequently, the bending process is not quite as simple as it is shown in Figure 6.9. Figure 6.11 shows how a pipe specimen is cut off from the tube and then bent to obtained the bending specimens used in this study. Notice that the strain distribution is more complex.

To illustrate how cold-work highly elongates grains in the working direction, several microphotography from outer and inner surfaces as well as the mid-thickness surface are shown in Figures 6.12-6.14. Notice that outer and inner surfaces exhibit elongated grains in the working direction. It is quite remarkable that the microstructures illustrated in Chapter Five for both steels of Grades X70 and X80 are the same for the 180º bending specimen.

The effect of high magnetic flux density of 2 Tesla (20,000 Gauss) on hydrogen content in cold-worked high strength steels of Grades X70 and X80 using the hydrogen cathodic charging cell is shown in Figures 6.15 and 6.16. Results are plotted in terms of total absorbed hydrogen content as a function of bending angles (level of residual stresses). Because the saturation magnetic flux density points or equilibrium hydrogen content in pipeline steels of Grades X70 and X80 are reached approximately after two (2) and one (1) hour of cathodic charging in 1N H_2SO_4 (sulfuric acid), respectively, the cold-work test charging time was setup at three (3) hours. Therefore, all bending specimens were tested at 2 Tesla for 3 hours in 500 ml of fresh 1N H_2SO_4 solution.

The results shown in Figures 6.15 and 6.16 are analyzed in Chapter Seven. However, it is quite remarkable that the results are largely different from what was expected. The graphical representation of the expected results is shown in Figure 5.28, where it is assumed that results follow a particular trend. In contrast, the experimental results exhibit a range of values that should be viewed as a zone of results. The reason for these results could be associated with the strain distribution throughout the tested specimen wall-thickness. Notice that the charging specimens were cut off from bent samples using a precision diamond saw, which does not guaranty that specimens are dimensionally equal and have identical strain distribution.

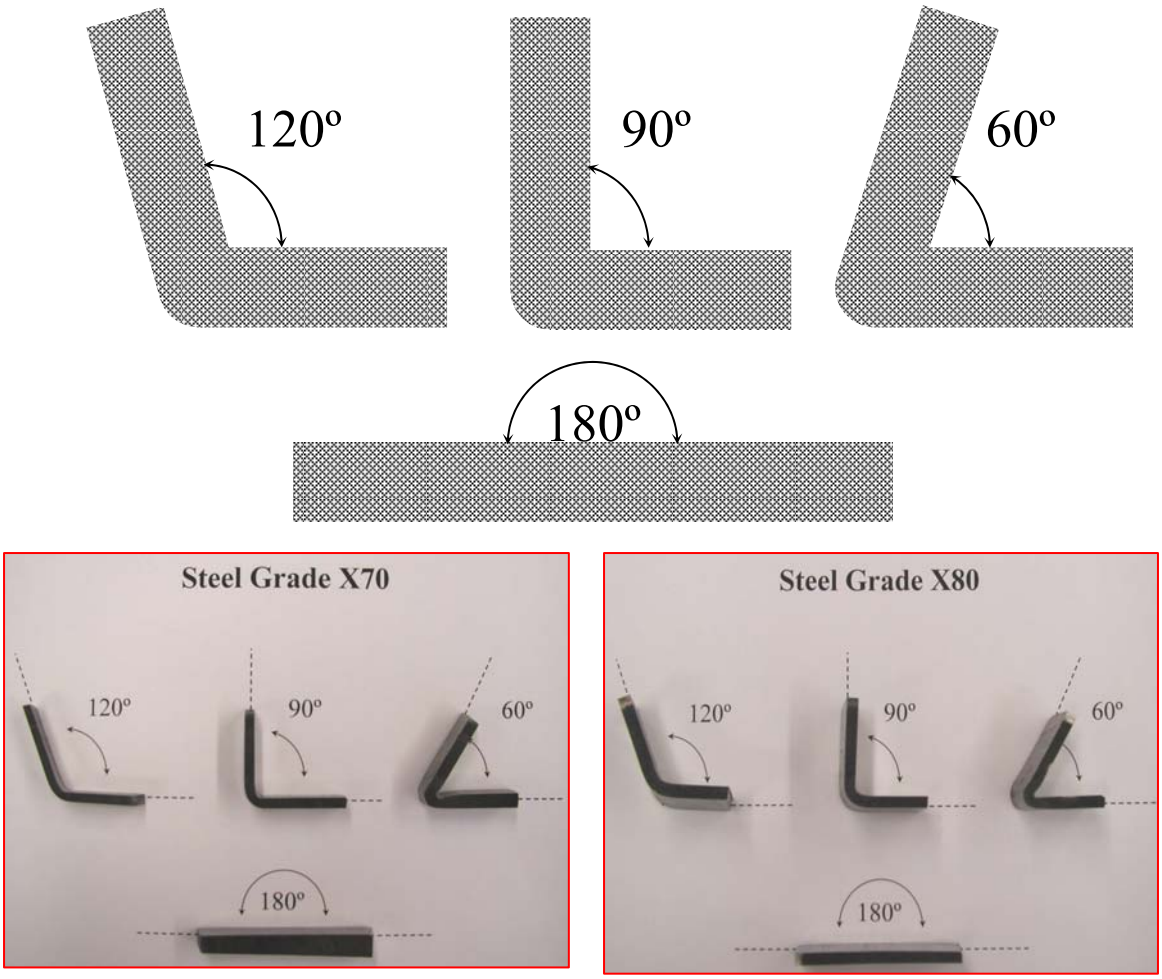

Figure 6.10. Bending angles – 180º, 120º, 90º, and 60º – applied to the evaluated pipeline steels of Grades X70 (3/8 in wall-thickness) and X80 (3/4 in wall-thickness).

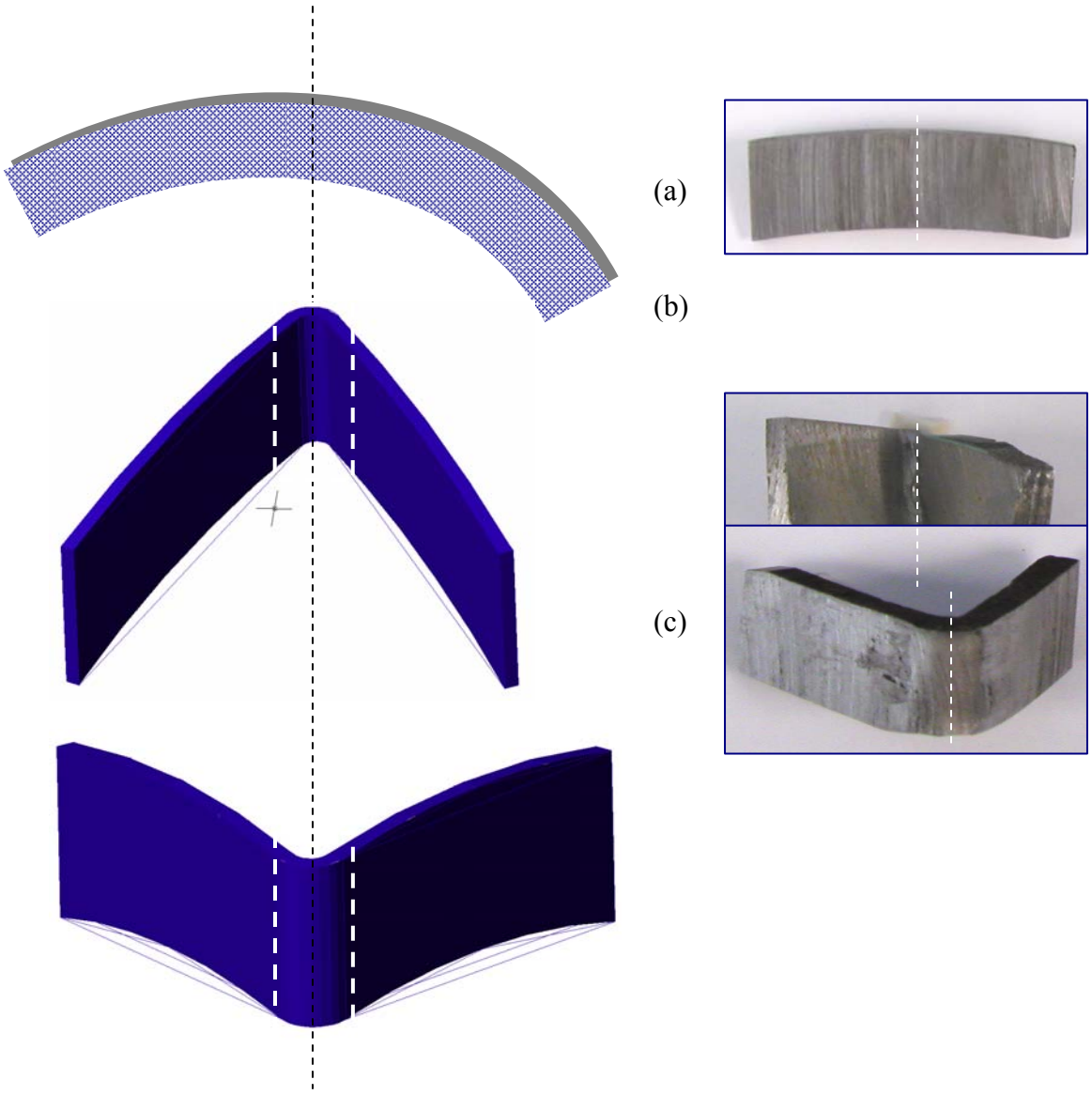

Figure 6.11. Representation of the tested line pipe sample (a) cut off from the tube showing a concave-arc configuration as result of the 'pipe forming process'. 60º bending specimen where concave arc is revealed (b-c). White segmented lines indicate high stresses section where from bending specimens for cold-work test are obtained.

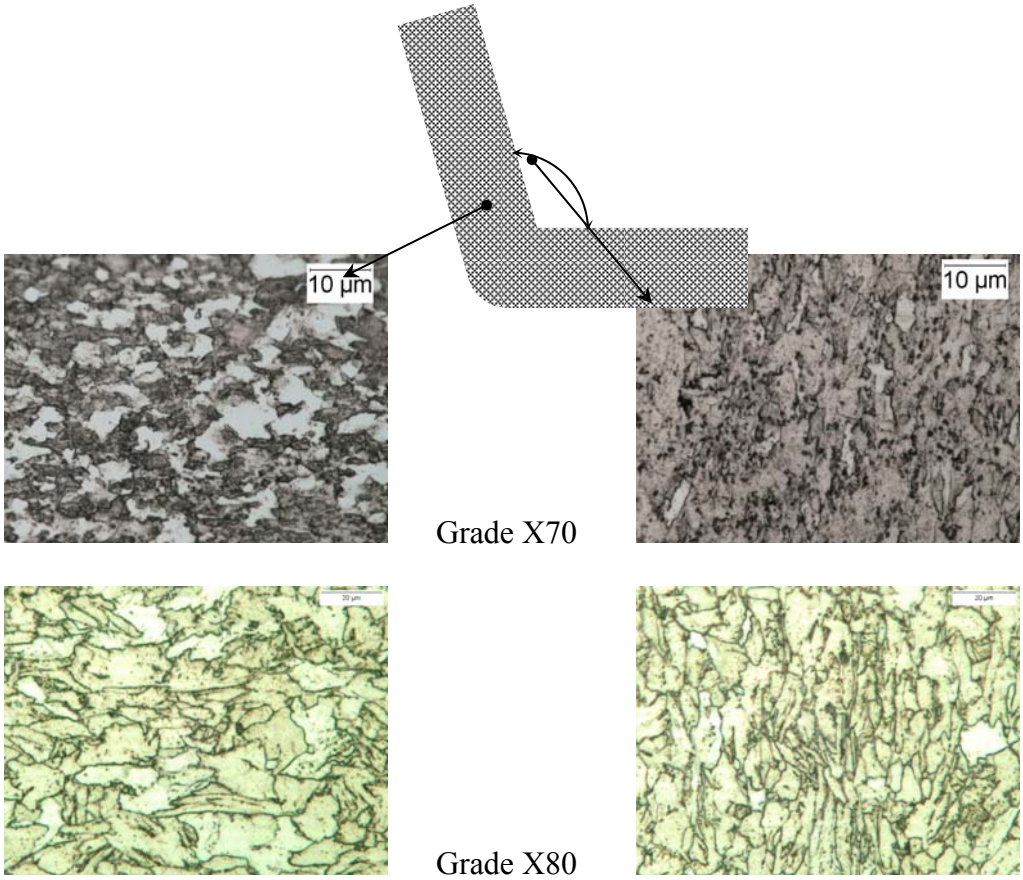

Figure 6.12 Microphotography of 120º bending specimen illustrating the elongation of grains on the outer and inner surface in the working direction.

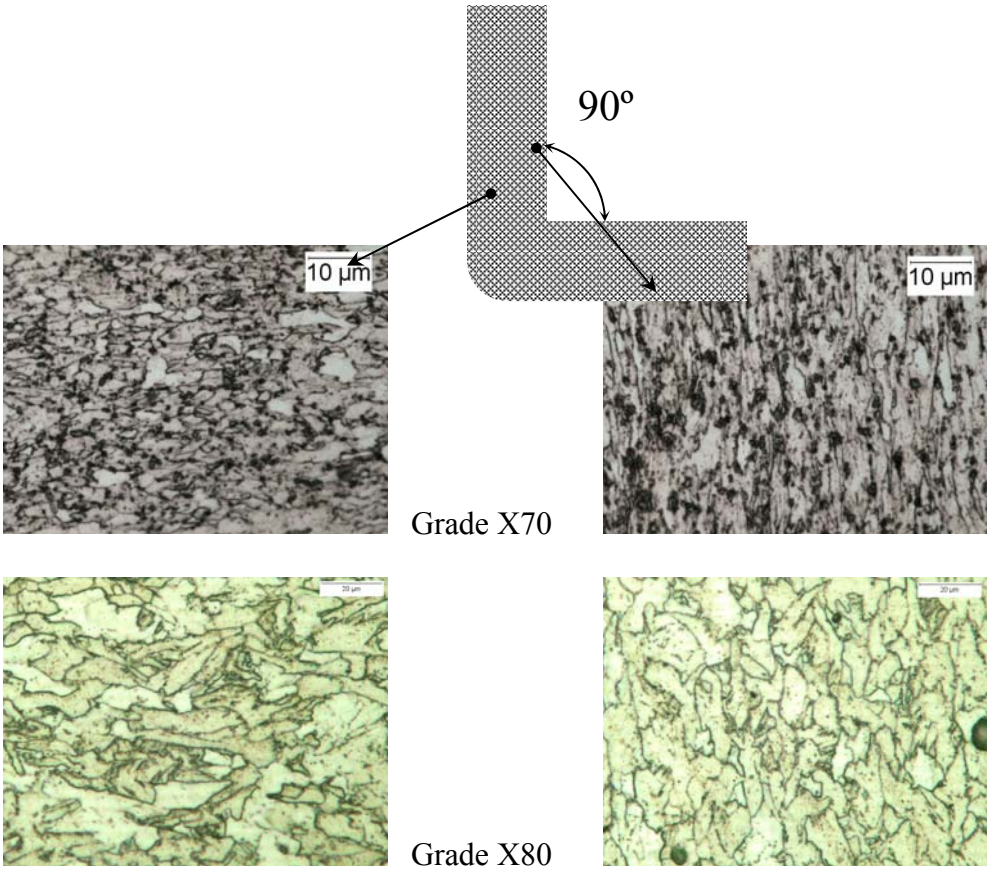

Figure 6.13 Microphotography of 90º bending specimen illustrating the elongation of grains on the outer and inner surface in the working direction.

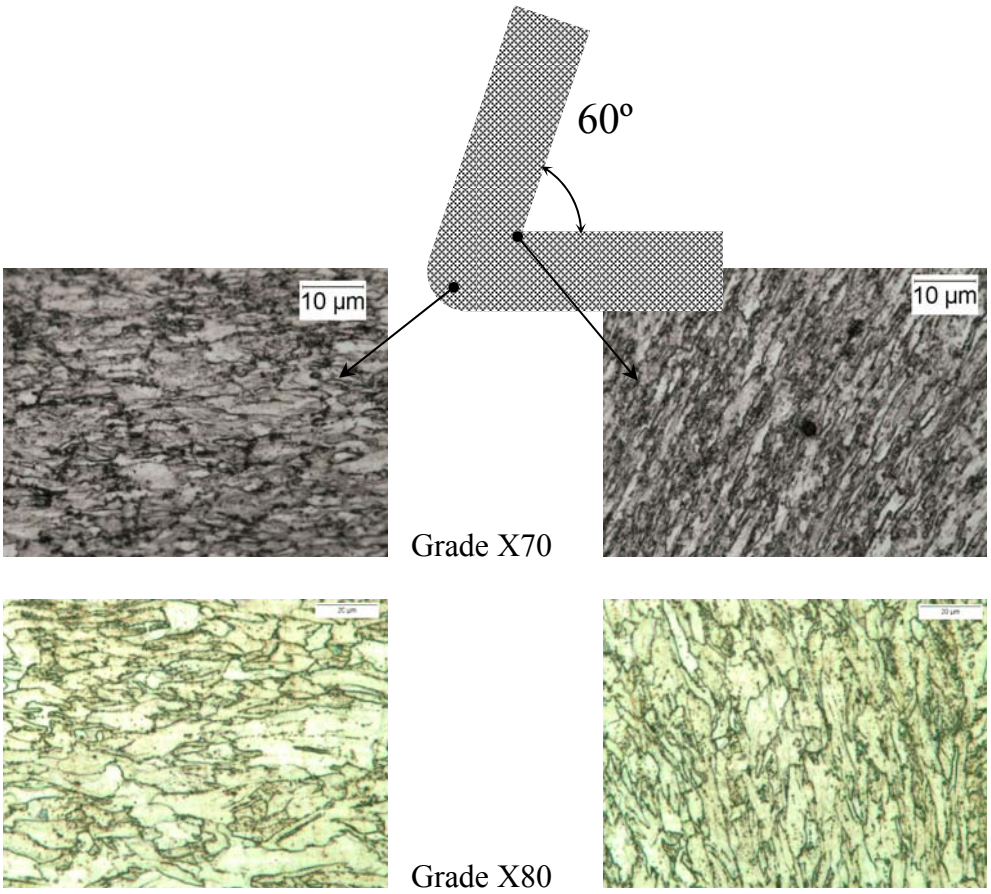

Figure 6.14 Microphotography of 60º bending specimen illustrating the elongation of grains on the outer and inner surface in the working direction. This case represents the most severe bending specimen.

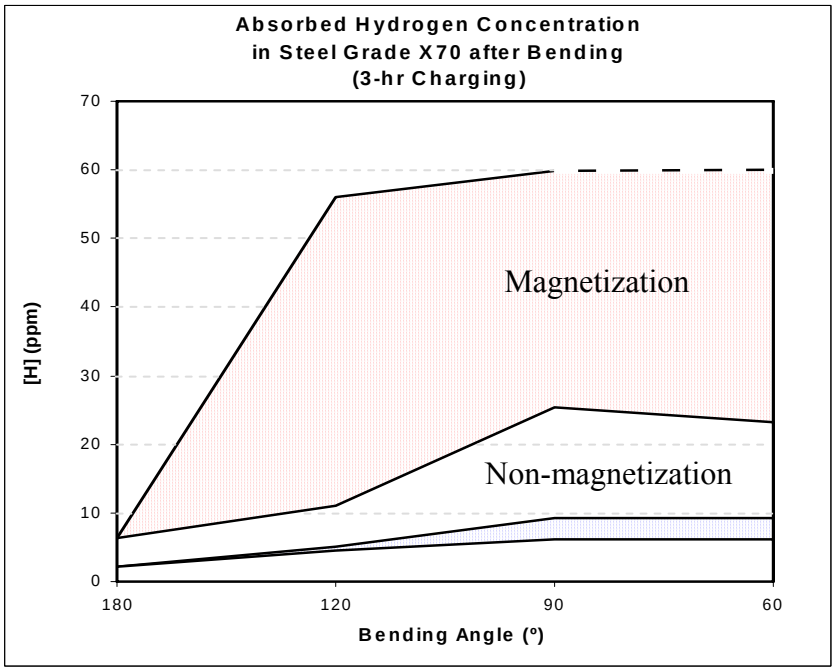

Figure 6.15 Graphical representation of the effect of high magnetic flux density, 2 Tesla, on total absorbed hydrogen concentration in cold-worked high strength steel of Grade X70.

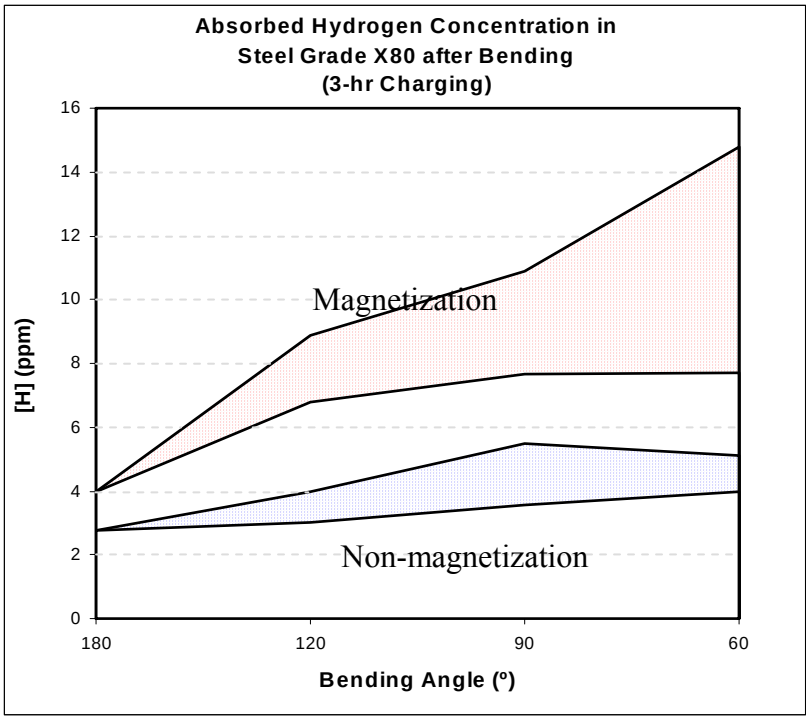

Figure 6.16. Graphical representation of the effect of high magnetic flux density, 2 Tesla, on total absorbed hydrogen concentration in cold-worked high strength steel of Grade X80.

6.4 Magnetization Effect on Hydrogen Induced Cracking for Thick High Strength Pipeline Steels

Hydrogen damage or hydrogen embrittlement is a form of environmentally induced cracking that generally occurs as a result of the combined action of hydrogen and residual or applied stresses. Hydrogen induced cracking, a type of hydrogen damage, is characterized by the brittle fracture of a typically ductile alloy under sustained loads (generally lower than the yield strength of the alloy) in the existence of hydrogen. This cracking phenomenon depends primarily on the hydrogen fugacity, applied or residual stresses, strength level of the material, heat treatment/microstructure, and temperature. Hydrogen stress cracking produces sharp singular cracks and is associated with the absorption of hydrogen and a delayed time to failure called incubation time. It has been demonstrated that at very high corroding potentials the fracture path may be transgranular occurring by the combination of hydrogen embrittlement and metal dissolution.

It is understood that the purpose of this study is neither the discovery of a new hydrogen damage mechanism nor the experimental support of one already suggested by investigators. However, as a matter of fact, few suggested mechanisms have been included and analyzed in order to comprehend the phenomenon.

Based on the hydrogen pressure theory, the embrittlement is caused by the diffusion of atomic hydrogen into the metal and its accumulation in high triaxial tensile stress zones or in some microstructural configurations where they become trapped such as dislocations or metallurgical defects (i.e. micro-voids and second-phase interfaces). A high concentration of hydrogen at these microstructural in-homogeneities causes a large internal pressure that enhances micro-void growth and crack initiation. Dislocations transport or motion from cold-work, for instance, can also create high internal pressure in the micro-voids. Based on the de-cohesion theory, the dissolved hydrogen may also effect the bond strength between atoms of the alloy matrix making the normal maximum tensile stress perpendicular to the crack plane equal to or higher than the lattice bond strength causing fracture.

Although the hydrogen pressure and de-cohesion theories may not be the only two hydrogen damage mechanisms existing to explain the obtained results, they are the more precise. This assumption is based on microphotographic evidence and literature references.

It is know that high-strength steels commonly show an incubation time before fracture initiates under sustained (applied or residual) loading. Tensile residual stresses such as those produced on the outer surface of bent (cold-work) samples, may also promote the initiation of hydrogen stress cracking.

It is quite remarkable that hydrogen-induced cracking in pipeline steels normally takes a form of hydrogen-induced blister cracking (HIBC). This particular mechanism induced by hydrogen atoms trapped at interfaces between matrix and inclusions offers low resistance to hydrogen embrittlement. Hydrogen trapped at elongated inclusions (principally MnS) is responsible for hydrogen-induced cracking due to either internal pressure or decohesion of the inclusion-matrix interface. As soon as hydrogen is trapped at an inclusion, it may achieve a high

internal pressure reducing the interatomic cohesive forces and surface energy at the inclusion surface and affecting, as well, the dislocation motion in the plastic zone.

Even though a fine ferrite-pearlite structure (normalizing) had been considered as structure that reduces hydrogen-induced cracking susceptibility in pipeline steel of Grades up to X60, some studies have revealed that this microstructure possesses the least hydrogen embrittlement (specifically sulfide stress cracking) resistance. It is because carbides and MnS inclusions precipitate along the banded pearlite and hydrogen diffusions to their interfaces reach the critical hydrogen concentration quickly.

To simulate experimental conditions of standard hydrogen damage tests and achieve the comparison evaluation defined as the primary purpose of this section, a set of 60º-bending steel of Grades X70 and X80 samples were obtained. Figure 17 exhibits the external highly stressed surface of a 60º-bended pipeline steel of Grade X70 sample. No cracks resulted from high-angle bending methods are observed. The tested pipeline steel sample wais 9/32 inches (0.67 mm) thick and the exposure area is approximately 0.093 in^2 (0.6 cm^2). Figure 6.18 shows the exposure area of a steel of Grade X80 HIC specimen where no cracks due to bending were observed. The specimens from steel of Grade X80 were approximately 0.31 in (0.76 cm) thick, which was half of the original pipe wall thickness (5/8 in, 1.53 cm). Figure 6.19 exhibits microphotographic evidence of deformation bands as a result of high-stress bending loads (cold-work) applied in the external surface of the steel of Grade X80 specimen. The propagation of these shear bands was in the direction of tensile stresses due to bending loads; i.e., the outer fibers. These bands are related to dislocations, which represent structural anomalies where hydrogen is commonly trapped.

Table 6.2 displays the experimental results obtained from the hydrogen-induced cracking evaluation. The test was conducted using pipeline steel of Grades X70 and X80 specimens submerged in the cathodic solution for 12, 24, and 36 hours under no magnetic field described as ‘Non-Magnet’ and under approximately 2 Tesla (20,000 Gauss) of magnetic induction described as ‘Magnet.’ The pit density (pitting) was measured in terms of the following classification: Heavy, Moderate, Minor, and No (i.e. pits do not exist). The presence of cracks in the exposure areas was presented in terms of ‘Yes’ and ‘No.’ This comparison evaluation points out the effect of magnetization on the nucleation and propagation of cracks in the tested pipeline steels under laboratory conditions (hydrogen-bearing solution, 1N H_2SO_4).

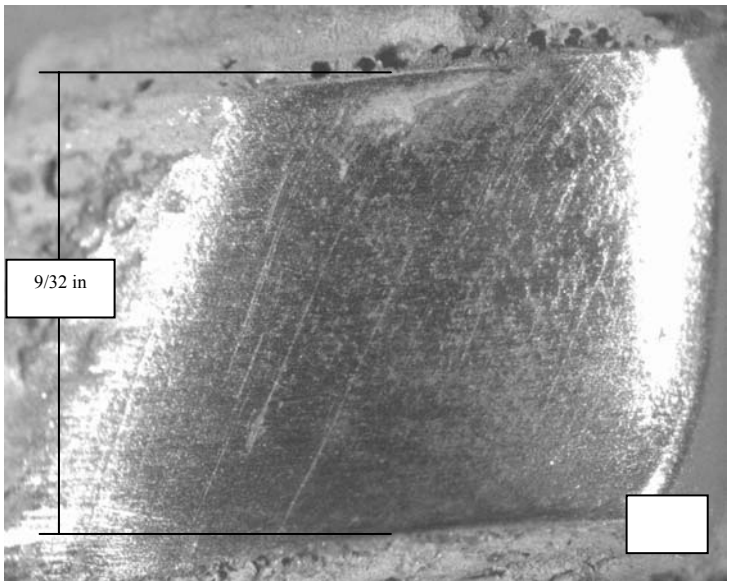

Figure 6.17. 60º-bended steel of Grade X70 sample, 9/32 in (0.67 cm) thick, just after bending and before cathodic charging. Notice that there are no evidence of pits or mechanical damage due to bending loads (such as bending-cracks).

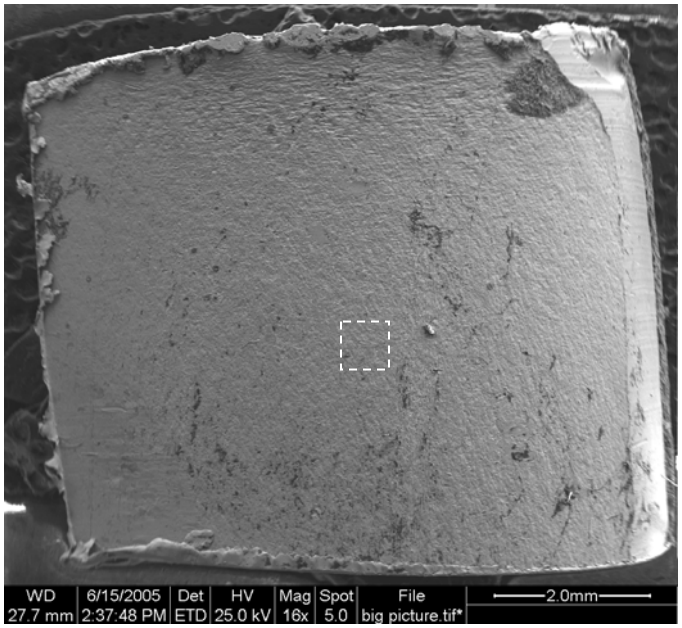

Figure 6.18. 60º-bended steel of Grade X80 sample, 5/8 in (1.53 cm) thick, just after bending and before cathodic charging. No evidence of bending-cracks or pits are observed. The white square shows the section observed in Figure 6.19.

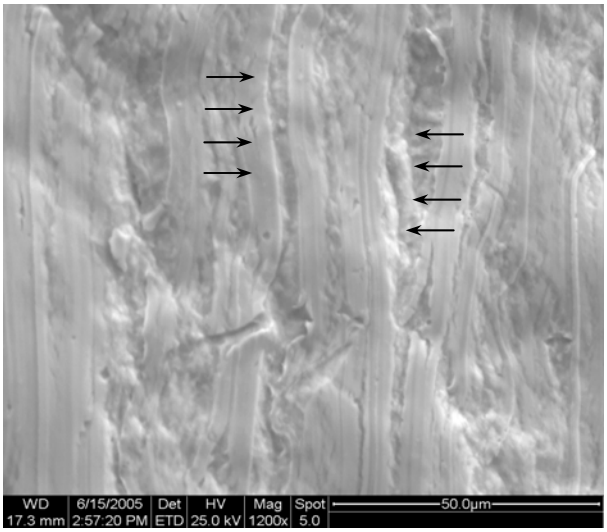

Figure 6.19. External surface of bending sample Grade X80 where deformation bands (arrows) due to cold-work are exhibited. These shear bands are perpendicular to the applied tensile stress direction.

Table 6.2. Hydrogen-induced cracking results for comparison and evaluation.

Charging Time (hours)	**Pipeline Steel Grade X70**				**Pipeline Steel Grade X80**			
	Pitting		Cracks		Pitting		Cracks	
	Non-Magnet.	Magnet.	Non-Magnet.	Magnet.	Non-Magnet.	Magnet.	Non-Magnet.	Magnet.
12	Minor	Moderate	No	Yes	n/t	No	n/t	No
24	Minor	Heavy	No	Yes	No	Minor	No	Yes
36	n/t		n/t		Minor	Heavy	No	Yes

n/t: no tested because it was considered non-relevant in terms of test purposes.

Notice that the HIC test reveals that a strong, continuous magnetic field causes a significant effect on both formation of pits and nucleation and propagation of cracks. Pits represent high-stress concentration points where cracks may initiate.

6.4.1 Pipeline Steel of Grade X70

After charging with hydrogen for 12 hrs, the pipeline steel of Grade X70 showed minor concentration of pits under non-magnetizing conditions and moderate-to-heavy concentration of pits and cracks in the exposure surface under magnetizing conditions (see Figures 6.20 and 6.21). The sample exhibited in Figure 6.21 was the first tested HIC specimen where SEM evaluation was not included; however, the rest of the specimens were evaluated employing SEM microscope. Because the very localized concentration of pits, a transversal-section optical evaluation was conducted and no microphotographic evidences of pits were found.

After 24 hours charging with no magnetization a minor concentration of pits and no cracks were observed. However, a group of non-metallic inclusions were revealed during the fractographic analysis of the external, exposure area. These inclusions are preferentially aligned next to pits given the idea that they are closely connected. Even though there are several small pits nearby a big cavity, cracks were observed neither inside nor outside of the pits (see Figure 6.22). Because pits are considered crack-initiation points, it is quite relevant to state that cracks would be present after few more hours charging.

Figure 6.23 shows a specimen exposed to the charging solution for 24 hours under magnetizing conditions. This 9/32 in (0.69 cm) thick specimen exhibits a heavy concentration of pits in a preferential zone, which could be localized in the maximum tensile stress area (Figures 6.9 and 6.10). Figure 6.24 magnifies the observed section in Figure 6.23, which shows a heavy concentration of small and large pits at 1500x. Cracks are observed inside a large pit and next to a non-metallic inclusion at 2500x. Inclusions are also considered crack-initiation points and, in this case, acted as a point of initiation of several microcracks.

Figure 6.25 shows that the pits and cracks exhibited in Figures 6.22 and 6.23 are closely connected to non-metallic inclusions. A metallographic evaluation revealed that the heavy concentration of pits in the outer surface is caused by the high accumulation of aligned non-metallic inclusions in the material. The larger and deeper pits are observed at the end of long lines of accumulated inclusions, while smaller and shallower pits are placed at the surface where the internal concentration of inclusions is lower. The initiation points of cracks are located at the bottom of the deeper pits as is shown in Figure 6.26. These high magnification microphotograpy analyses confirm the fact that the cracking path follows the zone with the maximum accumulation of inclusions.

Because pits have been discovered in the HIC specimens after 24 hours charging under no magnetization conditions, the 36 hours experiment was not conducted. 24 hours of cathodic charging employing an experimental solution of 1N H2SO4 at a current rate of 0.05 A/cm^2 is enough to produce pits in the tested pipeline steel of Grade X70.

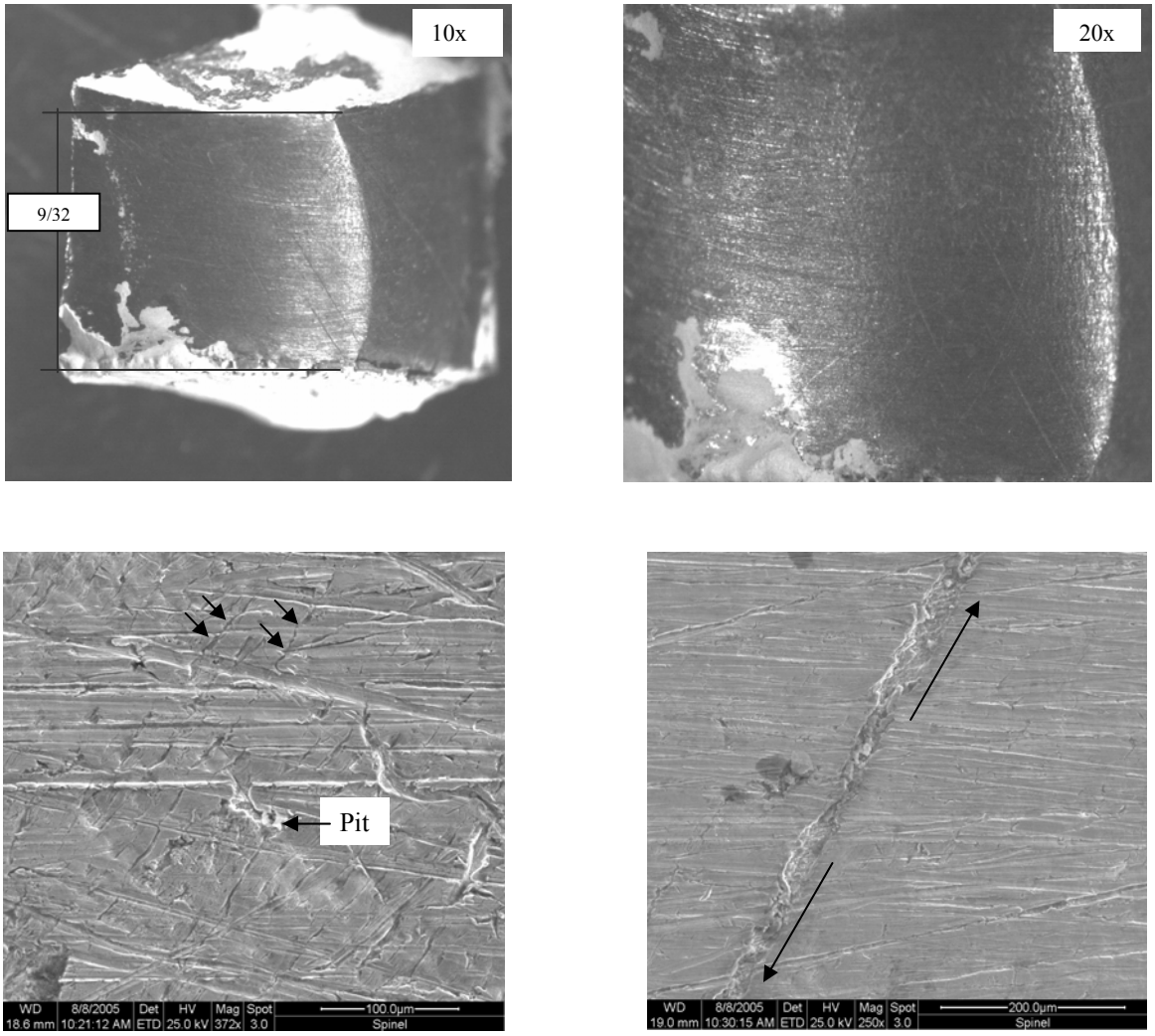

Figure 6.20. Pipeline steel sample Grade X70 after 12 hrs charging under non-magnetizing conditions (a). Notice that there are no pits at low magnification (b) and at higher magnification a very small (minor) concentration of pits is detected with no cracks (c-d). Figure (c) shows a very small pit and several indications of dislocations, while Figure (d) shows a pit growth following an inclusion path.

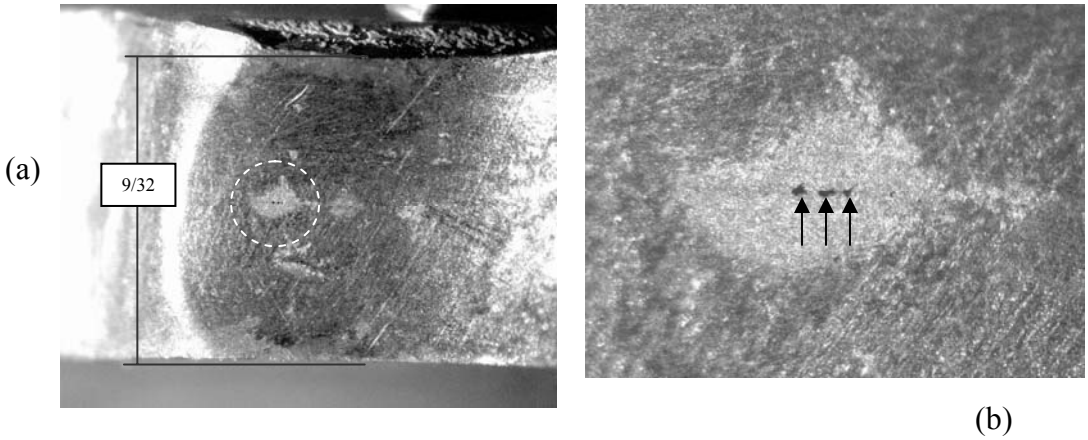

Figure 6.21. Pipeline steel sample Grade X70 after 12 hrs charging under magnetizing conditions (a). Notice that there is a very low (minor) concentration of pits and they are distributed following a preferential alignment where a crack was formed (b). Figure (b) zooms in the white circle area indicated in (a).

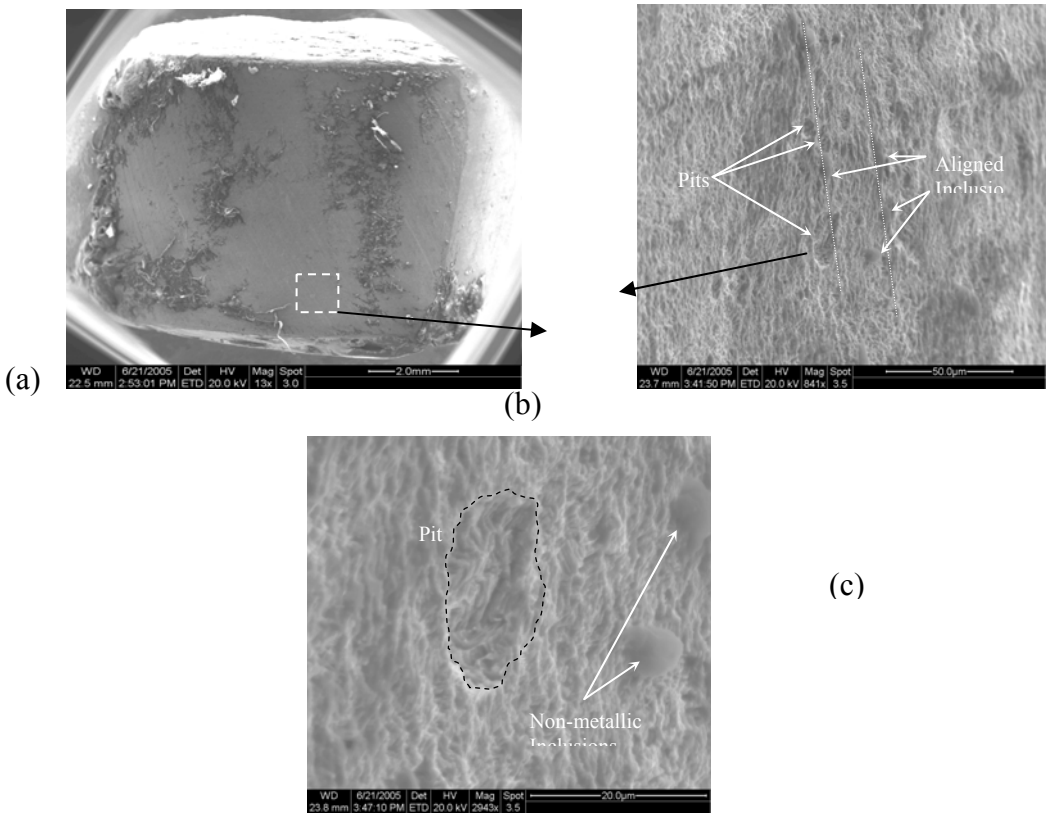

Figure 6.22. Pipeline steel sample Grade X70 after 24 hrs charging under non-magnetizing conditions (a). Notice that there is a minor concentration of pits (b) next to a preferential aligned group of non-metallic inclusions. No cracks are observed (c) although small pits are nearby a big one.

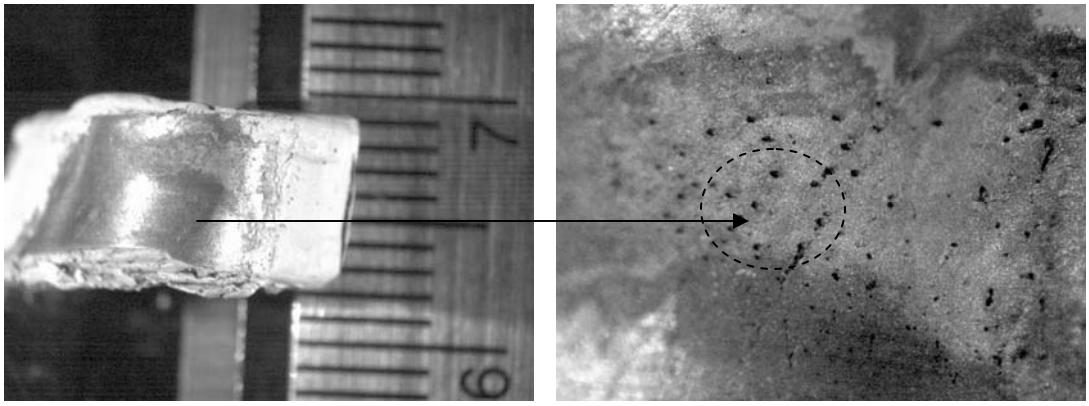

(a) (b)

Figure 6.23. Pipeline steel sample Grade X70 after 24 hrs charging under magnetizing conditions (a). Notice that there is a heavy concentration of pits (b) in the external surface where probably the maximum tensile stresses due to bending are present. Several of these pits are preferentially aligned producing cracks (arrows).

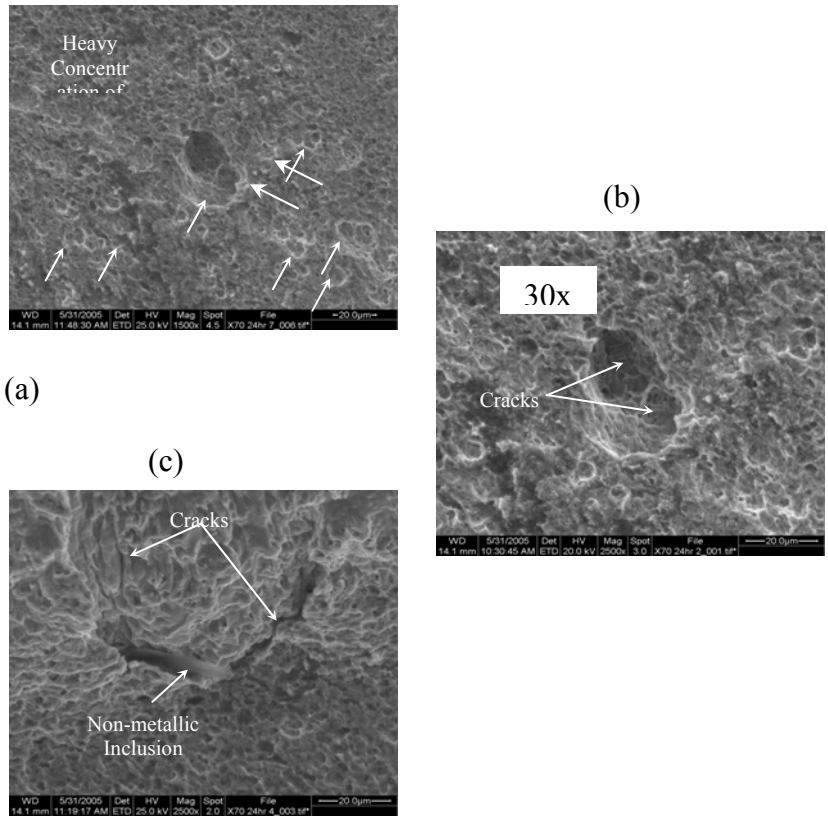

Figure 6.24. Pipeline steel sample Grade X70 exhibited in Figure 33. Notice the heavy concentration of pits (a) and the presence of cracks inside one of these pits (b). Nearby, a non-metallic inclusion acted as a crack-initiation point (c).

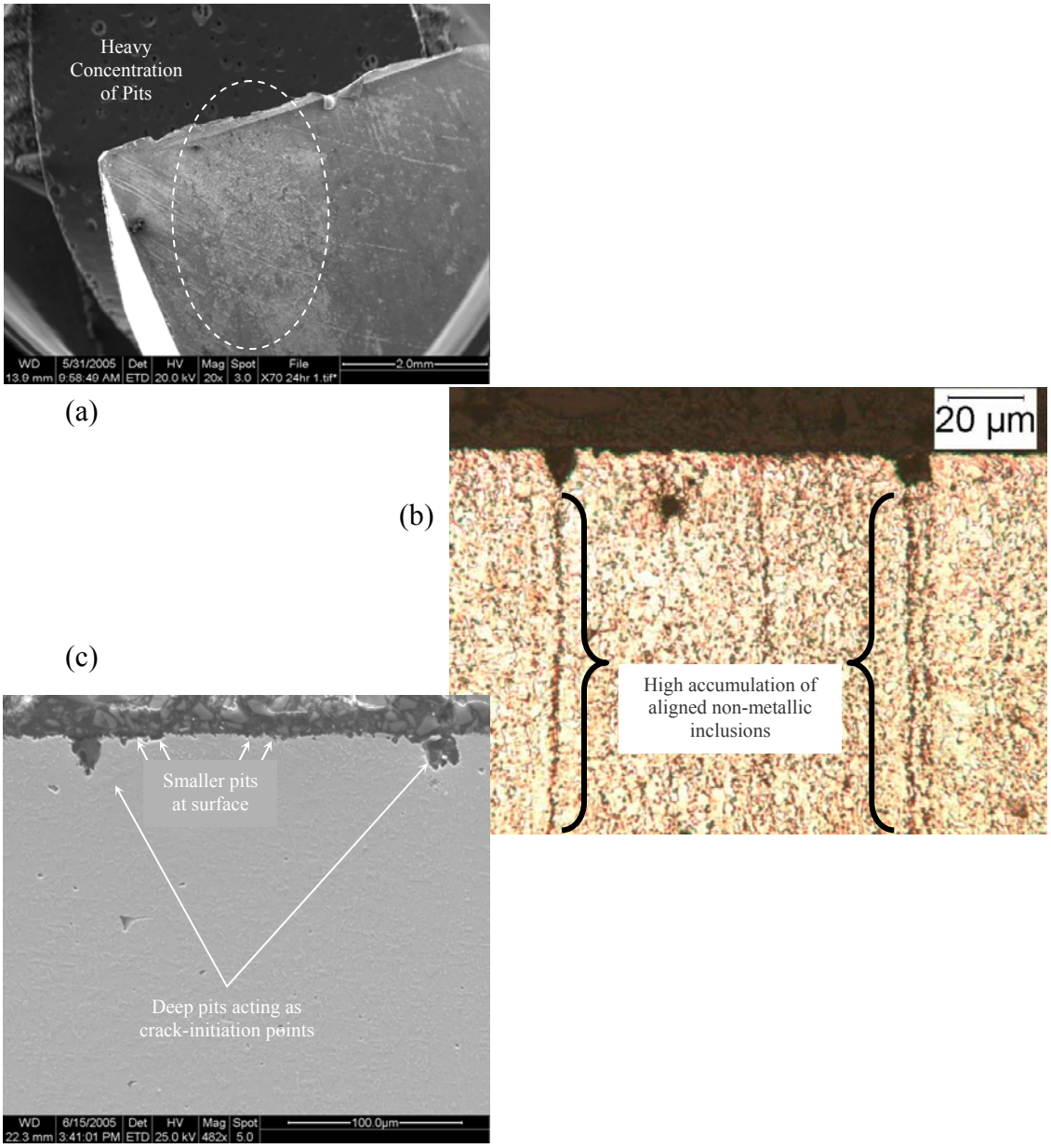

Figure 6.25. Pipeline steel sample Grade X70 exhibited in Figure 6.33-a. Notice the heavy concentration of pits (a) in the sectioned sample. The high accumulation of aligned non-metallic inclusions in the material (b) causes formation of pits at the surface, which act as crack-initiation points (c). See Figure 6.36.

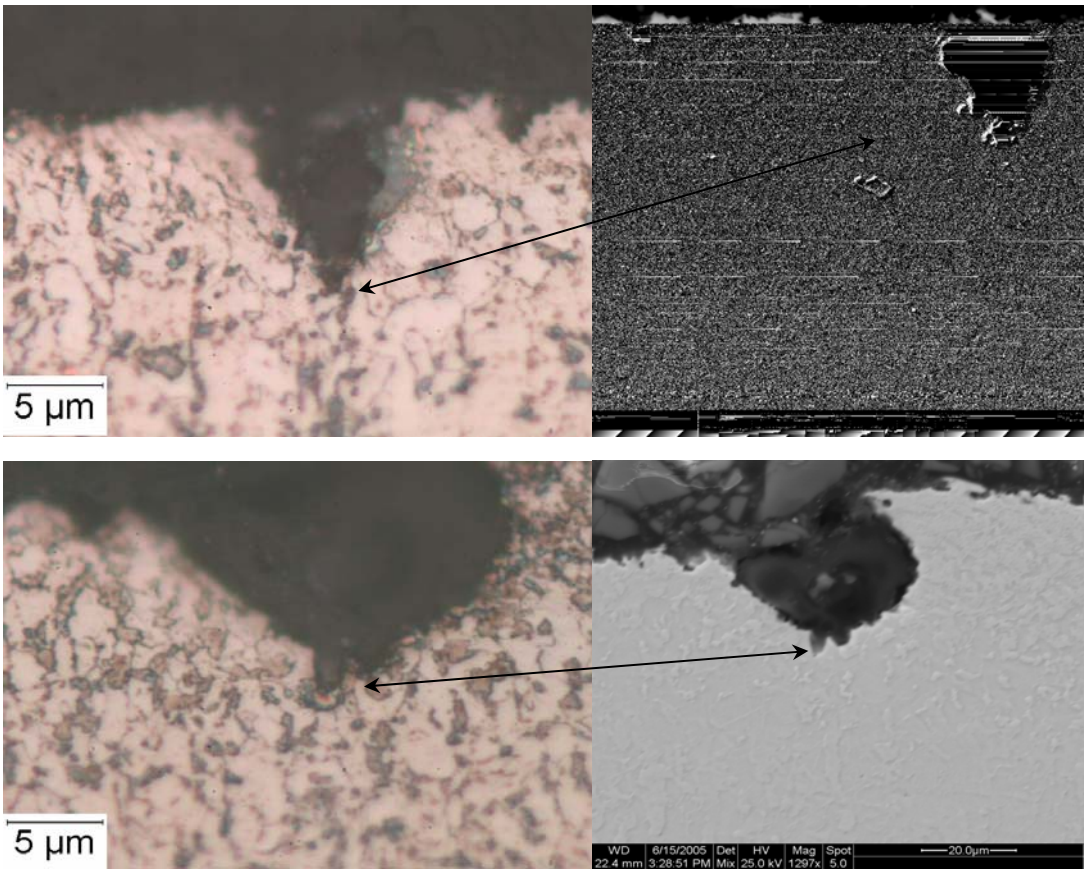

Figure 6.26. Magnification of Figure 25b and 25c. Notice that micro-cracks are present at the sharp bottom of the deep pits.

6.4.2 Pipeline Steel of Grade X80

Pipeline steel of Grade X80 was tested employing the cathodic charging cell for 12, 24, and 36 hours to determine the effect of magnetization on hydrogen-induced cracking. Because the 12-hr experiment under magnetizing conditions and the 24-hr experiment without magnetization revealed neither pits nor cracks, the 12-hr test under non-magnetization was not carried out. As is illustrated in Table 6.1, the 12-hr experiment is the only test missing.

Figure 6.27 shows the result of the optical and metalographic analyses of the 12-hr HIC experiment under magnetizing conditions. An exhaustive examination of the outer surface of the steel specimen after the cathodic charging test revealed that neither pit nor cracks were found. As seen in Figure 5.5, the metalographic analysis confirms the fact that there is no accumulation of non-metallic inclusions in the microstructure of the tested steel. Regarding the manufacturing process, it can be assumed that this pipeline steel was produced following better manufacturing quality control procedures than the tested pipeline steel of Grade X70.

The HIC steel specimen used for this 12-hr experiment is 5/8 in (1.53 cm) thick. Therefore, the separation distance between the permanent magnet employing for magnetizing-conditions tests is not the same as the distance achieved using steel of Grade X70 specimens. This apparatus configuration error was discovered and another sample was sectioned from a 60º bending angle sample and charged following the same experimental plan. The results revealed the same characteristics observed in Figure 6.27; i.e. an undisturbed surface. This is the reason why no microphotographic evidence was taken.

(a)

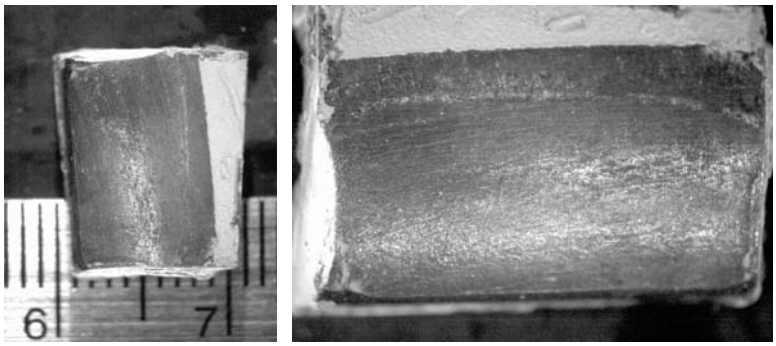

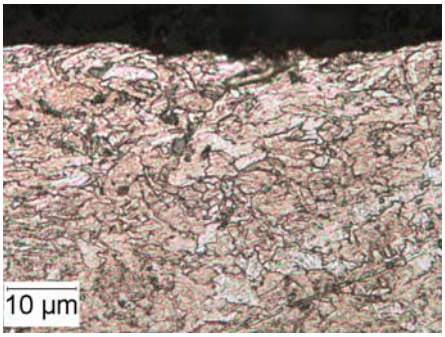

(b)

Figure 6.27. Pipeline steel of Grade X80 specimen after being charged for 12 hours under magnetizing conditions (a). Notice that neither pits nor cracks were observed. Metalographic analysis revealed an undisturbed feature of the exposed surface of the specimen (b).

Figure 6.28 exhibits a non-pit, non-crack exposed surface of the 24-hr HIC steel specimen under non-magnetizing conditions. This undisturbed outer surface revealed that a full-day of cathodic charging using experimental solution was not enough to produce neither localized corrosion (pitting) or cracks in a high-stressed bending sample. Evidence of cold-work are revealed in Figure 6.28 where no cracks where detected even at very high magnification.

Figures 6.29, 6.31, and 6.31 illustrate solid evidence of how magnetization affects the phenomenon of hydrogen-induced cracking in the tested pipeline steel of Grade X80 after 24 hours of cathodic charging under experimental conditions. Figure 6.29 shows the steel of Grade X0 specimen after 24 hours of charging under magnetizing conditions, where few bright zones exhibit a minor concentration of pits.

Figures 6.30 displays a higher-magnified illustration of Figure 6.29b. The pit density is classified as minor; however, the pit concentration is considerably higher inside the small brighter areas shown in Figure 6.29b. The larger and deeper pit observed in Figure 6.30a is

evaluated at high magnification where several microcracks are observed at the bottom of this pit. Cracks propagation follows a transgranular path and the grain boundaries can be noted.

Figure 6.31 shows the metalographic examination of the exposed, outer surface of the steel specimen. Because of the very low (minor) concentration of pits, the metalographic sample was not cut off from the HIC specimen through the zone where pits are localized. Therefore, very deep pits and cracks were not observed; however, a disturbed surface was detected. That is, irregularities similar to pits were revealed in Figures 6.31a and 6.31b.

The pipeline steel of Grade X80 specimen tested under non-magnetizing, 36-hr charging conditions is exhibited in Figure 6.32 while Figure 6.33 shows the same specimen under magnetization. Once more, both illustrations confirm that in fact a strong, continuous magnetic field accelerates the hydrogen damage in the tested steel. Pits and cracks were not detected in the specimen surface after being charged for 36 hours without magnetization (see Figure 6.32). In contrast, a heavy concentration of pits and several microcracks were detected in the surface of the specimen charged after 36 hours under magnetizing conditions (see Figures 6.33 and 6.34). Even though the tested material may be classified as high-quality pipeline steel of Grade X80 because of its uniform microstructure, its susceptibility to HIC increases under magnetizing conditions.

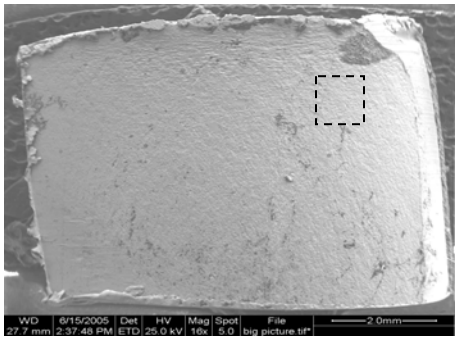

(a)

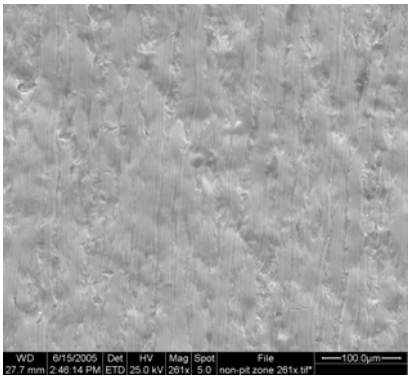

(b)

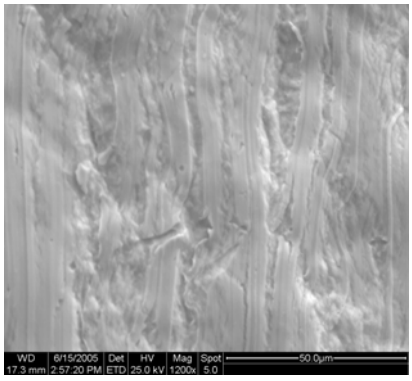

(c)

Figure 6.28. Pipeline steel of Grade X80 specimen after being charged for 24 hours under non-magnetizing conditions (a). Notice that neither pits nor cracks were observed. SEM analysis revealed evidences of cold-work in the confined area in (a), (b-c).

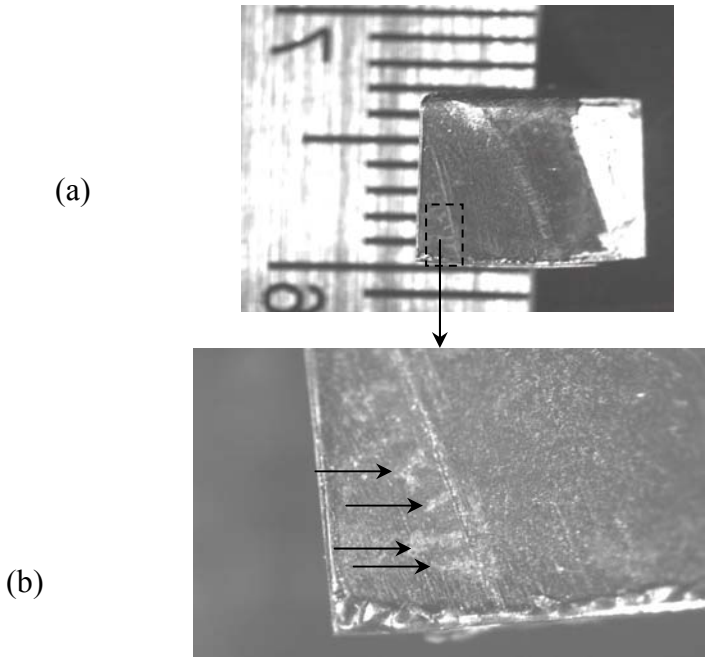

Figure 6.29. Pipeline steel of Grade X80 specimen after 24 hours of cathodic charging under magnetizing conditions (a). Notice that it reveals a minor concentration (brighten zones indicated in b with arrows) with apparently no macrocracks.

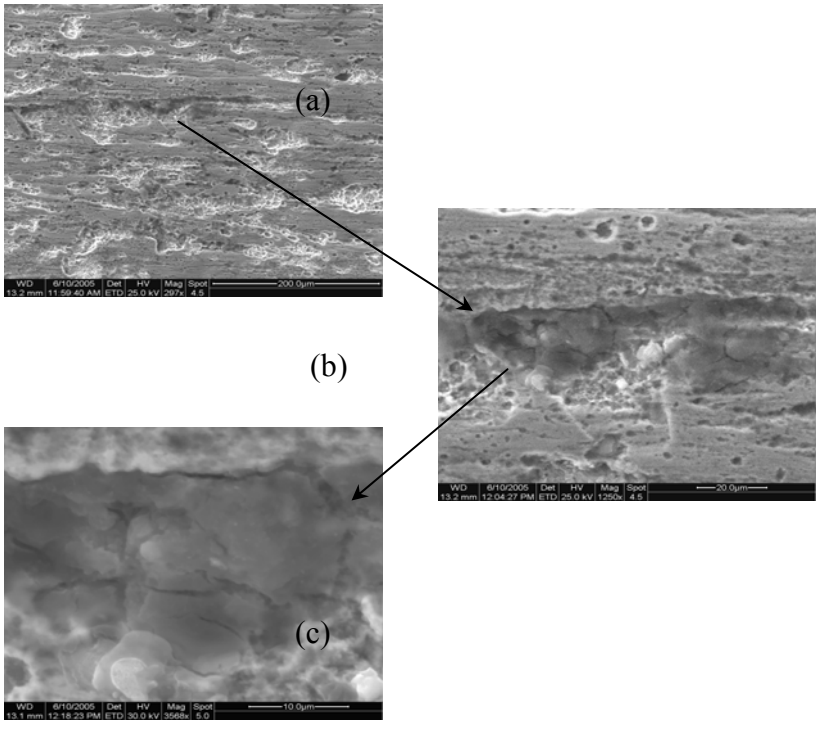

Figure 6.30. Higher magnification of Figure 6.29b (a). Although the bright zones seem to be small in Figure 6.29a, the concentration of pits is considerably high. Notice that a large, moderate deep pit contains multiple microcracks at the bottom (b). Cracks propagate following a transgranular path the grain boundaries can be delimited.

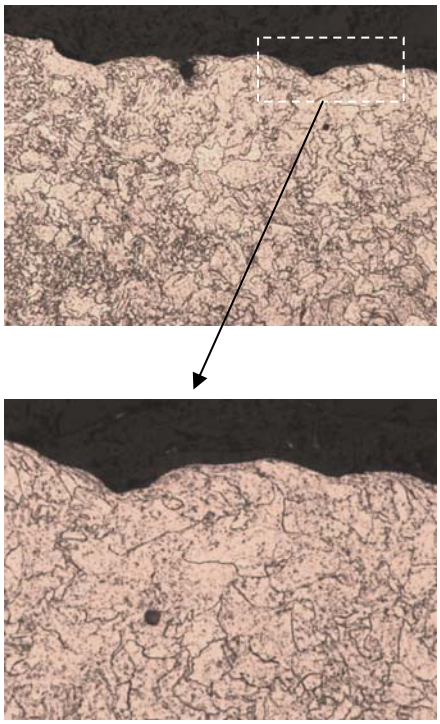

Figure 6.31. Metallography resulted from the examination of the exposed, outer surface of the steel specimen (a, 200x) and magnification of the squared area (b, 500x). Deep pits and cracks are not observed because the sample was not cut off from the HIC specimen through the zone where pits are localized. However, irregularities similar to pits are revealed.

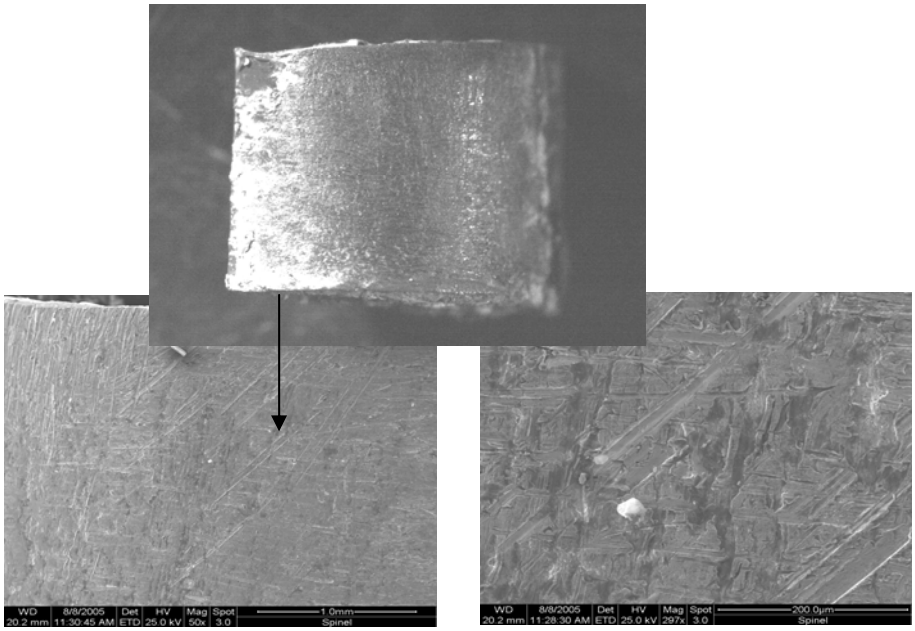

Figure 6.32. Pipeline steel of Grade X80 specimen after being charged for 36 hours under non-magnetizing conditions (a). Notice that neither pits nor cracks were observed. SEM analysis revealed evidences of cold-work in the confined area in (a), (b-c).

(a)

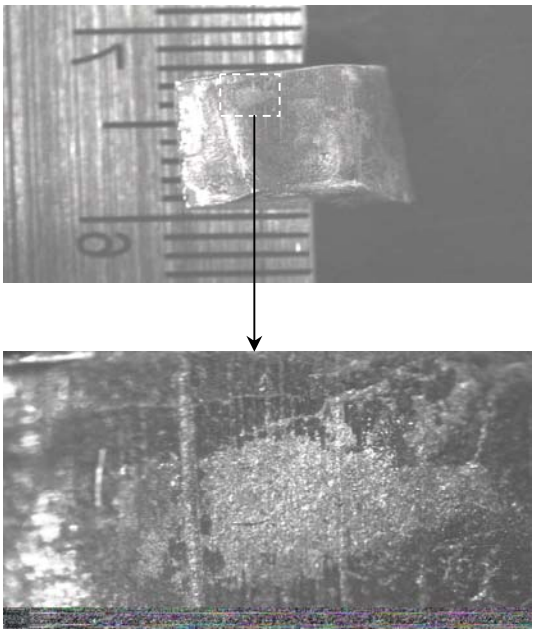

(b)

Figure 6.33. Pipeline steel of Grade X80 specimen after being charged for 36 hours under magnetizing conditions (a). Notice that there is a heavy concentration of pits (square) in the maximum tensile stresses area of the specimen (b).

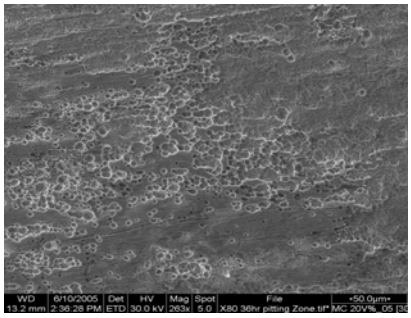

(a)

(b

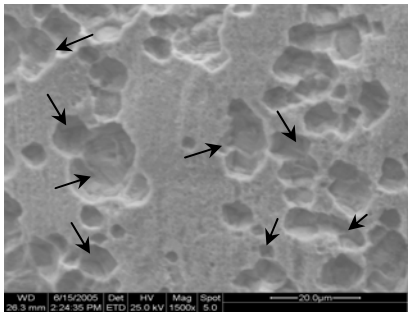

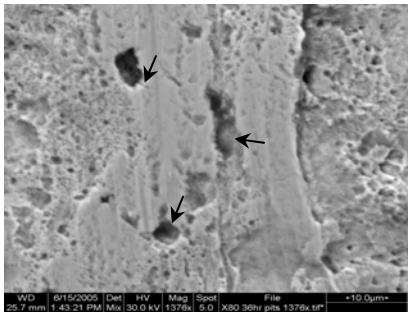

(c)

Figure 6.34. High magnification of the brighten zone of Figure 6.33b. Notice that there is a high concentration (heavy) of pits (a) and several microcracks (b-c, arrows) in the exposed area of the tested steel of Grade X80.

7. ANALYSIS OF RESULTS

The purpose of this Section is to identify the physical, metallurgical, and chemical fundamentals that permit evaluation and interpretation of the results. The results obtained from the assessment of the magnetization effect on hydrogen content and damage using the charging cell are explained in this Section.

In general terms, these outcomes point out some pertinent questions that will be addressed using references and scientific assumptions made by the research group. These questions are:

a. Why did the absorbed hydrogen content in the tested pipeline steels increase with magnetization?
b. Why are diverse pipeline steels affected differently by magnetization in terms of hydrogen concentration?
c. What is the real effect of pipeline pigging tools on hydrogen content in steels and how can this effect be interpreted?
d. Why did the absorbed hydrogen content in the cold-worked pipeline steels increase with magnetization and why is this effect different between steels of Grades X70 and X80?
e. How do the charging specimen shapes and dimensions affect the absorbed hydrogen content in cold-worked pipeline steel samples?
f. Why did the magnetization of 2 Tesla (20,000 Gauss) affects the hydrogen-induced cracking susceptibility of pipeline steels and why is the effect different between steels of Grades X70 and X80?

These questions can be categorized in four principal groups.

- The first group, questions a, b, and c, refers to the evaluation of magnetization effect on absorbed hydrogen content in the tested pipeline steels.
- The second, questions d and e, and refers to the assessment of the effect of a strong, continuous magnetic field on hydrogen content in cold-worked pipeline steel samples
- The third group, question f, refers to the assessment of the effect of a magnetic field on hydrogen-induced cracking in the tested steels, respectively.

7.1 Group 1: Absorbed Hydrogen Content as a Function of Magnetization.

As noted in Section Two, it is known that the 3d band of the iron atom is partially filled out with five electrons with ↑-spin and only one with ↓-spin. As a result, there is a spin polarization of the atom with a permanent moment, because the number of electrons with ↑-spin is unequal to the number of electrons with ↓-spin. Therefore, the strong, continuous magnetic field applied externally to the pipeline steel (iron-base ferromagnetic material) samples during the experiments produced a major component in the magnetic field direction. That is, at the saturation magnetization value of approximately 1.8 Tesla (18,000 Gauss), the domain configuration showed electron spins of parallel alignment; i.e., all magnetic moments are aligned parallel. Based on the quantum mechanic exchange energy concept, the exchange energy or exchange force is repulsive for electrons with parallel spins. This repulsive force due to parallel spins may distort the metal lattice in two possible ways: (a) producing a larger separation from

one atom to another or (b) producing a void because an electron jumps to a nearest neighbor creating an empty space and a double occupancy.

On the other hand, hydrogen, the lightest element of the periodic table, is an interstitial atom that, in the solid state, occupies interstitial sites between atoms; i.e., the interstices of the metal lattice. As was described in Section Three, at the experiment temperature (room temperature), the hydrogen atom dissociates into a proton and an electron ($H^o \Leftrightarrow H^+ + e^-$) in the steel where protons occupy interstitial positions and electrons go to the iron d-band. These interstitial sites are called hydrogen traps.

Because the positive charge of the protons has to be screened to preserve electrical neutrality, a screening occurs by the formation of an electronic cloud of atomic dimensions. But, the screening is not perfect, and repulsive forces occur between the proton and the neighboring positively charged metal nuclei. This situation leads to another kind of local expansion and thereby a distortion of the lattice.

The distortion of the steel lattice and production of internal layer voids due to the parallel aligned magnetic moments (parallel-spins) and repulsive electronic forces, as well as the preference of hydrogen to move on to empty spaces or interstitial sites in the solid state, lead to the following statement which was experimental proved: *"a strong magnetic field externally applied to the tested pipeline steels produces more available, suitable sites where hydrogen can preferentially diffuse and be trapped, increasing the absorbed hydrogen concentration."*

Once the effect of magnetization on hydrogen content in the tested steels has been described, the next step was to determine why those steels are affected differently. The answer is related to steel microstructures, chemical compositions, and mechanical properties, as well as hydrogen solubility in different steel phases.

Microstructural heterogeneities in steels produce a significant effect on hydrogen diffusion because of the attractive interactions of dissolved hydrogen with lattice imperfections. Microstructure constituents, such as grain boundaries, segregations, non-metallic inclusions, and alloying elements have also an effect on hydrogen diffusion.

Large carbides, segregations of alloying elements, and elongated non-metallic inclusions are very potent sites for hydrogen trapping and facilitate initiation and propagation of cracks. The hydrogen diffusion coefficient for steel containing elongated non-metallic (sulphide) inclusions is higher in the longitudinal direction than in the transversal one. Particular arrays of aligned inclusions provide sites for hydrogen to accumulate at the inclusion/interface and initiate cracking.

Particular alloying elements and their concentration affect hydrogen diffusion and content in steels. Chromium, nickel, and molybdenum tend to disturb hydrogen diffusion (low rate) because of sufficient effective barriers. As a result, high concentration of these elements would increase trapped hydrogen content.

Higher strength steels have more sites of high-stress triaxiality, which are known as regions of locally increased solubility because hydrogen atoms diffuse preferentially into these regions. The larger the triaxial component, the greater the amount of hydrogen that is absorbed.

The solubility of hydrogen and total hydrogen content in iron-base alloys depend also on the crystallographic structure of the alloy. The lowest hydrogen solubility is reached in the BCC α-iron, while the highest is achievable in the DHCP ε-iron. In the FCC γ-iron, it is noticeably higher than in the BCC α-iron. Thus, the lattice diffusivity of hydrogen in ε-phase and γ-phase is much lower than in α-phase.

Based on the results noted in Figure 6.18, the absorbed hydrogen content without magnetization increases as the steel yield strength increases. However, this perception is not quite precise because the original hydrogen content already in the steel at zero charging time is greater as the yield strength increases. The reason is associated with the steel making process. It is important to note that all of the hydrogen charging samples were baked at 400ºC for one hour to remove any remain diffusible hydrogen from manufacturing.

Under a strong magnetic field the total absorbed (trapped and diffusible) hydrogen concentration increases as the yield strength decreases. In other words, the effect of magnetization in terms of hydrogen content is much higher in the steel of Grade X52 than of steel of Grades X70 and X80. Moreover, the hydrogen content in steel of Grade X80 is lower than in steel of Grade X70. The author suggests that the reason of this substantial difference is shown in Table 7.1.

Table 7.1. Comparative description of tested pipeline steels.

Steel Grade	Yield Strength (Min. API)	Microstructure		
		General Description	Carbides at Grain Boundaries	Non-Metallic Inclusions
X52	52,000	Mixed ferrite structure with small concentration of carbides at grain boundary besides the coarse grains, few grains of pearlite, and greater fine ferrite grain concentration	Yes	Yes
X70	70,000	Mixed ferrite structure with small concentration of carbides at grain boundary besides the coarse grains, few grains of pearlite	Yes	Yes
X80	80,000	Acicular ferrite structure with sub-grain formation	No	No

The hydrogen concentration depends on hydrogen diffusion coefficient (material constant) and hydrogen permeability. In addition, the lattice diffusivity in BCC α-phase is much higher than in other iron-phases. Therefore, it is noted that the hydrogen diffusion coefficient, and consequently the total hydrogen concentration, in the steel of Grade X52 under a strong magnetic field is greater than in steels of Grades X70 and X80. It is thought to be because of the higher

concentration of finer ferrite grains and micro-structural heterogeneities such as carbides at grain boundaries and non-metallic inclusions, in addition to the effect of lattice distortion generated by the external magnetic field. At the same time, the hydrogen concentration in steel of Grade X70 is higher than in steel of Grade X80 is probably from the same cause but at a lower magnitude. In contrast, the acicular ferrite microstructure with no carbides or inclusions seems to allow a lower concentration of hydrogen.

In summary, a strong and continuous magnetic field of approximately 2 Tesla (20,000 Gauss) accelerates either the solubility of in tested pipeline steels. This phenomenon would be attributed to a combination of factors:

(a) High hydrogen solubility iron phases and microstructures, and
(b) Lattice distortion due to the external magnetic field that may increase either diffusivity or permeability of hydrogen in steels.

Pipeline pigging tools (MFL tools) apply the saturation magnetic flux density for few seconds while the pig moves at the velocity of 0.5-5.0 m/s through the pipe. When the imposed magnetic field is removed, the magnetic flux density will not relax back to zero at which the pipeline steel probably was before pigging. The amount of magnetization it retains at zero driving fields is called remanent magnetization.

Figure 6.18 and Table 6.1 show the graphical expression of the experimental data obtained during the absorbed hydrogen concentration test. It has been stated that a saturation magnetic induction of approximately 2 Tesla (20,000G) and 0.05 A/cm^2 current density can increase by more than six times the total hydrogen content in pipeline steels. The question to be addressed is: how much the absorbed hydrogen content increase under the remanent magnetization left by the Magnetic Flux Leakage tool after inspection operations?

This fundamental question can be addressed by the analysis of the in-between points from Figure 7.1, which is the graphical representation of Equation 6.3 applied to all of the tested pipeline steel grades. As the remanent magnetic induction (Br) in the steel grades is approximately 1 Tesla (10,000 Gauss), the potential absorbed hydrogen content increases up to 1.62 times, as it is showed in Table 7.2. However, this situation is possible if the magnetization is constant and does not alternate with aging. Surface anomalies could also increase the magnetic induction over these measured values. Surface anomalies such as cracks (at crack tip) and dents (cold-worked areas) considerably increase the magnetic flux density within the MFL process. They can reach a magnetization level greater than the remanent, thus the potential absorbed hydrogen concentration under these conditions would increase by more than sixty percent.

7.2 Group 2: Cold-work Effect

It has been stated that dislocation density increases with deformation and hydrogen diffusivity decreases with increasing cold work. Cold work increases the number of dislocations (which results in a higher state of internal or residual stresses), highly elongates grains in the working direction, and increases the number of precipitation sites. After deformation, commonly used pipeline steels develops a preferred orientation, called texture, that produces anisotropy in

mechanical properties that always accompanies the formation of deformation bands and shear bands (Huang 1995; Dieter 1976).

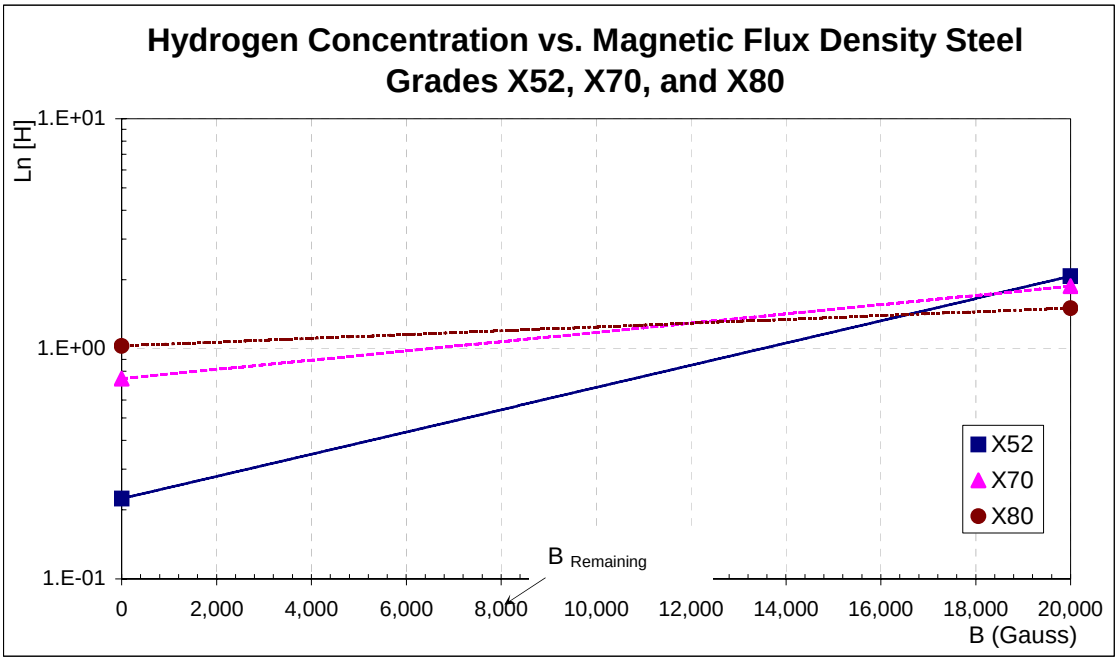

Figure 7.1. Graphical Representation of Equation 6.3 applied to all tested steel grades.

As noted earlier, magnetization produces a significant effect on total hydrogen content in pipeline steels. In other words, under a strong magnetic field of approximately 2 Tesla (20,000 Gauss), the absorbed hydrogen concentration may increase up to three times in steel of Grade X70 and 1.6 times in steel of Grade X80.

Table 7.2. Determination of intermediate points at Magnetic Flux Density of 1 Tesla

Parameter at 1 Tesla (10,000 Gauss)	Tested Pipeline Steel Grade		
	X52	**X70**	**X80**
Ln[H]	0.606	1.223	1.258
$[H]_{B=10kG}$ (ppm)	1.834	3.398	3.517
$[H]_{B=0}$ (ppm)	1.250	2.100	2.800
$[H]_{B=10kG}$ / $[H]_{B=0}$ Ratio	1.47	1.62	1.26

Figures 6.25 and 6.26 show that bent steel samples can absorb a tremendous amount of hydrogen after three hours charging with the 1N H_2SO_4 solution at a current rate of 0.05 A/cm^2. Total hydrogen content increases with the bending angle, 60º cold worked samples had the highest residual-stress and highest hydrogen content.

The cold worked specimens without magnetization absorbed much more hydrogen than as-received steel specimens. Deformed steel of Grade X70 specimens bent at 120º, 90º, and 60º angle absorb up to 3.6 times more hydrogen than non-cold worked samples. Cold worked steel of Grade X80 samples absorb hydrogen up to 2 times more. This experimental approach confirms the results obtained in previous research where it was concluded that hydrogen concentration in steel samples increases with increasing cold work.

However, the purpose of this study is not related to the cold work effect on hydrogen content in pipeline steel, but rather the magnetization effect on cold worked samples. The reason that this is even noted is pipelines can be mechanically damaged due to third-party triggers and the presence of severe dents is always possible.

The experimental data documented on Figures 6.25 and 6.26 show that a strong magnetic field produces an enormous effect on total hydrogen concentration in the tested pipeline steels under cold work conditions. The cold worked steel Grade X70 samples can absorb up to 9.4 times more hydrogen than an as-received steel samples under the same magnetic induction. The steel Grade X80 samples can absorb up to 3.7 times the amount of hydrogen than an as-received sample under the same experimental environment.

The results show some relevant questions that must be addressed: why is the effect of magnetization under same magnetic induction conditions is different in the tested pipeline steels of Grades X70 and X80? There is any relation to the shape and dimension of the charging-bending specimens? Does strain distribution throughout specimens' thickness and width cause a significant effect?

The reason why the tested steel of Grade X70 absorbs more hydrogen than steel of Grade X80 under a magnetic induction has been discussed in terms of the effect of metallurgical parameters and material properties. However, the reasons why the hydrogen concentration range in the steel of Grade X70 is much larger than the range obtained from the steel of Grade X80 needs to be addressed.

Complexity of the strain distribution in both sets of specimens, and consequently the range of values, is related primarily to the orientation and location of the cut-off bending samples. Figures 6.19 and 6.21 reveal that the maximum residual stresses are located at the bending centerline. The fibers on the outer surface are stretched while the fibers on the inner surface are compressed. Any point located next to the centerline throughout the width of the sample would have a different plastic strain distribution, which it is thought to be directly related to the behavior of absorbing hydrogen. A specimen that presents a higher concentration of stretched fiber would absorb more hydrogen because residual tensile stresses increase the number of sites where hydrogen would diffuse into and be trapped. In a word, from Figures 6.25 and 6.26 it is

suggested that in highly cold worked steels of Grades X70 and X80 specimens under experimental conditions, the total absorbed hydrogen concentration could reach up to 59.9 and 14.9 ppm, respectively. These concentration quantities are extremely detrimental for high-strength pipeline steel in hydrogen-bearing environment.

Another possible issue is that the steel of Grade X70 samples are 9/32 inches (7.14 mm) thick while the steel of Grade X80 samples are 5/8 inches (15.9 mm) thick. This thickness differential produces a significant variation of the distance between the magnetic field suppliers. Therefore, the magnetic induction is not the same for both sets of specimens. The steel of Grade X80 samples were sectioned into two dimensionally similar cold worked charging samples. As a result, because of the inaccuracy of the sectioning methodology, the magnetic field of 2 Tesla (20,000 Gauss) was applied inconsistently to both sets of samples. Even though this inconsistency was not reported, the detected difference ranges from 0.05 to 0.1 Tesla (500 to 1000 Gauss), which was considered as irrelevant in terms of magnetic induction at the saturation point. The applied magnetic field of 2 Tesla (20,000 Gauss) was selected as it is larger than the experimentally defined saturation point by approximately 0.2 Tesla (2,000 Gauss). Therefore, it is suggested that the shape and dimensions of the cold worked charging specimens could affect the reported amount of the intaken hydrogen content.

7.3 Group 3: Hydrogen Induced Cracking

Hydrogen induced cracking, hydrogen stress cracking, or hydrogen embrittlement are terms used to describe the hydrogen damage in materials. This cracking mechanism is primarily associated with the absorption of hydrogen and a delayed time to failure called the incubation time. During the incubation time hydrogen diffuse into regions of high triaxial stresses creating sites of high concentration of hydrogen. The deleterious effect of hydrogen on delayed failure increases because of the triaxiality of the stress state in components under an applied stress (ASM 2002).

Hydrogen embrittlement susceptibility of steels under hydrogen-containing atmospheres is commonly affected by factors such hydrogen concentration, stress intensity, metallurgical structure of steel, temperature, environment, and solution composition. Previous sections describe that the *concentration of hydrogen* in steel is basically a function of hydrogen-bearing environment pressure, alloy crystal structure, and temperature. However, another parameter would be added to the list is magnetization. Indeed, based on the obtained results, a strong magnetic induction of approximately 2 Tesla (20,000 Gauss) under laboratory conditions enormously increases the hydrogen content in the studied steels.

Hydrogen induced cracking or hydrogen damage occurs when hydrogen content in the steel matrix exceeds the threshold hydrogen content. This critical point is considered a material property and decreases with increased steel yield strength. Besides, a high density of non-metallic inclusions and segregations in the matrix also reduce the threshold hydrogen concentration. Lower fractions of inclusions and other type of metallurgical heterogeneities in the steel corresponded to higher resistance to hydrogen damage. The pipeline steel microstructure plays an important role in hydrogen damage resistance. Ferritic pipeline steels as well as bainite and un-tempered martensite are the most susceptible microstructures. Quenched-

tempered and normalized are the most resistant to hydrogen embrittlement. It has been stated that banded structure presented by microalloyed steels may contribute to increase hydrogen damage resistance at specific conditions. That is, heavily banded microstructures could enhance hydrogen-induced cracking by providing low fracture resistance paths for cracks to propagate.

Recent studies have stated that the acicular ferrite-dominated structure is the optimum candidate microstructure for pipeline steels in hydrogen-bearing environments (in particular, oil and gas sour service), while ultra fine ferrite microstructure is in second position in terms of hydrogen damage resistance. The ferrite-pearlite microstructure possesses the worst hydrogen embrittlement (sulfide stress cracking) resistance because since carbides and MnS inclusions precipitate along the banded pearlite. Hydrogen diffuses to their interfaces reaching the threshold hydrogen concentration more quickly.

The definite effect of strong magnetic induction on hydrogen induced cracking in high-strength pipeline steels has been studied. The susceptibility to hydrogen damage of the tested steel of Grade X70 without magnetization is higher than the of Grade X80. But, under a strong magnetic induction and laboratory conditions the susceptibility is even worst. In other words, cracks were detected in the steel of Grade X70 after 12 hours charging under magnetization whereas no cracks were observed after 12 and 24 hours of continuous un-magnetized charging. On the other hand, after 36 hours of charging no cracks where detected in the steel of Grade X80 without magnetization, but several cracks were found after 24 and 36 hours charging under the effect of the strong magnetic induction. It was noticed that the cracks observed in both steel grades initiate at pits and, in the case of the steel of Grade X70, they propagate following a particular arrays of aligned inclusions. The propagation pattern of cracks in the steel of Grade X80 was not determined.

The reason why magnetization affects hydrogen damage in the studied high-strength steels is related to of the total hydrogen concentration and the steel characteristics and properties. The strong magnetic induction of 2 Tesla (20,000 Gauss) increases hydrogen content in the steel and accelerates the cracking mechanism because the threshold hydrogen content is reached quicker, while microstructure defects such as inclusions increase the density of crack initiation points.

The magnetization affects steels of Grades X70 and X80 differently because of their inherent microstructure and material quality. Low quality steels, such as the tested steel of Grade X70, are more susceptible to hydrogen damage than cleaner steels. The metallurgical heterogeneities density is the steel of Grade X80 is much lower than in the steel of Grade X70, and the microstructure is more resistant to hydrogen stress cracking.

The results reported in Section 6 show the tremendous effect of saturation magnetic induction on the cracking mechanism in cold worked steel samples. However, the pipeline magnetic flux leakage (MFL) tools leave a remanent magnetization value after inspection, which is held by the steel for a long period of time. Therefore, the questions to be addressed are: how long the remanent magnetization is held by the pipeline steels after pigging? Does remanent magnetization affect the cracking mechanism in the same way than the saturation magnetization? These questions could be addressed with further research. Furthermore, this subject could be considered as a potential future work task.

8. CONCLUSIONS AND RECOMMENDATIONS

In this report, the effect of strong magnetic fields on absorbed hydrogen concentration and hydrogen induced cracking in high-strength, thick walled pipeline steels has been experimentally demonstrated by laboratory experiments. The effects of high level of residual stresses and magnetization in pipeline steels have also been assessed. This section presents the principal remarks and conclusions obtained from the experimental results shown in Section 6 and analyzed in Section 7. Additionally, a list of future work tasks is presented as the recommended assignments needed to achieve a better understanding of the phenomenon as shown in this dissertation.

NOTE: ***The results presented for steel grades X-52, X-70 and X-80 refer to the specifications of these steel samples. The actual yield strengths for these grades were closer to 70 ksi (X-52), 80ksi (X-70) and 90 ksi (X-80). Thus the data for hydrogen absorption and its effect on the observed hydrogen cracking susceptibility should be considered for the actual strengths.***

8.1 Remarks

a. The effect of magnetization on the hydrogen absorption decreases with increased steel yield stress. Under laboratory conditions, the tested pipeline steel of Grade X52 absorbs more hydrogen than steels of Grades X70 and X80. The steel of Grade X80 absorbs the lowest amount of hydrogen. It is noted that the material properties and microstructures appear to produce a significant effect on the obtained outcomes.

b. Cold worked specimens under laboratory conditions and with no magnetic induction applied externally absorb much more hydrogen than non cold-worked steel specimens. Total hydrogen concentration increases with the sharper bending angles, 60º-cold-worked samples had the highest residual stress. Deformed steel of Grade X70 specimens bent at 120º, 90º, and 60º angle absorb up to 3.6 times more hydrogen than unadulterated samples; while cold-worked steel of Grade X80 samples absorb hydrogen up to 2 times more.

c. In highly cold-worked steels of Grades X70 and X80 specimens under magnetization conditions, the total absorbed hydrogen concentration can reach up to 59.9 and 14.9 ppm, respectively. The tremendous dissimilarity is thought to be because of the complexity of the strain distribution in both sets of specimens, steels microstructure, and mechanical properties. A specimen that presents a higher concentration of stretched fiber would absorb more hydrogen because residual tensile stresses increase the number of sites where hydrogen would diffuse into and be trapped. These values of hydrogen concentration are extremely detrimental for high-strength pipeline steel in hydrogen-bearing environment.

d. The susceptibility to hydrogen damage of the tested steel of Grade X70 without magnetization is higher than the steel of Grade X80. But, under a strong magnetic induction and laboratory conditions the susceptibility increases. It was noted that the cracks

observed in both steel grades initiate at pits and, in the case of the steel of Grade X70, they propagate following a particular array of aligned inclusions.

e. A magnetic induction of approximately 2 Tesla (20,000 Gauss) accelerates the hydrogen damage phenomenon in high-strength thick walled pipeline steel under laboratory conditions. It is suggested that this effect depends on the concentration of hydrogen absorbed due to magnetization and the susceptibility to this hydrogen stress cracking of the tested steels.

f. The applied saturation magnetic induction affects steels of Grades X70 and X80 in different ways because of their microstructure and material quality. Low quality steels, such as the tested steel of Grade X70, are more susceptible to hydrogen damage than cleaner steels. The metallurgical heterogeneity density in the steel of Grade X80 is much lower than in the steel of Grade X70, and the microstructure is more resistant to hydrogen stress cracking.

8.2 Conclusions

a. A strong, continuous magnetic induction produced by MFL pipeline pigging tools of approximately 2 Tesla (20,000 Gauss) causes an increase in the total absorbed hydrogen concentration in the tested high-strength pipeline steels of Grades X70 and X80 in a hydrogen environment. It is thought to be because of the distortion of the steel lattice and production of internal voids due to the parallel-aligned magnetic moments and repulsive electronic forces, as well as the preference of hydrogen to move into empty spaces or interstitial sites in the solid state.

b. At a remanent magnetic induction of 1 Tesla (10,000 Gauss), the adsorbed hydrogen concentration in the tested high-strength pipeline steels increases by approximately sixty percent. At saturation magnetization (i.e. during pigging), the concentration could be as high as six times.

c. A strong magnetic field of approximately 2 Tesla (20,000 Gauss) produces an significant increase on total hydrogen concentration in the tested cold worked pipeline steels. The bent steel of Grade X70 samples can absorb up to 9.4 times more hydrogen than an as-received steel samples under the same magnetic induction. The steel of Grade X80 samples can absorb up to 3.7 times the amount of hydrogen absorbed by non-coldworked samples under the same experimental environment.

d. Magnetization increases absorbed hydrogen concentration in the steel and accelerates the cracking mechanism because the threshold hydrogen content is reached quicker. Microstructure defects, such as inclusions, increase the density of crack initiation points.

e. The reported results revealed that hydrogen damage or hydrogen induced cracking susceptibility of pipeline steels is negatively affected by magnetization at saturation levels. This suggests that the remanent magnetization left by magnetic flux leakage inspection

tools might also significantly affect the susceptibility to this cracking mechanism; however, a conclusive effect is to date undetermined.

f. Recommendations

The entire set of experiments was conducted under severe laboratory conditions where a magnetic field at saturation level of approximately 2 Tesla (20,000 Gauss), similar to the saturation induction applied by MFL tools, and a charging solution of 1N H_2SO_4 at a current rate of 0.05 A/cm^2 were employed. The effect of temperature on the susceptibility of pipeline steels to hydrogen damage under magnetization is unknown because the tests were run at room temperature. It has been stated that solubility of hydrogen in steel phases increases with temperature, but at high temperature the hydrogen damage susceptibility decreases.

The magnetization level left by MFL tools after pigging for an indefinite period of time is much lower than the saturation level and the absorbed hydrogen concentration is steels increases with deformation. Therefore, the effect of the remanent magnetization just after pigging on hydrogen absorption in unstressed and cold worked sections should be studied.

The total absorbed hydrogen content in steels under magnetization increases considerably in pipeline steels; however, the cause of this is uncertain in terms of solubility or permeability of hydrogen. Hydrogen permeability or hydrogen diffusivity cells could be appropriately designed and setup in order to assess this phenomenon.

The susceptibility of hydrogen damage of pipeline steels under magnetization conditions could be predicted scientifically. Predictive model based on magnetization level, mechanical properties and metallurgical features of steels, strain distribution or profile after deformation, as well as cathodic charging conditions should be developed.

Because of these uncertainties, the research group proposed a set of additional tasks to be addressed in order to have a much better understanding of this significant phenomenon and the parameters that affect it. The approach of this future work will facilitate the development of prevention methods to minimize pipeline damage after MFL pigging. The list of proposed future research tasks are as follow:

a. Field application of experimental results and collection of data.
b. Temperature effect on hydrogen damage in magnetized pipeline steels.
c. Hydrogen permeability and diffusivity test.
d. Development of predictive models.
e. Development of preventive methods.

The effect of temperature on the susceptibility of pipeline steels to hydrogen damage under magnetization, the effect of the remanent magnetization just after pigging on hydrogen absorption in unstressed and cold worked sections, the effect of cathodic protection techniques on hydrogen damage after pigging, and the effect of magnetization on permeability and diffusivity of hydrogen in pipeline steels have to be well understood in order to develop a predict model and define prevention methods. The mathematical model would assist estimations of pipeline remanent life and the pipeline industry would be able to predict hydrogen damage in hydrocarbon transportation networks due to the magnetization left by magnetic flux leakage inspection tools.

REFERENCES

American Petroleum Institute –API– Specification 5L: "Specification for Line Pipe". Forty-Second Edition, 2000.

American Society of Metals - ASM: "Corrosion: Fundamentals, Testing, and Protection." Handbook Volume 13A, 2002.

American Society of Metals - ASM: "Failure Analysis and Prevention." Handbook Volume 11, 2002.

AMT - Australian Magnet Technology PTY Ltd., History of Permanent Magnets, 2002. Web site: www.magnet.au.com

ASTM F1113-99: "Standard Test Method for Electrochemical Measurement of Diffusible Hydrogen in Steels (Barnacle Electrodes)."

ASTM G148-97: " Standard Practice for Evaluation Uptaken, Permeation, and Transport in Metals by an Electrochemical Techniques."

Berkowitz, A.E. and Kneller, E.: "Magnetism and Metallurgy - 1." Academic Press, 1969.

Bhatia, A. and Westwood, S.: " Developing a baseline in-line inspection program with design and operational decisions on the use of a high resolution magnetic flux leakage tool," paper NACE No. 3172 presented at the NACE International Annual Conference and Exposition, 2003.

Beuker, T. and Rahe, F.: "High-Quality, Smart Pig Dent Inspection Complies With Rules For Gas, Liquid Lines." Pipeline and Gas Journal, p. 40-44, March 2005.

Bickerstaff, R.; Vaughn, M.; Hassard, M.; and Garrett, M.: "Review of Sensor Technologies for In-Pipe Inspection of Natural Gas Pipeline." Sandia National Laboratories, 2002, website: www.netl.doe.gov

Bray, D.E. and McBride, D.: "Nondestructive Testing Techniques." New Dimensions in Engineering, John Wiley & Sons, Inc., 1992.

Bray, D.E. and Stanley, R.K.: "Nondestructive Evaluation, a Tool in Design, Manufacturing, and Service." Revised Edition. CRC Press, 1997.

Cahn, R.W. and Haasen, P.: "Physical Metallurgy." North-Holland, Amsterdam, 1996.

Chikazumi, S.: "Physics of Ferromagnetism." The International Series of Monographs on Physics, Vol. 94, Second Edition. Oxford University Press, New York, 1997.

Choumar, A.A.: "Pipeline Integrity Management through Intelligent Pigging Survey," paper SPE-36275 presented at the 7th Abu Dhabi International Petroleum Exhibition and Conference of the Society of Petroleum Engineers, Abu Dhabi, U.E.A, 13-16 October 1996.

Craig, B.D.: "Corrosion Product Analysis-A Road Map to Corrosion in Oil and Gas Production." Material Performance Magazine, Volume 41, No.8, NACE, August 2002.

Craig, B.D.: "Sour-Gas Design Considerations." Society of Petroleum Engineers, Monograph Volume 15, Houston, 1993.

Cullity, B. D.: "Introduction to Magnetic Materials." Addison-Wesley Publising Co., Inc., 1972.

Das, K.B.: "Hydrogen embrittlement of Cathodically Protected 15-5PH Stainless Steel." Proceedings of the Second International Congress of Hydrogen in Metals, International Association of Hydrogen Energy, Volume 1-3E1, Paris, France, 6-10 June, 1977.

DeLuccia, J.J., and Berman, D.A.: "An Electrochemical technique to Measure Diffusible Hydrogen in Metals (Barnacle Electrode)." Electrochemical Corrosion Testing, eds. Mansfeld, F, and Bertocci, U. Philadelphia, PA: ASTM, 1981, p256.

Devanathan, M.A.V. and Stachurski, Z.: "The absorption and diffusion of electrolytic hydrogen in palladium." Proceedings of Royal Society, section A270, 1962, p90.

Dieter, G.: "Mechanical Metallurgy." McGraw-Hill, Second Edition, 1976.

Du Trémolet, E., Gignoux, D., and Schlenker, M.: "Magnetism, I-Fundamentals." Klumer Academic Publishers, Norwell, 2002.

Elboujdaini M., Revied, R.W, and DeRushie, C.: "Effects of Metallurgical Parameters and Non-Metallic Inclusions on Behaviour for Oil and Gas Industry Steels on Hydrogen Induced Cracking," paper No. 528, presented at 58th Annual Conference and Exposition of NACE, 2003.

Flis, J. and Zakroczymski, T.: "Enhanced Hydrogen Entry in Iron at Low Anodic and Low Cathodic Polarizations in Neutral and Alkaline Solutions." Corrosion, NACE, p530-539, July 1992

Glicksman, M.E.: "Diffusion in Solids." John Wiley & Sons, Inc. NY, 2000.

Gräf, M., Schröder, J. Schwinn, V., and Hulka, K.: "Production of Large Diameter Pipes Grade X 70 with High Toughness Using Acicular Ferrite Microstructures." Technical paper, http://www.cbmm.com.br/.

Hagiwara, N. and Meyer, M.: "Evaluating HSC of Line Pipe Steels under Cathodic Protection Using CTOD Tests," paper No. 380, presented at 55th Annual Conference and Exposition of NACE, 2000.

Hirth, J.P.: “Effects of Hydrogen on the Properties of Iron and Steel.” Metallurgical Transactions A, Vol. 11A, pp.861-890, 1980.

Huang, H. and Shaw, W.J.D.: “Hydrogen Embrittlement Interactions in Cold-Worked Steel.” NACE International, Corrosion – January 1995, Corrosion Science Section, p30.

Ibach, H. and Lüth, H.: “Solid-State Physics.” Springer-Verlag Berlin Heidelberg, Second Edition, 1995.

Interrante, C.G.: “Basic Aspects of the Problems of Hydrogen in Steels.” American Society of Metals, Washington DC, 1982.

Jiles, D.: “Introduction to Magentism and Magnetic Materials.” Second Edition, Chapman and Hall, New York, 1998.

Kittel, C.: “Introduction to Solid State Physics.” John Wiley and Sons, Inc.1953.

Johnson, H.H. and Lin, R.W.: “Hydrogen and Deuterium Trapping in Iron.” Proceedings of the Third International Conference on Effect of Hydrogen on Behavior of Materials, the Metallurgy Society of AIME, p3-26, Wyoming, 1980.

Jones, D.A.: “Principles and prevention of Corrosion,” 2nd Edition, Prentice Hall, NJ, 1996.

Learn Electronics Tutorials. http://www.twysted-pair.com/

Leis, B.N., Francini, R.B., Kechter, G.E., and Narendran, V.K.: “Real Time Monitoring for Encroachment and Contact Detection – a Step Towards Smart Pipelines and Their Benefits.” Derived from Proceeding of the 3rd IBC – Onshore Pipelines International Business Conferences, Berlin 1999. www.battelle.org

MMC - Magnetic Materials and Components: “Neodymium Iron Boron Magnets.” New York, 2001, website: www.mmcmagnetics.com

Muhlbauer, K.: “Pipeline Risk Management Manual.” Gulf Publishing Company, Texas, 1992.

Nave, C.R.: “ Hyperphysics.” Georgia State University, Department of Physics, 2002, website: http://hyperphysics.phy-astr.gsu.edu/hbase/hframe.html

Nestleroth, J. B. and Bubenik, T. A.: “Magnetic Flux Leakage (MFL) Technology For Natural Gas Pipeline Inspection.” The Gas Research Institute, 1999, website: www.battelle.org

Nespeca, G.A., and Hveding, K.B.: “Intelligent Pigging of the Ekofisk-Emden 36-in. Gas Pipeline,” paper SPE-18232 presented at the 63rd Annual technical Conference and Exhibition of the Society of Petroleum Engineers, Houston, Texas, USA, October 2-5, 1988.

Olsen, S., Børvik, L., Rørvik, G., Aune, E.: "Risk of Hydrogen Embrittlement from Cathodic Protection on Super-Martensitic Stainless Steels," paper No. 091, presented at 56th Annual Conference and Exposition of NACE, 2001.

Oriani, R.A., Hirth, J.P., and Kmiałowski, M.: "Hydrogen Degradation of Ferrous Alloys." Noyes Publications, New Jersey, 1985.

PPSA - Pigging Products and Services Association: "An Introduction to Pipeline Pigging." Gulf Publishing Company, Texas, 1995.

Pepperhoff, W. and Acet, M.: "Constitution and Magnetism of Iron and its Alloys." Springer-Verlag, Engineering Materials. Berlin, 2001.

Pressouyre, G.M.: "A Classification of Hydrogen Traps in Steels." Metallurgy Transitions, Vol. 10A, p 1571-1573, 1979.

Porter, P.C.: "The application of new technology to the inspection of transmission and distribution pipelines," paper NACE No. 43 presented at the NACE International Annual Conference and Exposition, 1996.

Riecke, E.: "Influence of Microstructure of Iron and Steels on Steady State Hydrogen Permeation." Proceedings of the Third International Conference on Effect of Hydrogen on Behavior of Materials, the Metallurgy Society of AIME, p97-104, Wyoming, 1980.

Serna, S., Albarrán, J.L., and Perez, R.: "Effects of Wet Hydrogen Sulfide Environments on the Cracking Susceptibility of medium-Strength Microalloyed Pipeline Steels for Oil and Gas Transport," paper No. 530, presented at 58th Annual Conference and Exposition of NACE, 2003.

Stevens, M.F.: "Analysis of Trapping Effects on Hydrogen Embrittlement of a HSLA Steel." Proceedings of the Third International Conference on Effect of Hydrogen on Behavior of Materials, the Metallurgy Society of AIME, p341-348, Wyoming, 1980.

Talbot-Besnard: "Using Fundamental Studies to Find Possible Solutions to Hydrogen Problems in Steels." Proceedings of the Third International Conference on Effect of Hydrogen on Behavior of Materials, the Metallurgy Society of AIME, p361-377, Wyoming, 1980.

Tanner, B.K.: "Introduction to the Physics of Electrons in Solids." Cambridge University Press, 1995.

Troiano, F.: "Hydrogen Embrittlement and Stress Corrosion Cracking." American Society of Metals, 1984.

Vieth, P.H., Moghissi, O., and Beavers, J.A.: "Integrity-verification methods support US efforts in pipeline safety." Oil and gas Journal, December 16, 2002, pp. 52-58

Yang, L., Fong, H., and Wong, Y.: "Research on intelligent pipeline magnetic flux leakage detector," paper No. 11922 presented at 10th Asia-Pacific Conference on Non-Destructive Testing. Brisbane, Australia, 17-21 September 2001.

Zhao, M.C., Tang, B. Shan, Y.Y., and Yang, K.: "Role of Microstructure on Sulfide Stress Cracking of Oil and Gas Pipeline Steels." Metallurgical and Materials Transactions, Volume 34A, p1089, May 2003.

SELECTED BIBLIOGRAPHY

ASTM E1290-02: "Standard Test Method for Crack-Tip Opening Displacement (CTOD) Fracture Toughness Measurement." American Society for Testing and Materials, 2002.

Bhatia, A. and Westwood, S.: " Developing a baseline in-line inspection program with design and operational decisions on the use of a high resolution magnetic flux leakage tool," paper NACE No. 3172 presented at the NACE International Annual Conference and Exposition, 2003.

Choe, S.B. and Shin, S.C.: "Calculations of the Surface Shape Anisotropy Induced at Rough Surfaces of Ferromagnetic Thin Films." Journal of the Korean Physical Society, Vol. 38, No. 4, April 2001, pp. 392-395, website: www.cnsm.kaist.ac.kr

Cramer, S.D. and Covino, B.S.: "Corrosion: Fundamentals, Testing, and Protection." ASM Handbook Volume 13A, 2003.

Crouch, A. E.: "In-Line Inspection of Natural Gas Pipelines." GRI-Report 91/0365, Gas Research Institute, 1992.

Fukai, Y.: "High Pressure Phase Diagram of Transition Metal-Hydrogen Systems." Department of Physics, Chuo University, Kasuga, Bonkyo-ku, Tokio, 2000.

Garber, R.: "Effect of Carbon Content and Prior Austenic Grain Size on Hydrogen Embrittlement of 1%Cr/0.75%Mo/0.025%Nb Steel in Aqueous Hydrogen Sulfide Environment." Proceedings of the Third International Conference on Effect of Hydrogen on Behavior of Materials, the Metallurgy Society of AIME, p361-377, Wyoming, 1980.

Herve, J.L., Udeli, J. and Ling M.T.S.: "New Techniques of Pipeline Inspection," paper SPE-10402. Society of Petroleum Engineers of AIME, 1981.

Hodgman, R.Z.: "Smart Pigging Philosophy," paper NACE No. 41 presented at the NACE International Annual Conference and Exposition, 1996.

Lauer, G. and Moreno P.: "New pigs combine previously separate detection technologies." Pipe Line & Gas Industry Magazine, Vol. 84 No. 6, June 2001.

Nye, B. and Garrison, C.: "Pigging Moves On-Improves Pipeline Safety and Operational Efficiency." Pipeline & Gas Journal, August 2000.

Niyomsoan, S., Mishra, B., Olson, D.: 'The Relationship between Seebeck Coefficient and Phase Transformation of AB2 Hydrogen Storage Materials,' in progress. Colorado School of Mines, 2003.

Shamblin, T.R.: "Intelligent Pig Inspection of Uncoated Seamless Pipelines." Pipeline & Gas Journal, March 2000.

Smith, S.N., Duvivier, J.P., Lefevre, D.E., and Robb, G.A.: "Field experiences with intelligent pigs," paper NACE No. 37 presented at the NACE International Annual Conference and Exposition, 1996.

Staff Report: "Pigging - A good Year for Developments & Operational Success." Pipeline & Gas Journal Online, August 2001.

Tuboscope: "Geometric Pigs Operation Principles." Geometry Inspection, 2002, website: www.tuboscopepipeline.com

Vieth, P.H.: "Comprehensive, Long-Term Integrity Management Programs are being Developed and Implemented to reduce the Likehood of Pipeline Failures." Materials Performance Megazine, June 2002, pp. 17-22.

Van der Veer, P.A.J., Jager, S.F., Schmidt, R., and Bukman, F.: "Measuring Internal Corrosion in Small Diameter, Heavy Wall Pipelines." Pipeline & Gas Journal, March 2000.

Yen, S.K. and Tsai, Y.C.: "Critical Hydrogen Concentration for the Brittle Fracture of AISI 430 Stainless Steel." Journal of Electrochemistry Society, Vol.143, No. 9, September 1996, p. 2736.

Yen, S.K., Huang, I.B., Yen, Z. S.: "Effect of Electrolytic Zirconium Oxide Coating on Hydrogen Permeation of AISI 430 Stainless Steel." NACE International, Corrosion – October 2000, Corrosion Science Section, p998.